

*See also 192247
Space Telescope
San Martin*

May 7, 1990

PH9

Semi-Annual Report for NAG5-1076

*711 51-1
146597*

"Coronal Mass Ejections from a Young KO Dwarf Star"

P.80

by Dr. David Soderblom

Most of the work for this program has been completed. The overall coordinator was Dr. Andrew Collier Cameron of the University of Sussex, England. A paper has been written that brings together data from the International Ultraviolet Explorer (both NASA and ESA), the Anglo-Australian Telescope, and the European Southern Observatory to examine the variability in spectrum features that are indicative of coronal and chromospheric activity. From these variations it is possible to see individual clouds moving away from the star, conveying angular momentum. This paper, titled "Fast Spectroscopic Variations on Rapidly-Rotating, Cool Dwarfs. III. Masses of Circumstellar Absorbing Clouds on AB Doradus," has been accepted for publication in Monthly Notices of the Royal Astronomical Society.

This publication completes the major portion of this effort. With the resources remaining additional aspects of the observations are being examined.

(NASA-CR-192247) CORONAL MASS
EJECTIONS FROM A YOUNG KO DWARF
STAR Semiannual Report (Space
Telescope Science Inst.) 80 p

N93-71407

Unclass

29/89 0146597

Fast Spectroscopic Variations
on Rapidly-Rotating, Cool Dwarfs.
III. Masses of Circumstellar Absorbing Clouds
on AB Doradus*

A. Collier Cameron¹ D.K. Duncan^{2†} P. Ehrenfreund³ B.H. Foing^{4,5}
K.D. Kuntz² M.V. Penston^{6†} R.D. Robinson⁷ D.R. Soderblom^{2†}

December 20, 1989

¹*Astronomy Centre, University of Sussex, Falmer, Brighton BN1 9QH, ENGLAND.*

²*Space Telescope Science Institute[†], 3700 San Martin Drive, Baltimore, MD 21218, USA.*

³*Groupe de Physique du Solide ENS, 4 pl Jussieu, Tour 23, 75251 Paris Cedex, FRANCE.*

⁴*ESTEC, Keplerlaan 1, Postbus 299, 2200 AG Noordwijk, NETHERLANDS.*

⁵*Institut d'Astrophysique Spatiale, BP 10, 91871 Verrieres-le-Buisson, FRANCE.*

⁶*Royal Greenwich Observatory, Madingley Road, Cambridge, ENGLAND.*

⁷*Anglo-Australian Observatory, P.O. Box 296, Epping, NSW 2121, AUSTRALIA.*

Running title: Masses of coronal clouds in AB Dor.

*Based on observations made at ESO La Silla, the Anglo-Australian Observatory and the *International Ultraviolet Explorer* satellite.

[†]Guest Observer with the *International Ultraviolet Explorer* satellite.

[†]Operated by the Association of Universities for Research in Astronomy, Inc., under contract with the National

Aeronautics and Space Administration.

Summary: We present new time-resolved $H\alpha$, CaII H & K and MgII h & k spectra of the rapidly-rotating K0 dwarf star AB Doradus (= HD 36705). The transient absorption features seen in the $H\alpha$ line are also present in the Ca II and Mg II resonance lines. New techniques are developed for measuring the average strength of the line absorption along lines of sight intersecting the cloud. These techniques also give a measure of the projected cloud area. The strength of the resonance-line absorption provides useful new constraints on the column densities, projected surface areas, temperatures and internal turbulent velocity dispersions of the circumstellar clouds producing the absorption features. At any given time the star appears to be surrounded by at least 6 to 10 clouds with masses in the range $2 - 6 \times 10^{17}$ g. The clouds appear to have turbulent internal velocity dispersions of order $3\text{--}20 \text{ km s}^{-1}$, comparable with the random velocities of discrete filamentary structures in solar quiescent prominences. Night-to-night changes in the amount of Ca II resonance line absorption can be explained by changes in the amplitude of turbulent motions in the clouds. The corresponding changes in the total energy of the internal motions are of order 10^{29} erg per cloud. Changes of this magnitude could easily be activated by the frequent energetic ($\sim 10^{34}$ erg) X-ray flares seen on this star.

1 Introduction

AB Doradus is a young, spotted K0 dwarf with an unusually short axial rotation period of 0.514 day (Pakull 1981) . It is a flaring coronal X-ray source (Collier Cameron *et al.* 1988; Vilhu & Linsky 1987) . Optical and UV spectra show strong chromospheric and transition region line emission (Vilhu *et al.* 1987; Rucinski 1985), indicating high levels of magnetic activity in the star's outer atmosphere . Innis *et al.* (1986) suggested on the basis of its space motion that it is a likely member of the Pleiades Moving Group (also known as the Local Association: Eggen 1973, 1975, 1983a, b). This implies that AB Dor is similar in age to the Pleiades cluster. This is supported by its high lithium abundance (Rucinski 1982) and the existence of a population of similarly rapidly-rotating and magnetically-active K dwarfs in the Pleiades cluster (van Leeuwen *et al.* 1983, 1987; Stauffer *et al.* 1984, 1987).

In earlier papers in this series we discussed the properties of a system of prominence-like condensations of mainly neutral material, located between 3 and 10 stellar radii from the rotation axis of AB Dor and trapped in co-rotation with the star by the stellar magnetic field. The clouds were first discovered as transient absorption features in $H\alpha$ (Robinson & Collier Cameron 1986; Collier Cameron & Robinson 1989a: Paper I) . The absorption transients are produced when clouds pass between the observer and the stellar disc, scattering chromospheric $H\alpha$ photons out of the line of sight. New clouds appear to form at the rate of one or two per day, just outside the Keplerian co-rotation radius, and subsequently move outwards until they finally escape from radial magnetic confinement, at least $10 R_*$ from the rotation axis (Collier Cameron & Robinson 1989b: Paper II) .

The specific angular momentum of the escaping cloud material is clearly high, and suggests that the cloud ejection process could contribute significantly to AB Dor's rotational braking rate. Observations in $H\alpha$ alone do not, however, provide very tight constraints on the cloud masses, since the population of the lower state of the transition depends critically on both the temperature and density in the cloud interior. The CaII and MgII resonance lines are much better suited to determining the cloud column densities, but time-resolved spectroscopic studies of the CaII H & K line profiles were not possible until dye-coated CCD detectors with extended blue response became widely available.

In the present paper we report the results of a co-ordinated programme of observations of

AB Doradus made during 1988 December. We obtained high-dispersion, time-resolved $H\alpha$ and $\text{CaII } H \& K$ spectra at the European Southern Observatory (ESO) and the Anglo-Australian Observatory, and high-dispersion $\text{MgII } h \& k$ spectra with the *International Ultraviolet Explorer* (*IUE*) satellite. In Section 2 we summarise the observations and data reduction techniques used, and in Sections 3 and 4 we describe the data analysis methods and absorption line profile synthesis used to constrain the projected areas, column densities, temperatures and internal velocity dispersions of the clouds. The implications for the masses and internal structure of the clouds are discussed in Section 5.

2 Observations and data reduction

2.1 Observing strategy

The programme of *IUE*, *AAT* and *ESO* observations of AB Dor undertaken during 1988 December is summarised in the journal of observations (Table 1). Of the four nights allocated to the programme at the *AAT* (Dec 16 to 19) only one (Dec 18) was lost due to poor weather, although the data quality during first half of the night of Dec 17 was degraded by variable cloud cover. The two *ESA IUE* shifts on 1988 Dec 17 and 19 coincided with the hours of darkness at the *AAT*. Within the limits imposed by spacecraft temperature constraints and camera readout and preparation, the high-resolution LWP exposures of the $\text{MgII } h \& k$ region were made at stellar rotation phases where well-defined absorption transients or clear patches had been observed in $H\alpha$ at the *AAT* on Dec 16 and 17. $\text{CaII } H \& K$ observations were interleaved with the $H\alpha$ observations on Dec 19, the last night of the *AAT* run.

All three nights of the *ESO* programme (Dec 21 to 23) were clear. The first night was devoted to continuous monitoring of the $H\alpha$ profile, and the second to continuous monitoring of the $\text{CaII } H \& K$ region. On the last night of the *ESO* run, $H\alpha$ and $\text{CaII } H \& K$ spectra were interleaved. During the three *US IUE* shifts on Dec 24 and 25, alternating LWP and SWP exposures were made, covering the full stellar rotation cycle.

2.2 AAT instrument configuration

The AAT spectra were obtained with the new UCL échelle spectrograph (UCLES: Walker & Diego 1985), at the coudé focus of the 3.9m Anglo-Australian Telescope. The 31 lines mm^{-1} échelle grating was used with the 70cm camera and a liquid nitrogen-cooled, dye-coated GEC CCD as detector, giving a dispersion of 2.7 km s^{-1} per $22 \mu\text{m}$ pixel in the dispersion direction. A slit width of 1.3 arc sec gave an instrumental profile with full width at half maximum intensity of 2.8 pixel, or 7.5 km s^{-1} . During times of poor seeing, a focal reducer (Diego & Walker 1985) was used to increase throughput by opening the slit width to 1.7 arcsec, while maintaining the same resolution at the detector. The CCD chip was binned by a factor of four in the slit direction, to reduce both readout noise and chip readout time. The exposure times used were 150s for all $\text{H}\alpha$ exposures, and 300s for CaII H \& K .

2.3 ESO instrument configuration

The ESO spectra were obtained with the Cassegrain Echelle Spectrograph (CASPEC; Pasquini & D'Odorico 1989) on the 3.6m telescope at La Silla. A 31.6 lines mm^{-1} grating was used on the first night (1988 Dec 21 UT) in the red range centered at 6250\AA . A 52 lines mm^{-1} grating was used on the second night in the blue range centered at 4200\AA . On the third night the 31.6 lines mm^{-1} was used again, alternating between the blue and red ranges. The CASPEC échelle spectral range covers around 1000\AA at once, allowing features other than the prime lines ($\text{H}\alpha$ and CaII H \& K) to be observed. The light is focussed by a 291mm camera onto a Thomson CCD detector with 1024×660 15 micron pixels. A slit width equivalent to 1.5 arcsec allowed an instrumental spectral resolution of 30000 or 10 km/s. The seeing ranged between 1 to 1.5 arcsec and the weather was photometric during the ESO observing period. The whole CCD chip was read unbinned, using an exposure time of 300s for all AB Dor frames, with a time lag of 50-60s between exposures. The pixel to pixel response and wavelength calibration were determined by using a quartz flat-field and a Th-Ar lamp.

2.4 IUE instrument configuration

IUE (Boggess *et al.* 1978) high resolution spectra were taken through the large aperture (5×10 arcsec) with the Long Wavelength Prime camera covering the MgII h \& k emission lines.

The Vilspa ground station near Madrid, Spain was used for the observations on 1988 December 17 and 19; the images were received at Goddard Space Flight Center in Greenbelt, Maryland in the United States on 1988 December 25 and 26. Exposure times were generally 40 minutes in duration, although exceptionally they were varied to 35 or 60 minutes (see Table 6). These provided reasonably exposed emission lines while avoiding too much smearing of features varying in wavelength during the exposure. The continuum is weak but visible. The spectral resolution of this observing configuration is 0.17\AA (18 km/s).

2.5 Data reduction: $H\alpha$ and Ca II spectra

The échelle spectra from both *UCLES* and *CASPEC* were reduced at the RGO node of the UK *Starlink* network. The data were extracted and calibrated using the AAO/CalTech échelle reduction routines incorporated in the FIGARO package. After flat-fielding and extraction, each individual échelle order was written into a single row of a two-dimensional dynamic spectrum. Thorium-argon arc exposures provided the wavelength calibration for both the *AAT* and *ESO* spectra. Each dynamic spectrum was rebinned to equal increments in log wavelength, with a velocity increment per pixel of 2.7 km s^{-1} . Finally, each row in the dynamic spectrum was corrected for low-frequency variations in continuum shape using a polynomial fit to a set of continuum windows. The $H\alpha$ spectra were normalised to a continuum level set at unity. Because of the difficulty of locating the continuum in the blue part of the spectrum, the CaII *H* & *K* spectra were normalised to a mean value of 1.0 over the wavelength range 3925.0 to 3975.0 \AA . Sample $H\alpha$ and CaII *H* & *K* spectra are shown in Fig. 1.

2.6 Data reduction: Mg II spectra

The data sets from VILSPA and Goddard were extracted at their institute of origin using standard procedures. Both data sets were calibrated using the RDAF routine calibration.

Both MgII lines are overlaid by a narrow interstellar line, for whose absorption one must correct before measuring the flux. It was assumed that the interstellar absorption was unresolved, so that each MgII line could be fit by the function

$$F(\lambda) \simeq F_c(\lambda) + A_e \exp[-z_e^2(\lambda)] - F(\lambda_a) \frac{W_a}{\sigma_a \sqrt{\pi}} \exp[-z_a^2(\lambda)]. \quad (1)$$

Here $F_c(\lambda)$ is the continuum flux, which was fit as a second order polynomial. A_e is the amplitude of the emission gaussian. $F(\lambda_a)$ is the value of the underlying stellar monochromatic flux at the wavelength λ_a of the interstellar absorption line, and (ignoring the contribution of the continuum) is given approximately by $F(\lambda_a) = A_e \exp[-z_e^2(\lambda_a)]$. W_a is the equivalent width in angstroms of the interstellar line absorption and σ_a is the width of the instrumental profile, treated here as a gaussian. We also use the notation

$$z_e(\lambda) = \frac{\lambda - \lambda_e}{\sigma_e}, \quad (2)$$

$$z_a(\lambda) = \frac{\lambda - \lambda_a}{\sigma_a} \quad (3)$$

where λ_e is the wavelength of the emission gaussian. As the equivalent width of the interstellar absorption and the instrumental resolution must be the same for all exposures, the lines from all exposures should be fit simultaneously. In practice, all of the k lines were fit simultaneously, and all the h lines were fit simultaneously, but the whole set of lines were never fit as one batch. The equivalent widths of the interstellar lines and the instrumental resolutions from the two different fits were quite similar.

The fitting was done with a modified amoeba algorithm (Press *et al.* 1986; Kuntz 1990, in preparation). Uncertainties determined for the calculated quantities are the most extreme values of those quantities for which the chi square of the fit (at the extreme value of the calculated quantity) minus the best possible chi square for the fit is unity. The algorithm used to determine uncertainties is described in full in Kuntz (1990, in preparation).

The fluxes from the MgII lines were measured in two ways: (a) the area under the fitted gaussian emission profile was calculated, and (b) the absorbed flux $F(\lambda_a)W_a$ calculated from the fit was added to the observed flux minus the fitted continuum, integrated over a 3.4\AA (i.e. $\pm 180\text{ km s}^{-1}$) window centered on the line. The measured flux (minus fitted continuum), the fitted absorbed flux, the corrected measured flux and the fitted emission flux are listed for each spectrum in Table 2. The two methods do not agree as well as one would like. The ratio of the quantity as measured by the first method to that measured by the second will always be greater than unity, and will increase with increasing noise. This is due to the fitted flux being a function of the width of the emission gaussian, which will always be larger than it should be due to the noise in the wings. The quantity derived by the second method (labelled "Corrected

flux" in Table 2) is therefore to be preferred.

3 Measuring the cloud absorption profiles

3.1 H α profile analysis

Normally, chromospheric emission fills the H α profile in AB Dor, almost exactly to the level of the adjacent continuum. To a good approximation we can thus treat the background illuminating source for the clouds as a flat continuum in H α . When a cloud passes between the stellar disc and the observer, it scatters chromospheric H α photons out of the line of sight. There is little coupling between the thermal properties of the cloud and the radiation field. In Paper I we inferred from statistical equilibrium studies that the cloud source function consists solely of the stellar radiation field, diluted according to the distance of the cloud from the star. The population of the $n = 3$ level of H I is sufficiently low that both recombination and stimulated emission in H α are negligible. Since most of the clouds are located approximately $3 R_*$ from the star, the cloud source function should be at most 3 percent of the intensity of the chromospheric background in H α . For this reason we expect to see a "pedestal" of weak emission coming from off-disc clouds. In Paper I we found that the amplitude of the pedestal emission in a time-averaged spectrum was greatest at $\pm 3 v_e \sin i$ from line centre, and was at most one or two percent of the stellar background spectrum in H α . This agrees with our expectations, because the majority of the clouds are located just outside the co-rotation radius and the clouds near the inner edge of the distribution will have the greatest surface brightnesses. The upper limit of 1 or 2 percent on the pedestal emission tells us that the total projected area of all the clouds in the system is probably between 1 and 5 times the projected surface area of the star. Since the average cloud cross-sectional area is roughly 20 percent of the disc area, this suggests that at any time there are between 5 and 20 clouds of this size surrounding the star, and that they form preferentially close to the stellar equatorial plane.

The radial temperature gradient in the layers of the stellar chromosphere where H α and the Ca II and Mg II resonance line emission features are formed is small enough that we are justified in neglecting centre-to-limb variations in the emission line profiles for a lowest-order analysis.

In this very simple situation the observed equivalent width W of the cloud absorption profile is just the average of the absorption equivalent width w calculated along all lines of sight intersecting the stellar disc. Since the clouds appear to be well-defined, sharp-edged entities, we can also express the observed equivalent width in terms of the effective fraction of the stellar disc covered by clouds, and an area-weighted mean absorption equivalent width \bar{w} :

$$W = \frac{1}{4\pi R_*^2} \int \int_{\text{disc}} w(x, y) dy dx \quad (4)$$

$$\equiv \bar{w} \frac{A_{\text{cloud}}}{A_*}. \quad (5)$$

If we can determine the value of \bar{w} from the line profiles, we can use the observed EW variations in $\text{H}\alpha$ to determine the fraction of the stellar disc covered by clouds at any time.

In interpreting the shapes of the line profiles, we make the simplifying assumptions that

1. the cloud source function is zero,
2. the background continuum intensity I_0 is independent of wavelength,
3. the absorption equivalent width w is the same along all lines of sight intersecting a cloud and the stellar disc, and
4. there is no centre-to-limb variation in the chromospheric $\text{H}\alpha$ surface brightness.

When no cloud is obscuring the disc, the observed continuum flux is

$$F_c = I_0 \int_{-1}^1 c(x) dx \equiv \pi I_0 \quad (6)$$

Here we define the independent variable x as the radial velocity along a given line of sight in units of $v_e \sin i$, or equivalently as the projected x -coordinate of the line of sight on the stellar disc in units of the stellar radius. A chord across the stellar disc, running through x parallel to the projected rotation axis, has a length $c(x) \equiv 2(1 - x^2)^{1/2}$. We also define a function $h(x)$ to describe the shape of a section of the star obscured by cloud. The units of $h(x)$ are the same as those of $c(x)$, so that

$$\int_{-1}^1 h(x) dx = \pi \frac{A_{\text{cloud}}}{A_*}. \quad (7)$$

The rotation profile of the star is thus given by $c(x)$, and the rotation profile of the part of the stellar disc occupied by clouds is given by $h(x)$.

The observed line profile is the convolution of the background spectrum $I(x) \equiv I_0$ with the rotation profile of the unobscured part of the disc, plus the convolution of the absorption profile $I_c(x)$ along a single line of sight through the cloud with the cloud rotation profile:

$$F(x) = I_0 \int_{-1}^1 [c(x') - h(x')] dx' + \int_{-1}^1 I_c(x - x') h(x') dx'. \quad (8)$$

We obtain the fractional depression of the observed monochromatic flux below the level of the continuum from Eqs. (6) and (8):

$$\frac{F_c - F(x)}{F_c} = \frac{1}{\pi I_0} \int_{-1}^1 [I_0 - I_c(x - x')] h(x') dx' \quad (9)$$

In the limit where the cloud has a small extent in x , giving a rotation profile $h(x)$ narrower than the width of the intrinsic absorption profile $I_c(x)$, we can treat $h(x)$ as a δ -function with area $\pi A_{\text{cloud}}/A_*$, located at the x -coordinate x_c of the cloud centre. Eq. (9) then simplifies to

$$\frac{F_c - F(x)}{F_c} = \frac{A_{\text{cloud}}}{A_*} \left(\frac{I_0 - I_c(x - x_c)}{I_0} \right) \quad (10)$$

If the cloud absorption profile is saturated, then $I_c(0) = 0$. *The fractional depression of the deepest part of the observed line profile is then equal to the fraction of the stellar disc obscured by the cloud.* Note that if we integrate over x , we recover the result of Eq. (5), since

$$W \equiv \int_{-\infty}^{\infty} \frac{F_c - F(x')}{F_c} dx' \quad (11)$$

and

$$\bar{w} \equiv \int_{-\infty}^{\infty} \frac{I_0 - I_c(x')}{I_0} dx'. \quad (12)$$

In practice, this condition is satisfied for a time as the leading edge of a cloud starts to move on to the disc, and again as its trailing edge moves off the disc. During these opening and closing stages of a transient, the equivalent width of the observed profile is $W = \bar{w} A_{\text{cloud}}/A_*$, and the fractional depth of the centre of the absorption profile is $(1 - F(x_c)/F_c) = A_{\text{cloud}}/A_*$. That is, a plot of the equivalent width against the depth of the observed absorption profile should give a straight line with slope \bar{w} .

Fig. 2 shows the width-depth plots for the opening and/or closing phases of twelve of the best-defined H α absorption transients observed during the campaign. The slopes of the linear parts of these relations are listed in Table 3. The average value is 44.98 pixel (2.66Å) with a

2σ scatter of 12.56 pixel (0.74\AA). The small observed spread in the values of \bar{w} allows us to estimate reliably the rate at which the fraction of the disc obscured by clouds is varying, even if we cannot make a direct density estimate for each individual cloud.

3.2 Ca II profile analysis

At the temperatures and densities inferred for the clouds in Paper I, most of the calcium is expected to be singly-ionised and in the ground state. In this case we can estimate the total column density of the clouds from the column density of Ca II ions, assuming normal solar abundances.

The cores of the CaII *H* & *K* resonance lines in AB Dor show strong chromospheric emission reversals, giving a plentiful background source of photons in these lines. The effect of the circumstellar clouds on the observed profiles is similar to that in $H\alpha$: CaII *H* & *K* photons are scattered out of the line of sight when clouds pass between the stellar disc and the observer, giving rise to travelling absorption features in the dynamic spectra. No strong off-disc emission features are present in the dynamic spectra, indicating that once again the cloud source function in these lines is small, consisting mainly of scattered stellar CaII *H* & *K* photons.

In interpreting the shapes of the CaII *H* & *K* profiles, we make simplifying assumptions similar to those used in the discussion of the $H\alpha$ profiles:

1. the cloud source function is zero,
2. the total cloud column density is the same along all lines of sight intersecting a cloud and the stellar disc, and
3. there is no centre-to-limb variation in the chromospheric CaII *H* & *K* spectrum.

If the underlying spectrum in the co-rotating frame is $I_0(x)$, then the emergent spectrum along a line of sight through the cloud is

$$I_c(x) = I_0(x)e^{-\tau(x)}. \quad (13)$$

The observed monochromatic flux is obtained by convolving the underlying spectrum with the rotation profile of the unobscured part of the disc, and the absorbed spectrum with the

rotation profile of the obscured part:

$$F(x) = \int_{-1}^1 I_0(x - x')[c(x') - h(x')] dx' + \int_{-1}^1 I_c(x - x')h(x') dx'. \quad (14)$$

The total flux scattered out of the line of sight by the clouds is most conveniently expressed as a line index I_K or I_H , measured relative to the total (unobscured) flux over a wavelength band extending from $1.5v_e \sin i$ blueward to $1.5v_e \sin i$ redward of line centre:

$$I_{K,H} = \frac{\int_{-3/2}^{3/2} [F_0(x') - F(x')] dx'}{\int_{-3/2}^{3/2} F_0(x') dx'}. \quad (15)$$

If we define a similar line index for a single line of sight through the cloud

$$\bar{i}_{K,H} = \frac{\int_{-3/2}^{3/2} [I_0(x') - I_c(x')] dx'}{\int_{-3/2}^{3/2} I_0(x') dx'}, \quad (16)$$

we can see that to a good approximation, $I_{K,H} = \bar{i}_{K,H} A_{\text{cloud}}/A_*$, as is the case with the $H\alpha$ equivalent widths. A plot of the observed line index I_K or I_H against $H\alpha$ equivalent width W should give a straight line with slope \bar{i}/\bar{w} . This gives us a measure of \bar{i} , since we can determine \bar{w} directly from the $H\alpha$ profile width/depth variations:

$$\bar{i}_{K,H} \simeq \bar{w} \frac{dI_{K,H}}{dW} \quad (17)$$

In practice, this technique works best when we use short sequences of interleaved $H\alpha$ and CaII $H \& K$ observations made at times when the total amount of cloud coverage on the stellar disc is changing rapidly. Over longer periods, rotational changes in the background chromospheric emission flux can give rise to spurious drifts in the $H\alpha$ equivalent width and the CaII $H \& K$ line indices.

For shorter sequences, the dominant source of error in measuring the line core fluxes in the calibrated, normalised spectra lies in the polynomial fit used to straighten the continuum. We compensate for this by measuring the line core flux relative to two reference bands, each $0.75v_e \sin i$ wide, immediately adjacent to the line core band. Photon shot noise and readout noise then provide a good estimate of the uncertainty in each line index measurement. For the Dec 19 and 23 data, we interpolate linearly in time to obtain the value of W at the time of each Ca II observation. For the continuous series of Ca II spectra taken on 1988 Dec 22, we can estimate the the values of W at a given rotation phase by interpolation, using $H\alpha$ spectra

taken at the same rotation phase on 1988 Dec 21 and 1988 Dec 23. Fig. 3 shows the difference between values of W measured on these two nights, at the phase corresponding to a given UT on 1988 Dec 22. During the intervals used in Fig. 4 and Table 5, it can be seen that the phase-dependent changes in W did not evolve significantly between Dec 21 and Dec 23. Note, however, that the time-dependent zero-point drifts in the $I_{K,H} - W$ relations for Dec 22 are considerably greater than those on Dec 19 and 23. The $H\alpha$ equivalent widths obtained using this technique may not be as reliable as those obtained by alternating observations at the two different wavelengths.

In Fig. 4 we show the CaII H & K line index - $H\alpha$ equivalent width relation for a total of 8 sequences on Dec 19, 22 and 23. The slopes of the straight-line fits to these plots are listed in Table 5.

3.3 Mg II profile analysis

The analysis of the MgII h & k profile variations on 1988 Dec 17 and 19 is very similar to that described above for the CaII H & K data. Like the calcium, most of the magnesium in the clouds will be singly-ionised and in the ground state. The chromospheric MgII h & k emission provides a background source of photons which are scattered out of the line of sight by the clouds. Again the line source function in the clouds is expected to consist solely of scattering terms. The low level of the surrounding continuum allows us to place further constraints on the total projected surface area of the cloud system. The base widths of the MgII h & k emission lines are close to 3\AA . Clouds located just outside the co-rotation radius should produce pedestal emission between 2.0 and 2.5\AA to either side of line centre when they are near maximum elongation. The pedestal emission comprises no more than 30 percent of the signal at this distance from line centre, and may be less because of the extended wings of the chromospheric emission features. If, as we argue below, the cloud optical thickness is such that the width of the absorption profile is similar to the emission base width, then the total scattered flux from the whole cloud system should be some 3 percent of the total chromospheric emission flux multiplied by the total projected area of the cloud system in units of the stellar disc area. The upper limit on the total scattered flux is of order $4 \times 10^{-13} \text{ erg cm}^2 \text{ s}^{-1}$, while the total chromospheric emission flux is of order $4 \times 10^{-12} \text{ erg cm}^2 \text{ s}^{-1}$. This implies a total projected

area for the cloud system of three times the stellar disc area, in good agreement with the value inferred from the $H\alpha$ pedestal emission.

The procedures for forming line indices and calculating their dependence on cloud column density are nearly identical to those described above for Ca II, and so will not be repeated here. The band over which the line indices $I_{k,h}$ and $i_{k,h}$ are calculated extends from $2.0 v_e \sin i$ blueward to $2.0 v_e \sin i$ redward of line centre. No photospheric reference sidebands are used in this case because of the very low level of the surrounding continuum. The sensitivity of the LWP camera is sufficiently stable that the use of such sidebands is unnecessary. The line profiles and integrated fluxes have, however, been corrected for the effects of interstellar absorption as described in Section 2.6 above.

The main problem in interpreting the simultaneous $H\alpha$ and MgII h & k data is the long exposure times of the *IUE* spectra. Substantial changes in cloud covering fraction often occurred during the MgII exposures, as seen from the changes in the $H\alpha$ EW during each exposure. A second problem is that it was not possible to measure the intrinsic $H\alpha$ EW (\bar{w}) for every cloud contributing to the MgII line index - $H\alpha$ absorption EW relations.

The best we can do is to average all measurements of the $H\alpha$ absorption equivalent width made during each MgII exposure, to obtain the *time-averaged* value of W during the *IUE* exposure. Secondly we must assume an average value of \bar{w} in order to estimate the average cloud covering fraction during the exposure from the average value of W . We must bear in mind that the results may be affected by spurious zero-point drifts, caused by rotationally-dependent changes in either the underlying $H\alpha$ or Mg II emission flux. However, the $H\alpha$ width-depth plots for five different transients observed on 1988 Dec 17 and 19 all lie on the same relation (Fig. 2). This suggests that any such drifts are small, in $H\alpha$ at least.

The observed MgII h & k line indices $I_{k,h}$, and the corresponding time-averaged W values for the $H\alpha$ absorption are listed in Table 6. The $I_{k,h}$ - $H\alpha$ absorption EW relations are shown in Fig. 5. The discrepant point in both these plots corresponds to the first *IUE* exposure made on 1988 December 19, LWP14672. Closer examination of this spectrum revealed that both the MgII emission and the surrounding continuum fluxes are consistently lower than the other exposures, by nearly a factor of 2. The reason for this flux deficiency is not clear: it is possible that the star was not properly centred in the entrance aperture.

If the data from LWP14672 are excluded, the $I_{k,h}$ - $H\alpha$ absorption EW relations are well-represented by linear relations, with slopes of $(dI_k/dW) = 0.58 \pm 0.06$ and $(dI_h/dW) = 0.49 \pm 0.06$ respectively. If we assume that the cloud scatters *all* the chromospheric MgII photons out of any line of sight intersecting the cloud, this implies an upper limit on \bar{w} of $1.90 \pm 0.15\text{\AA}$. This is within the scatter of the distribution of \bar{w} values measured from the $H\alpha$ width-depth relations. This indicates that the width of the absorption profile of a typical cloud in the MgII resonance lines is comparable with the base width of the chromospheric emission features, and so places a lower limit on the cloud optical thickness.

4 Line index - column density relations

4.1 $H\alpha$ profile synthesis

For the larger clouds studied here, the range in intrinsic $H\alpha$ absorption equivalent widths \bar{w} , and hence in column densities of hydrogen atoms in the first excited state ($n = 2$), is small (Table 3). These larger clouds have projected surface areas between 13 and 18 percent of the stellar disc area, so it is not too surprising that their other physical properties should be fairly similar.

The equivalent width of the $H\alpha$ absorption profile depends principally on

1. the total column density of cloud material;
2. the degree of excitation and ionisation of hydrogen in the cloud interior; and
3. the amplitude of turbulent random motions within the cloud.

turbulent motions within the cloud have the effect of broadening the Doppler core of the absorption profile, although it is less important for hydrogen than for heavier atoms with small thermal doppler widths. By analogy with quiescent solar prominences, we suspect that turbulent motions may be important in the AB Dor clouds. The clouds are likely to have a highly-fragmented structure: the effective pressure scale height in the cool cloud material is determined by the combined gravitational acceleration and the cloud temperature, and is of order 200 to 300 km, which is very much smaller than the overall cloud extent. Nakagawa & Malville (1969) found that in the solar case, the prominence-corona interface was unstable

to fragmentation for perturbations with wavelengths longer than the pressure scale height. Given that conditions inside the AB Dor clouds are likely to be similar, it seems plausible that filamentary structures similar to those seen in quiescent solar prominences may be present, and that individual elements of this fine structure may have random velocities at least as great as the 5 to 10 km s^{-1} observed by Engvold (1972) in the solar case.

In Fig. 6 we show contours of constant $H\alpha$ absorption equivalent width \bar{w} , computed as a function of the column density of H atoms in the $n = 2$ level and a gaussian turbulent velocity component. The contours span the observed range of \bar{w} values, and show little change as the turbulent velocity dispersion is increased from 0 to 20 km s^{-1} . The range in column density of singly-excited H atoms permitted by the observations spans less than an order of magnitude: for a turbulent velocity of 10 km s^{-1} , $\log n_{n=2} = 14.4 \pm 0.2 \text{ cm}^{-2}$.

The degree of excitation of hydrogen within the cloud is influenced mainly by the cloud kinetic temperature, and to a lesser extent by the volume density of the cloud material. The statistical equilibrium in the cloud interior was discussed in some detail in Paper I, to which the reader is referred for further details. Here we use the same model with a 5-level H atom plus continuum, and the Lyman lines and continuum in radiative detailed balance. In Fig. 7 we show contours of constant w as a function of cloud temperature and total hydrogen column density $n_H + n_p$, computed using a turbulent gaussian velocity dispersion of 10 km s^{-1} .

Fig. 7 was computed for a slab of uniform density with a thickness of one stellar radius, comparable to the projected linear dimensions of the clouds. If the clouds are significantly fragmented, however, the *local* density in the neutral material will be very much greater than we have assumed. We can explore this possibility by computing a second set of models in which the slab thickness is decreased by a factor of 1000 and the local density increased by the same factor to give the same total column density. The results are shown in Fig. 8. At temperatures below 8000 K there is little difference between the uniform and fragmented models. At higher temperatures, however, when a substantial fraction of the hydrogen is ionized, the higher local densities in the fragmented model serve to increase the recombination rate, increasing the amount of neutral hydrogen relative to the uniform density model. The observed optical thickness in $H\alpha$ is thus achieved at a column density up to an order of magnitude lower in the fragmented model than in the uniform model.

Figs. 7 and 8 show clearly that the observed H α equivalent widths effectively rule out total cloud column densities less than $(8 \pm 4) \times 10^{18} \text{ cm}^{-2}$. This lower limit on the column density occurs at a temperature close to $1.1 \times 10^4 \text{ K}$, where the number density ratio of H atoms in the $n = 2$ level passes through a maximum relative to the total number density ($n_H + n_P$). At higher temperatures, the increasing degree of excitation is offset by the decrease in the amount of neutral hydrogen as the hydrogen becomes ionised; while at lower temperatures the hydrogen is mainly neutral but the degree of excitation is lower.

4.2 Ca II profile synthesis

We now need to calibrate the variation of $\bar{i}_{K,H}$ with column density. The amount of flux scattered out of a single line of sight depends on -

1. the width of the chromospheric emission core in the background stellar spectrum *as seen in the co-rotating frame of the cloud*;
2. the velocity dispersion of the Ca II ions in the cloud; and
3. the column density of Ca II ions in the cloud.

Although we cannot determine the intrinsic width of the emission core directly (owing to the extreme rotational broadening of the spectrum) we can make a reasonable estimate based on observations of more slowly-rotating, active stars of similar spectral type. Empirical studies of CaII H & K emission profile widths in a large number of dwarfs and giants with a range of spectral types and chromospheric activity levels show that the full widths at half maximum (FWHM) of the chromospheric Ca II emission cores are insensitive to the level of chromospheric heating, although they are very sensitive to surface gravity (Wilson & Bappu 1957). In a theoretical study of chromospheric scaling laws, Ayres (1979) found that the base width $\Delta\lambda_*$ of the chromospheric Ca II emission cores and the thermalisation width $\Delta\lambda_A$ have equal and *opposite* dependences on metallicity, stellar effective temperature and chromospheric heating, but the *same* dependence on surface gravity. The thermalisation width corresponds to the separation of the red and blue peaks of the emission profile. The functional dependence of the FWHM of the emission profile on the various stellar parameters is intermediate between those of the base width and the thermalisation width: that is, the effects of metallicity, effective

temperature and chromospheric heating cancel out, leaving only the gravity dependence of the Wilson-Bappu effect.

The compilation of high-resolution CaII *H* & *K* profiles of late-type stars by Linsky *et al.* (1979) gives FWHM values for several stars of similar surface gravity and spectral type to AB Dor. The scatter in these widths is small, and we adopt a mean value of $0.43 \pm 0.04 \text{ \AA}$ as the FWHM of the CaII *H* & *K* emission cores in AB Dor. For modelling purposes, we represent the background spectrum by a gaussian emission core of appropriate width and amplitude, superimposed on a parabolic fit to the broad photospheric absorption profile.

The atomic parameters used in calculating the line absorption profiles are listed in Table 4. The thermal Doppler width of the absorption profile is $1.2 \pm 0.2 \text{ km s}^{-1}$ over the temperature range 5000 to 10000 K, in which the cloud temperature is expected to lie. As described above, however, we also consider the possibility that turbulent broadening of up to 20 km s^{-1} may be also be present due to random motions of fragmented sub-structures within the clouds.

In Fig. 9 we plot contours of constant line index i_K and i_H as a function of cloud column density and turbulent velocity, for an assumed cloud temperature of 8500 K and a background emission core width of 0.43 \AA . The effects of varying the background emission core width are illustrated in Fig. 10: the effects on the line index are negligible.

We can use the model line index maps shown in Fig. 9 to determine a confidence region in $(n_H + n_p, v_{\text{turb}})$ space, within which we can achieve a satisfactory fit to the observations. For each sequence of n Ca II observations of a single absorption transient, we usually had observations of the K-line in two different echelle orders, and of the H-line in a single order. Each $(n_H + n_p, v_{\text{turb}})$ pair defines the slope of a theoretical line index - $H\alpha$ equivalent width relation, in each of the H and K lines. At each value of $n_H + n_p$ and v_{turb} we fix the slope at the theoretical value, and determine the zero-point offset for each line in each order, by minimising the statistic

$$S = \sum_{i=1}^n n \frac{D_i - F_i}{\sigma_i} \quad (18)$$

where D_i and F_i are the observed and predicted data values and σ_i is the observational scatter. We then sum the resulting values of S for all lines and orders, and so build up a map of S as a function of $n_H + n_p$ and v_{turb} , incorporating all the data on each individual cloud observed.

We identify the contours of constant S corresponding to the 95.4 and 99.0 percent confidence limits on $(n_H + n_p, v_{\text{turb}})$ using the parameter estimation method of Lampton, Margon & Bowyer (1976). The value S_L on the contour that has a probability α of enclosing the true values of the parameters is given by

$$S_L = S_{\min} + \chi_p^2(\alpha). \quad (19)$$

Here S_{\min} is the minimum value of S in the map, and $\chi_p^2(\alpha)$ is the tabulated value of the χ^2 distribution for p degrees of freedom and significance α . In this case there are two free parameters, so that $p = 2$. The 95.4 and 99.0 percent confidence regions in $(n_H + n_p, v_{\text{turb}})$ space are shown for the eight clouds observed, in Fig. 11.

We verified that $p = 2$ was the correct choice by Monte Carlo simulation, as follows. We assume that the “true” cloud parameters are those giving the minimum value of S , i.e. $S_{\text{true}} = S_{\min}$. Using these parameters we generate a large number of artificial data sets with normally-distributed errors. For each artificial data set we generate a new map of $S'(n_H + n_p, v_{\text{turb}})$, and locate the minimum value S'_{\min} . The value of S corresponding to this $(n_H + n_p, v_{\text{turb}})$ pair in the *original* map derived from the actual data is noted. After n such simulations, we sort the n resulting S values into ascending order, and note the limiting values S_L below which 95.4 and 99.0 percent of the simulated minima lie. We found good agreement between the contour levels estimated in this way and those estimated by the method of Lampton *et al.*

4.3 Mg II profile synthesis

The modelling of the Mg II line profiles as viewed in the co-rotating frame (and hence the Mg II line indices $i_{h,k}$) as functions of the cloud column density was very similar to that used for the Ca II profiles. Again the chromospheric emission profile was approximated by a gaussian. The width of the synthetic profile was based on *IUE* observations of chromospheric Mg II emission profile widths for several nearby late-G and early-K dwarfs (Basri & Linsky 1979). As with the Ca II profiles of Linsky *et al.* (1979), the scatter in the profile widths for the stars in the Basri & Linsky sample is small, and we adopt a mean FWHM of $0.60 \pm 0.06 \text{ \AA}$ for our synthetic gaussian profile.

Fig. 12 shows contours of constant line index i_k and i_h as functions of cloud column density and turbulent velocity, for an assumed cloud temperature of 8500 K and a background emission

core width of 0.60\AA . In Fig. 13, the effects on the line index - column density relations of varying the background emission core width by $\pm 0.06\text{\AA}$ are represented as in Fig. 10: once again, the line index is seen to be insensitive to errors in the estimated width of the chromospheric emission core.

The contours of constant χ^2 bounding the 95.4 and 99.0 percent confidence regions in $(n_H + n_p, v_{\text{turb}})$ space, within which we can obtain a satisfactory fit to the combined 1988 Dec 17 and 19 MgII *h* & *k* line index - H α EW relations, excluding LWP14672, are shown in Fig. 14.

5 Cloud masses and internal velocity fields

Using the techniques developed in Section 3 we have succeeded in measuring both the equivalent width of the H α absorption and the amount of the Mg II and Ca II resonance line scattering, along typical lines of sight running through some of the larger circumstellar clouds. When compared with the line profile synthesis results of Section 4, the observed line indices provide a set of independent constraints on the column densities, temperatures and turbulent internal velocity dispersions of the clouds. The H α equivalent widths are more sensitive to the density and temperature of the cloud material than to the random internal motions. The CaII *H* & *K* and MgII *h* & *k* line indices are more sensitive to column density and turbulent motions than to cloud temperature.

The H α equivalent widths of the various clouds studied show remarkably little scatter. If the physical conditions affecting the degree of excitation and ionization of hydrogen are similar for all the clouds, this would imply that the total hydrogen column density is similar for the various clouds studied. The situation for the Ca II resonance lines is not quite so simple. For a fixed turbulent velocity dispersion, the scatter in the inferred column density varies by as much as two orders of magnitude from cloud to cloud. The three clouds for which we obtained good Ca II line index - H α equivalent width relations on 1988 Dec 22 and 23 showed a marked decrease in Ca II absorption over the course of two stellar rotations. Over the same period, however, the H α equivalent width and fractional area coverage underwent only minor evolution.

There are two possible explanations for this behaviour. First, the amount of material in

each of these three physically distinct clouds may have decreased by a factor of between 10 and 100 between 1988 Dec 22 and 23. Let us suppose that the clouds are in thermal equilibrium, such that a fixed rate of conductive and mechanical energy input is balanced by radiative losses in strong, effectively thin lines such as the hydrogen Balmer series and the Mg II and Ca II resonance lines. In this case, a drop in the cloud density will lead to an increase in temperature until the electron density (and hence the radiative loss rate) has attained more or less its original value. At the temperatures and densities considered here, the $n = 2$ level population of hydrogen varies almost in direct proportion to the electron density, provided that the degree of ionization of the cloud material is small. This “thermostat” acts to keep the H α absorption equivalent width at a nearly constant value. At temperatures above 10^4 K, however, hydrogen is almost completely ionised so that this mechanism breaks down. As Figs. 7 and 8 show, the lowest total column density that can possibly give rise to the observed H α equivalent widths is of order 10^{19} cm^{-2} , so that the total column densities on 1988 Dec 22 must have been one to two orders of magnitude greater, i.e. *at least* 10^{20} to 10^{22} cm^{-2} .

The second possibility is that the column density and temperature did not change. Instead, the decrease in the strength of the Ca II absorption could have been caused by a change in the average amplitude of the turbulent motions inside the clouds, from $10\text{-}20 \text{ km s}^{-1}$ on Dec 22 to 4 km s^{-1} or less on Dec 23. The solar analogy provides some evidence in favour of this idea. Solar quiescent prominences often undergo temporary increases in the amplitude of their internal motions. These activations usually occur in response to a solar flare, when large-scale magnetic wave disturbances spread out through the corona, propagating large distances over the surface of the Sun at speeds of order 1000 km s^{-1} . The internal motions in the prominence increase from the usual $5\text{-}10 \text{ km s}^{-1}$ to $30\text{-}50 \text{ km s}^{-1}$, and after an hour or so may either die down or lead to an outward eruption of the entire prominence (Bruzek 1969). Given that AB Dor undergoes strong soft X-ray flares at a rate of one or two per day (Pakull 1981; Vilhu & Linsky 1987; Collier Cameron *et al.* 1988), this explanation seems plausible and has the added attraction that it can explain why three physically distinct circumstellar clouds should all show enhanced Ca II absorption only during one four-hour series of observations, on Dec 22. Further simultaneous optical and X-ray observations are planned for the near future, and should allow us to determine whether X-ray flares and Ca II absorption enhancements are correlated.

In Table 7 we list the various constraints on the cloud temperature and internal motions, as functions of column density. The range of cloud temperatures consistent with the observed $H\alpha$ equivalent width is listed, for a cloud model with uniform density (filling factor $f = 1$, as in Fig. 7) and for a fragmented model with filling factor $f = 10^{-3}$ (Fig. 8). The 99 percent confidence limit on the value of v_{turb} consistent with the observed amount of Mg II absorption on 1988 Dec 17 (Fig. 14) is shown, as are the limits on v_{turb} for each of the clouds observed in CaII $H \& K$ (Fig. 11). Under the assumption that the differences in Ca II absorption from cloud to cloud are due to differences in internal velocity dispersion rather than column density, it seems that the only value of the column density that is capable of satisfying all the observational constraints simultaneously, is $n_H + n_p \simeq 10^{20}$. The corresponding cloud temperature needed to give the observed $H\alpha$ equivalent width lies in the range 8000 to 9000 K, and the internal motions of the clouds range from less than 2 km s^{-1} to more than 14 km s^{-1} .

The cross-sectional areas of all the clouds studied in CaII $H \& K$ and $H\alpha$ were in the range 0.15 to 0.20 times the projected area of the stellar disc. For a column density of 10^{20} cm^{-2} , this gives a mass of $4 \text{ to } 5 \times 10^{17} \text{ g}$ per cloud. The amount of energy needed to increase the turbulent velocity dispersion of such a cloud from ~ 5 to $\sim 15 \text{ km s}^{-1}$ is of order $5 \times 10^{29} \text{ erg}$ – a small fraction of the $\sim 10^{34} \text{ erg}$ released in 0.1 to 10 keV X-rays by a single large flare on AB Dor (Collier Cameron *et al.* 1988)..

The energy budget for disposing of between 90 and 99 percent of the material in three clouds between 1988 Dec 22 and 23 is considerably greater. A large fraction of the cool cloud material seen on 1988 Dec 22 material must either have been re-ionised, fallen back to the surface of the star or been ejected from the corona by Dec 23. The amount of energy needed to re-heat most of the material in a $4 \times 10^{17} \text{ g}$ cloud to the ambient coronal temperature of $2 \times 10^7 \text{ K}$ is of order 10^{33} erg . Alternatively, the confining field may have contracted, dragging the cloud down to a position inside the co-rotation radius, where the dense cloud material is free to drain back on to the chromosphere, releasing 10^{32} to 10^{33} erg of gravitational energy per cloud as it goes. A third possibility is that part of each cloud may have undergone centrifugal ejection from the confining field, again releasing at least 10^{33} erg of magnetic energy from the stressed magnetic configuration. However, the apparent stability of the radial positions and projected areas of these three clouds, and the lack of any obvious bulk motions (absorption blueshifts or

redshifts) during the period 1988 Dec 21 to 23, tends to argue against any hypothesis requiring all three clouds to shed most of their contents in such a spectacular fashion in the course of 24 hours.

6 Conclusions

The new techniques developed in this paper for measuring the strength of the $H\alpha$, CaII $H \& K$ and MgII $h \& k$ absorption along lines of sight intersecting a cool circumstellar cloud have been applied successfully to new optical and UV spectra of AB Dor. These measurements place important new constraints on the masses and internal velocity dispersions of the AB Dor cloud system. The average amount of $H\alpha$ absorption along lines of sight through several of the larger clouds shows little variation, either from night to night or from cloud to cloud. The CaII $H \& K$ absorption, however, can change dramatically from night to night in a given cloud. These changes correspond to changes of 1 or 2 orders of magnitude in the cloud column density at a fixed internal velocity dispersion. A more plausible explanation for these changes in the CaII $H \& K$ absorption is that the internal velocity dispersions of the clouds may vary in time over the range 5 to 20 km s^{-1} – possibly increasing in response to stellar flares – in a manner analogous to the activation of solar prominences. In this case, a column density $n_H + n_p = 10^{20} \text{ cm}^{-2}$ is consistent with all the observations. The projected cross-sectional areas of these clouds are 15 to 20 percent of the projected stellar disc area, giving total masses per cloud of 2 to $6 \times 10^{17} \text{ g}$.

The excitation temperature for hydrogen needed to match the observed $H\alpha$ EW is between 8000 and 9000 K. If we take into account the combined local gravitational and centrifugal acceleration, the pressure scale height in the clouds is thus a few hundred km. By analogy with solar quiescent prominences, where similar physical conditions prevail, we suspect that the cloud material may be concentrated in filamentary structures with local densities two to three orders of magnitude greater than the average cloud density. The amplitude of the turbulent velocity dispersion inferred from the CaII $H \& K$ absorption strength is similar to the amplitude of the random motions of filaments within quiescent solar prominences.

At any given time there appear to be of order 6 to 10 large clouds in the observable slice of the corona, with allowance made for incomplete phase coverage. The actual number of clouds

is probably at least twice this number, giving a total mass for the cloud system of order 10^{19} g.

Acknowledgments ACC thanks the director and staff of the Anglo-Australian Observatory, for support at the telescope and for the use of the VAX 11/780 computer at AAO Epping, where the early stages of the data reduction were carried out. BHF and PE thank the staff of the European Southern Observatory for their support during the La Silla observations. MVP thanks the Institute of Astronomy, Cambridge for hospitality during the period over which this work was carried out, and the staff at Vilspa for support during the ESA *IUE* observations. The later stages of the data analysis were performed on the STARLINK VAX 11/780 at the Royal Greenwich Observatory. During the course of this work ACC was supported in a SERC-funded postdoctoral fellowship at the University of Sussex. An EEC grant to BHF for research into stellar activity is also acknowledged.

References

- [1] Ayres, T.R., 1979. *Astrophys. J.*, **228**, 509.
- [2] Basri, G.S. & Linsky, J.L., 1979. *Astrophys. J.*, **234**, 1023.
- [3] Bruzek, A., 1969. In de Jager, C. & Svestka, Z., editors, *Solar Flares and Space Research*, page 61, North-Holland, Amsterdam.
- [4] Collier Cameron, A., Bedford, D.K., Rucinski, S.M., Vilhu, O., & White, N.E., 1988. *Mon. Not. R. astr. Soc.*, **231**, 131-147.
- [5] Collier Cameron, A. & Robinson, R.D., 1989a. *Mon. Not. R. astr. Soc.*, **236**, 57.
- [6] Collier Cameron, A. & Robinson, R.D., 1989b. *Mon. Not. R. astr. Soc.*, **238**, 657.
- [7] Diego, F. & Walker, D.D., 1985. *Mon. Not. R. astr. Soc.*, **217**, 347.
- [8] Eggen, O.J., 1973. *Publ. astr. Soc. Pacif.*, **85**, 289.
- [9] Eggen, O.J., 1975. *Publ. astr. Soc. Pacif.*, **87**, 37.
- [10] Eggen, O.J., 1983. *Mon. Not. R. astr. Soc.*, **204**, 377.
- [11] Eggen, O.J., 1983. *Mon. Not. R. astr. Soc.*, **204**, 391.
- [12] Engvold, O., 1972. *Solar Phys.*, **23**, 346.
- [13] Innis, J.L., Thompson, K., & Coates, D.W., 1986. *Mon. Not. R. astr. Soc.*, **223**, 183.
- [14] Lampton, M., Margon, B., & Bowyer, S., 1976. *Astrophys. J.*, **208**, 177.
- [15] Lites, B.W., Skumanich, A., Rees, D.E., Murphy, G.A., & Carlsson, M., 1987. *Astrophys. J.*, **318**, 930.
- [16] Nakagawa, Y. & Malville, J.M., 1969. *Solar Phys.*, **9**, 102.
- [17] Pakull, M.W., 1981. *Astr. Astrophys.*, **104**, 33.
- [18] Pasquini, L. & D'Odorico, S., 1989. CASPEC: ESO Operating Manual 2, European Southern Observatory.

- [19] Press, W.H., Flannery, B.P., Teukolsky, S.A., & Vetterling, W.T., 1986. *Numerical Recipes: The Art of Scientific Computing*. Cambridge University Press, Cambridge.
- [20] Robinson, R.D. & Collier Cameron, A., 1986. *Proc. Astr. Soc. Australia*, **6**, 308.
- [21] Rucinski, S.M., 1982. *Inf. Bull. var. Stars*, **2203**.
- [22] Rucinski, S.M., 1985. *Mon. Not. R. astr. Soc.*, **215**, 591-614.
- [23] Shine, R.A. & Linsky, J.L., 1974. *Solar Phys.*, **39**, 49.
- [24] Stauffer, J.R. & Hartmann, L.W., 1987. *Astrophys. J.*, **318**, 337.
- [25] Stauffer, J.R., Hartmann, L., Soderblom, D.R., & Burnham, N., 1984. *Astrophys. J.*, **280**, 202.
- [26] van Leeuwen, F. & Alphenaar, P., 1983. In Rodono, M. & Byrne, P.B., editors, *IAU Colloquium 71, Activity in Red Dwarf Stars*, Reidel.
- [27] van Leeuwen, F., Alphenaar, P., & Meys, J.M.M., 1987. *Astr. Astrophys. Suppl.*, **67**, 483 - 506.
- [28] Vilhu, O. & Linsky, J.L., 1987. *Publ. astr. Soc. Pacif.*, **99**, 1071.
- [29] Vilhu, O., Gustafsson, B., & Edvardsson, B., 1987. *Astrophys. J.*, **320**, 850.
- [30] Walker, D.D. & Diego, F., 1985. *Mon. Not. R. astr. Soc.*, **217**, 355.
- [31] Wilson, O.C. & Bappu, M.K.V., 1957. *Astrophys. J.*, **125**, 661.

Figure 1: A set of representative $H\alpha$ and CaII H and K spectra.

Each series of spectra traces the development of a typical cloud absorption transient. Panel (a) shows the development of a transient in $H\alpha$ on 1988 Dec 21. Panels (b) and (c) show smoothed reference spectra of the CaII H & K lines. These reference spectra were subtracted from the observed spectra to give the time-series of CaII H & K difference spectra in panels (d) and (e). These were obtained over the same range of rotation phases as (a), on 1988 Dec 22, and are plotted on the same vertical scale as (b) and (c).

Figure 2: $H\alpha$ absorption equivalent width plotted against central absorption depth.

A total of 12 width-depth relations for individual clouds are shown, measured from the dynamic spectra of (a) 1988 Dec 16, (b) Dec 17, (c) Dec 19, (d) Dec 21 and (e) Dec 23. The slope of each plot gives the average $H\alpha$ absorption equivalent width \bar{w} for a single line of sight through the cloud.

Figure 3: $H\alpha$ absorption EW plotted against UT on 1988 Dec 22.

The variation of $H\alpha$ EW with rotation phase on 1988 Dec 22 was assumed to be the mean of the values observed at the same rotation phase on Dec 21 and 23. The dot-dashed curve shows the difference between the EWs observed on Dec 21 and 23. The horizontal solid line segments denote the three phase ranges over which the CaII H & K index - $H\alpha$ EW relations for Dec 22 were calculated. Although some changes in the cloud distribution clearly occurred between Dec 21 and Dec 23, the night-to-night changes over these phase ranges were small compared to the amplitude of the phase-dependent EW variation.

Figure 4: CaII H and K line index plotted against H α absorption equivalent width. Data are given for each of the CaII *H* & *K* lines in each echelle order observed, for a total of eight transients observed on (a) 1988 Dec 19, (b) Dec 22 and (c) Dec 23. The slope of each plot gives the value of $\bar{i}_{K,H}/\bar{w}$ for a single line of sight through the cloud.

Figure 5: MgII h and k line index plotted against H α absorption equivalent width. The line indices for the five *IUE* LWP spectra obtained on 1988 Dec 17 are shown as open circles. The slope of each plot gives the average value of $\bar{i}_{k,h}/\bar{w}$ for a single line of sight through the cloud material obscuring the disc at the time of observation.

Figure 6: Intrinsic H α absorption EW as a function of $n_{n=2}$ and v_{turb} .

Figure 7: Intrinsic H α absorption EW as a function of $n_H + n_p$ and T_{cloud} .
The cloud thickness is 7.3×10^{10} cm and the turbulent velocity dispersion is $v_{\text{turb}} = 10 \text{ km s}^{-1}$.

Figure 8: Intrinsic H α absorption EW as a function of $n_H + n_p$ and T_{cloud} .
The cloud thickness is 7.3×10^7 cm and the turbulent velocity dispersion is $v_{\text{turb}} = 10 \text{ km s}^{-1}$.
This simulates a fragmented cloud, in which the condensed cloud material occupies only 10^{-3} times the total cloud volume.

Figure 9: CaII H and K absorption line index map.

Contours of constant (a) i_K and (b) i_H are plotted as a function of total hydrogen column density $n_H + n_p$ and turbulent velocity dispersion v_{turb} . From bottom to top, contour levels are 0.1, 0.2, 0.3, 0.4, 0.5, 0.6, 0.7, 0.8, 0.9.

Figure 10: CaII H and K line index plotted against total hydrogen column density

The solid curve shows the variation of the line index with column density, for zero turbulent velocity dispersion and a gaussian chromospheric emission profiles with $\text{FWHM} = 0.43\text{\AA}$. The effects of increasing or decreasing the chromospheric emission width by 0.04\AA are shown by the dashed and dotted curves respectively. The effect of introducing a turbulent gaussian velocity dispersion of 4 km s^{-1} is shown by the dot-dashed curve.

Figure 11: Confidence limits on cloud parameters from CaII H and K data.

The 95.4% and 99% confidence limits on the cloud parameters are shown in the $(n_H + n_p, v_{\text{turb}})$ plane. The confidence limits are contours of constant χ^2 , for all the data available on each of the eight individual absorption transients studied.

Figure 12: MgII h and k absorption line index map.

Contours of constant (a) i_k and (b) i_h are plotted as a function of total hydrogen column density $n_H + n_p$ and turbulent velocity dispersion v_{turb} . From bottom to top, contour levels are 0.1, 0.2, 0.3, 0.4, 0.5, 0.6, 0.7, 0.8, 0.9.

Figure 13: MgII h and k line index plotted against total hydrogen column density.

The solid curve shows the variation of the line index with column density, for zero turbulent velocity dispersion and a gaussian chromospheric emission profiles with $\text{FWHM} = 0.66\text{\AA}$. The effects of increasing or decreasing the chromospheric emission width by 0.06\AA are shown by the dashed and dotted curves respectively. The effect of introducing a turbulent gaussian velocity dispersion of 4 km s^{-1} is shown by the dot-dashed curve.

Figure 14: Confidence limits on cloud parameters from MgII h and k data.

The 95.4% and 99% confidence limits on the cloud parameters are shown in the $(n_H + n_p, v_{\text{turb}})$ plane. The confidence limits are contours of constant χ^2 , for a fit to the MgII h & k data obtained on 1988 Dec 17.

Table 1: Journal of observations			
UT Date 1988	Ground-based optical		<i>IUE</i>
	H α	CaII <i>H</i> & <i>K</i>	MgII <i>h</i> & <i>k</i>
Dec 16	<i>AAT</i> 12:22 - 17:40	—	—
Dec 17	<i>AAT</i> 10:15 - 17:56	—	ESA 09:51 - 16:40
Dec 18	<i>AAT</i> 16:29 - 17:56	—	—
Dec 19	<i>AAT</i> 10:42 - 18:04	<i>AAT</i> 11:58 - 17:42	ESA 13:19 - 16:17
Dec 21	<i>ESO</i> 01:29 - 08:40	—	—
Dec 22	—	<i>ESO</i> 01:50 - 07:45	—
Dec 23	<i>ESO</i> 02:49 - 08:01	<i>ESO</i> 03:08 - 08:07	—
Dec 24	—	—	—
Dec 25	—	—	US2 01:16 - 08:11
Dec 25	—	—	US1 17:17 - 23:11
Dec 26	—	—	US2 00:29 - 05:59

Table 2: MgII h and k emission flux measurements. All fluxes are in units of 10^{-12} erg cm² s⁻¹.

LWP No	Line	Measured Flux	Absorbed Flux	Corrected Flux	Fitted Flux	Ratio
14655	k	2.97±0.14	0.92±0.02	3.88±0.14	4.87±0.12	1.25
14655	h	3.46±0.09	0.75±0.01	4.21±0.10	4.66±0.09	1.10
14656	k	2.18±0.13	0.63±0.02	2.82±0.13	3.94±0.12	1.40
14656	h	2.51±0.08	0.49±0.01	3.00±0.08	3.43±0.08	1.14
14657	k	2.39±0.13	0.70±0.02	3.10±0.13	4.26±0.12	1.37
14657	h	3.07±0.10	0.63±0.01	3.70±0.10	4.17±0.10	1.13
14658	k	1.87±0.13	0.56±0.02	2.42±0.13	3.61±0.12	1.49
14658	h	2.25±0.08	0.50±0.01	2.75±0.08	3.19±0.08	1.16
14659	k	2.50±0.13	0.87±0.02	3.37±0.13	4.39±0.12	1.30
14659	h	3.33±0.08	0.69±0.01	4.02±0.08	4.47±0.08	1.11
14672	k	1.27±0.15	0.46±0.02	1.73±0.15	2.71±0.14	1.57
14672	h	1.60±0.09	0.39±0.01	1.99±0.09	2.33±0.08	1.17
14673	k	2.56±0.14	0.83±0.02	3.39±0.14	4.52±0.13	1.33
14673	h	2.93±0.08	0.67±0.01	3.60±0.08	4.01±0.08	1.11
14674	k	2.52±0.13	0.74±0.02	3.26±0.13	4.48±0.12	1.37
14674	h	2.71±0.08	0.62±0.01	3.33±0.08	3.72±0.07	1.12
14708	k	3.27±0.13	1.08±0.02	4.35±0.13	5.40±0.11	1.24
14708	h	3.73±0.09	0.87±0.01	4.60±0.09	4.88±0.08	1.06
14709	k	3.81±0.13	0.98±0.02	4.78±0.14	5.99±0.13	1.25
14709	h	4.28±0.12	0.84±0.02	5.13±0.12	5.56±0.11	1.08
14710	k	2.65±0.10	0.78±0.02	3.43±0.10	4.50±0.09	1.31
14710	h	2.92±0.05	0.68±0.01	3.60±0.06	3.91±0.05	1.09
14713	k	2.79±0.09	0.74±0.01	3.54±0.10	4.83±0.09	1.37
14713	h	2.93±0.06	0.65±0.01	3.58±0.06	3.95±0.06	1.10
14715	k	3.40±0.09	0.95±0.01	4.35±0.09	5.60±0.09	1.29
14715	h	3.06±0.06	0.78±0.01	3.84±0.07	4.20±0.06	1.10
14716	k	3.34±0.07	0.92±0.01	4.26±0.07	5.49±0.07	1.29
14716	h	3.19±0.05	0.68±0.01	3.87±0.06	4.36±0.05	1.12
14717	k	3.32±0.10	0.98±0.02	4.29±0.10	5.44±0.09	1.27
14717	h	3.68±0.06	0.79±0.01	4.47±0.06	4.79±0.05	1.07
14718	k	2.42±0.13	0.70±0.02	3.12±0.13	4.33±0.12	1.39
14718	h	2.77±0.06	0.59±0.01	3.35±0.06	3.78±0.06	1.13

Table 3: Area-weighted mean cloud H α absorption EW.

Values for individual clouds are derived from absorption EW-depth relations.

Date	Start UT	End UT	Mean Intrinsic H α EW (channels)	\bar{w} (Å)
1988 Dec 16	12:56	14:12	30.76 ± 5.32	1.82 ± 0.31
1988 Dec 16	15:30	16:13	45.32 ± 2.11	2.68 ± 0.16
1988 Dec 17	10:35	11:10	51.62 ± 3.42	3.05 ± 0.20
1988 Dec 17	13:35	14:53	38.56 ± 3.07	2.28 ± 0.18
1988 Dec 17	16:12	16:44	52.16 ± 2.29	3.08 ± 0.14
1988 Dec 19	14:48	16:08	35.99 ± 1.53	2.13 ± 0.09
1988 Dec 19	17:06	18:04	45.50 ± 3.66	2.69 ± 0.22
1988 Dec 21	03:37	04:01	33.00 ± 0.92	1.95 ± 0.05
1988 Dec 21	04:40	05:00	46.39 ± 2.28	2.74 ± 0.13
1988 Dec 21	06:33	06:46	42.69 ± 4.74	2.52 ± 0.28
1988 Dec 23	04:53	05:43	48.53 ± 2.87	2.87 ± 0.17
1988 Dec 23	05:55	06:33	49.14 ± 2.90	2.90 ± 0.17
1988 Dec 23	07:36	08:01	50.91 ± 3.01	3.01 ± 0.18

Table 4: Atomic parameters and line broadening coefficients

	H α	CaII K	CaII H	MgII k	MgII h
A_E	—	2.27(-6)	2.27(-6)	3.34(-5)	3.34(-5)
At. wt.	1.0	40	40	24	24
f_{lu}	0.641	0.66	0.33	0.63	0.31
λ_0	6562.808	3933.644	3968.470	2795.53	2802.70
Γ_R	5.698(8)	1.50(8)	1.50(8)	2.70(8)	2.70(8)
G_{VW}	3.85(-8)	1.6(-8)	1.6(-8)	1.4(-8)	1.4(-8)
G_{res}	5.877(-7)	—	—	—	—

Notes:

1. $\Gamma = \Gamma_R + N_H(G_{VW}(T/5000)^{0.3} + G_{res})$
2. Ca II broadening coefficients from Shine & Linsky (1974)
3. H α and Mg II broadening coefficients from Lites *et al.* (1987)

Date	Table 5: Observed CaII H and K index - H α EW relations				
	UT Start	UT End	Échelle Order	dI_K/dW (Å)	dI_H/dW
1988 Dec 19	14:41	16:19	143	—	0.125 ± 0.027
1988 Dec 19	14:41	16:19	144	0.188 ± 0.037	—
1988 Dec 19	16:39	17:42	143	—	0.071 ± 0.025
1988 Dec 19	16:39	17:42	144	0.261 ± 0.071	—
1988 Dec 22	04:12	04:53	087	0.299 ± 0.022	0.171 ± 0.014
1988 Dec 22	04:12	04:53	088	0.256 ± 0.020	—
1988 Dec 22	05:28	06:03	087	0.152 ± 0.021	0.071 ± 0.013
1988 Dec 22	05:28	06:03	088	0.171 ± 0.019	—
1988 Dec 22	07:16	07:45	087	0.300 ± 0.032	0.207 ± 0.020
1988 Dec 22	07:16	07:45	088	0.030 ± 0.029	—
1988 Dec 23	04:47	05:49	143	—	0.061 ± 0.013
1988 Dec 23	04:47	05:49	144	0.083 ± 0.016	—
1988 Dec 23	04:47	05:49	145	0.044 ± 0.023	—
1988 Dec 23	06:01	06:52	143	—	0.027 ± 0.011
1988 Dec 23	06:01	06:52	144	0.119 ± 0.014	—
1988 Dec 23	06:01	06:52	145	0.049 ± 0.020	—
1988 Dec 23	07:17	07:54	143	—	-0.009 ± 0.021
1988 Dec 23	07:17	07:54	144	0.025 ± 0.027	—
1988 Dec 23	07:17	07:54	145	0.050 ± 0.037	—

Table 6: Simultaneous MgII h and k index and H α EW measures.

Note that W is a time-averaged value, calculated over the duration of the corresponding IUE

	Date	UT Start	UT End	W (\AA)	I_K	I_H
exposure.	1988 Dec 17	09:51	10:26	0.20	0.00 ± 0.05	0.00 ± 0.03
	1988 Dec 17	11:40	12:20	0.57	0.27 ± 0.04	0.29 ± 0.03
	1988 Dec 17	12:50	13:30	0.52	0.20 ± 0.04	0.12 ± 0.03
	1988 Dec 17	14:04	14:44	0.79	0.38 ± 0.04	0.35 ± 0.02
	1988 Dec 17	16:00	16:40	0.49	0.13 ± 0.04	0.04 ± 0.03
	1988 Dec 19	13:20	13:55	0.35	0.55 ± 0.04	0.53 ± 0.02
	1988 Dec 19	14:29	15:04	0.22	0.13 ± 0.05	0.14 ± 0.03
	1988 Dec 19	15:37	16:17	0.43	0.16 ± 0.05	0.21 ± 0.03

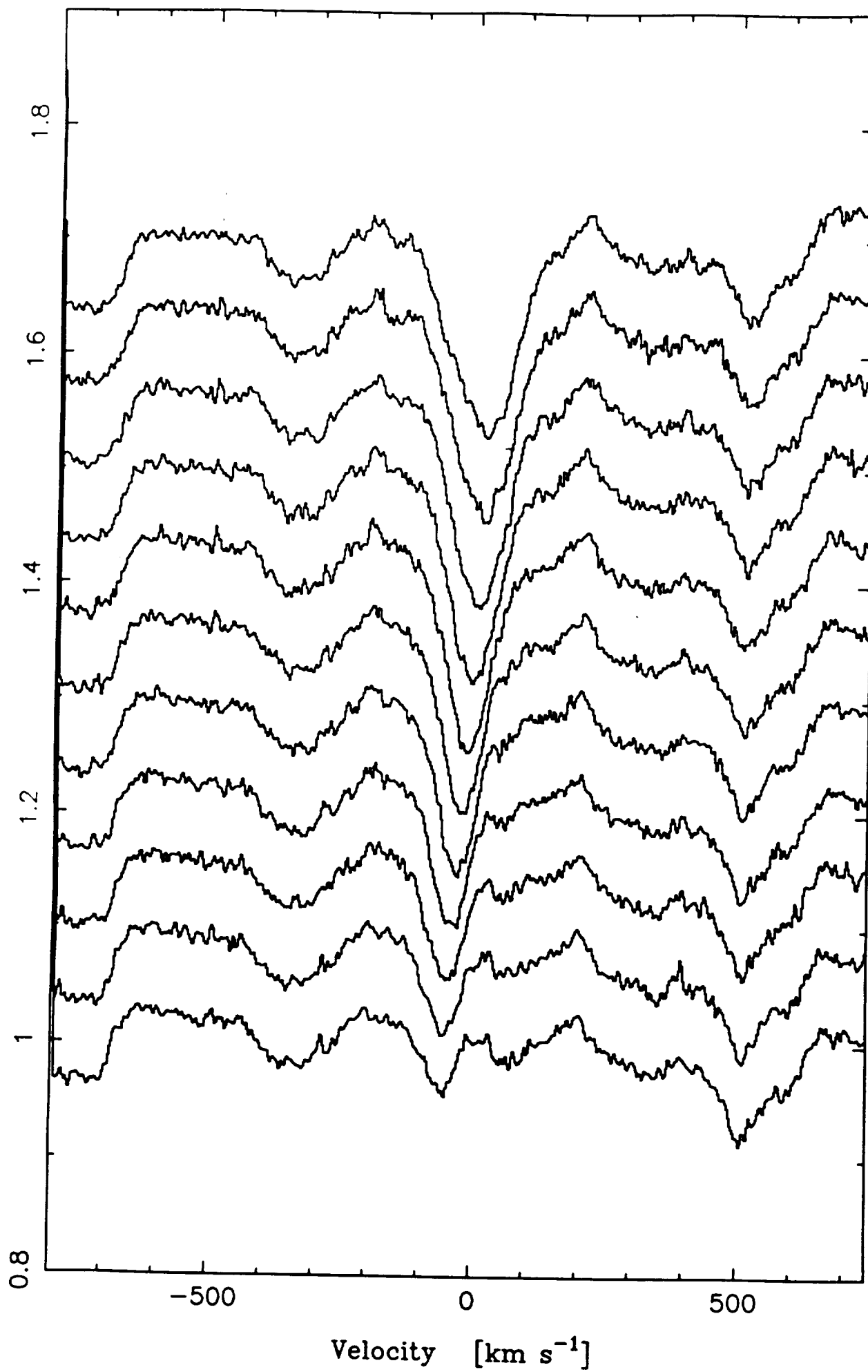
$n_H + n_p$	Table 7: Constraints on cloud temperature and velocity dispersion						
	T_{cloud} ($f = 1.000$)	T_{cloud} ($f = 0.001$)	MgII h & k				v_{turb} CaII
			Dec 17	Dec 19(1)	Dec 19(2)	Dec 22(1)	Dec 22(2)
10^{22}	6000 ± 200	6000 ± 200	Unc.	Excl.	< 3	< 2	Excl.
10^{21}	7000 ± 300	7000 ± 300	Unc.	< 3	Unc.	> 5	< 3
10^{20}	9000 ± 1000	8200 ± 400	> 5	2-10	Unc.	> 14	3-9
10^{19}	Excl.	12000 ± 2000	> 10	4-15	> 1	Excl.	5-14
10^{18}	Excl.	Excl.	> 15	> 10	> 4	Excl.	> 10

Table 7 overleaf.

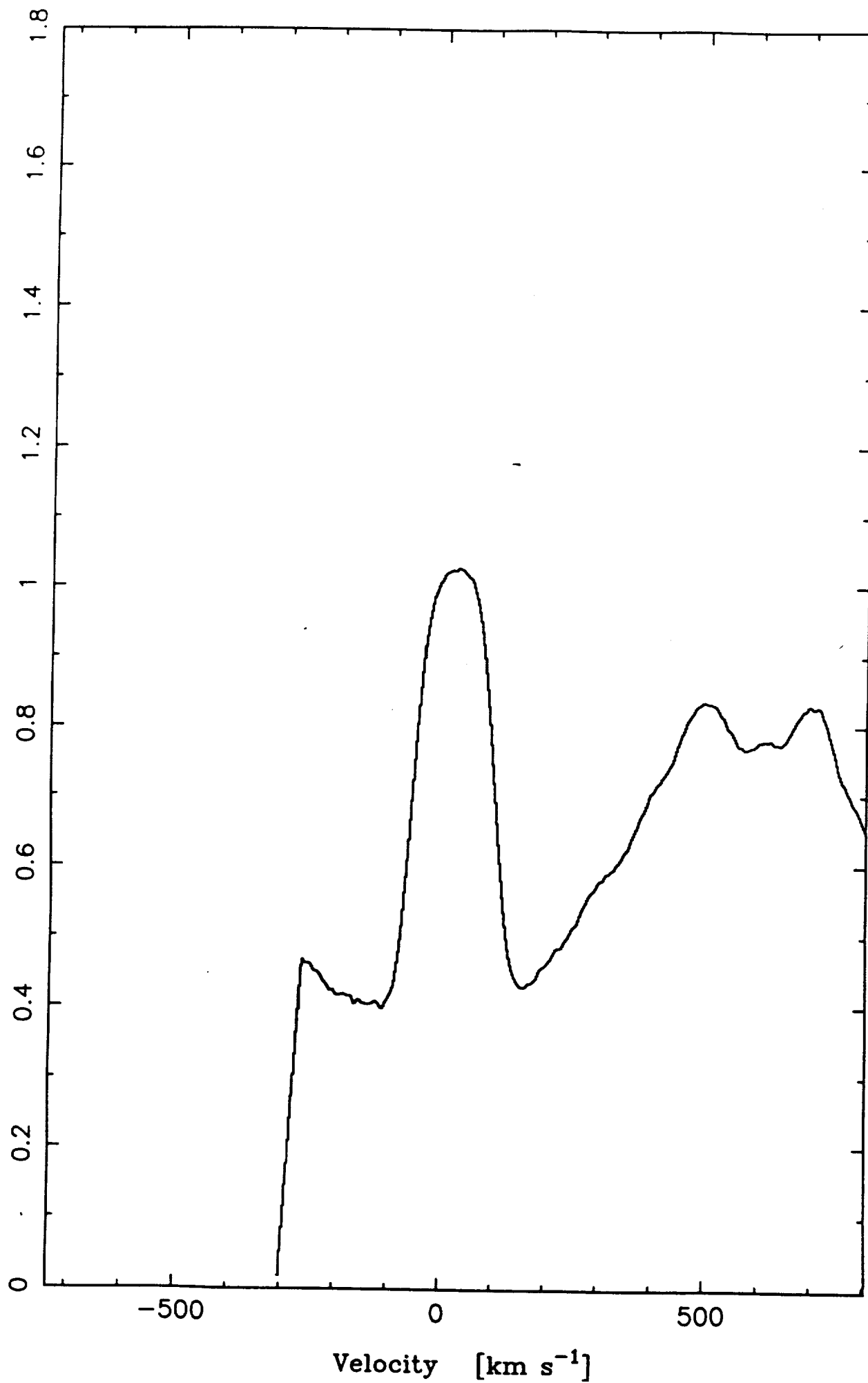
Table 7: Constraints on cloud temperature and velocity dispersion

$n_H + n_p$	T_{cloud} ($f = 1.000$)	T_{cloud} ($f = 0.001$)	Mg II h & k		v_{turb} Ca II H & K							
			Dec 17	Dec 19(1)	Dec 19(2)	Dec 22(1)	Dec 22(2)	Dec 22(3)	Dec 23(1)	Dec 23(2)	Dec 23(3)	
10^{22}	6000 ± 200	6000 ± 200	Unc.	Excl.	< 3	< 2	Excl.	< 2	Excl.	Excl.	Excl.	Excl.
10^{21}	7000 ± 300	7000 ± 300	Unc.	< 3	Unc.	> 5	< 3	> 4	Excl.	Excl.	Excl.	Excl.
10^{20}	9000 ± 1000	8200 ± 400	> 5	2-10	Unc.	> 14	3-9	> 8	< 4	< 3	< 2	< 2
10^{19}	Excl.	12000 ± 2000	> 10	4-15	> 1	Excl.	5-14	> 11	2-6	2-5	< 3	< 3
10^{18}	Excl.	Excl.	> 15	> 10	> 4	Excl.	> 10	Excl.	5-11	5-11	< 6	< 6

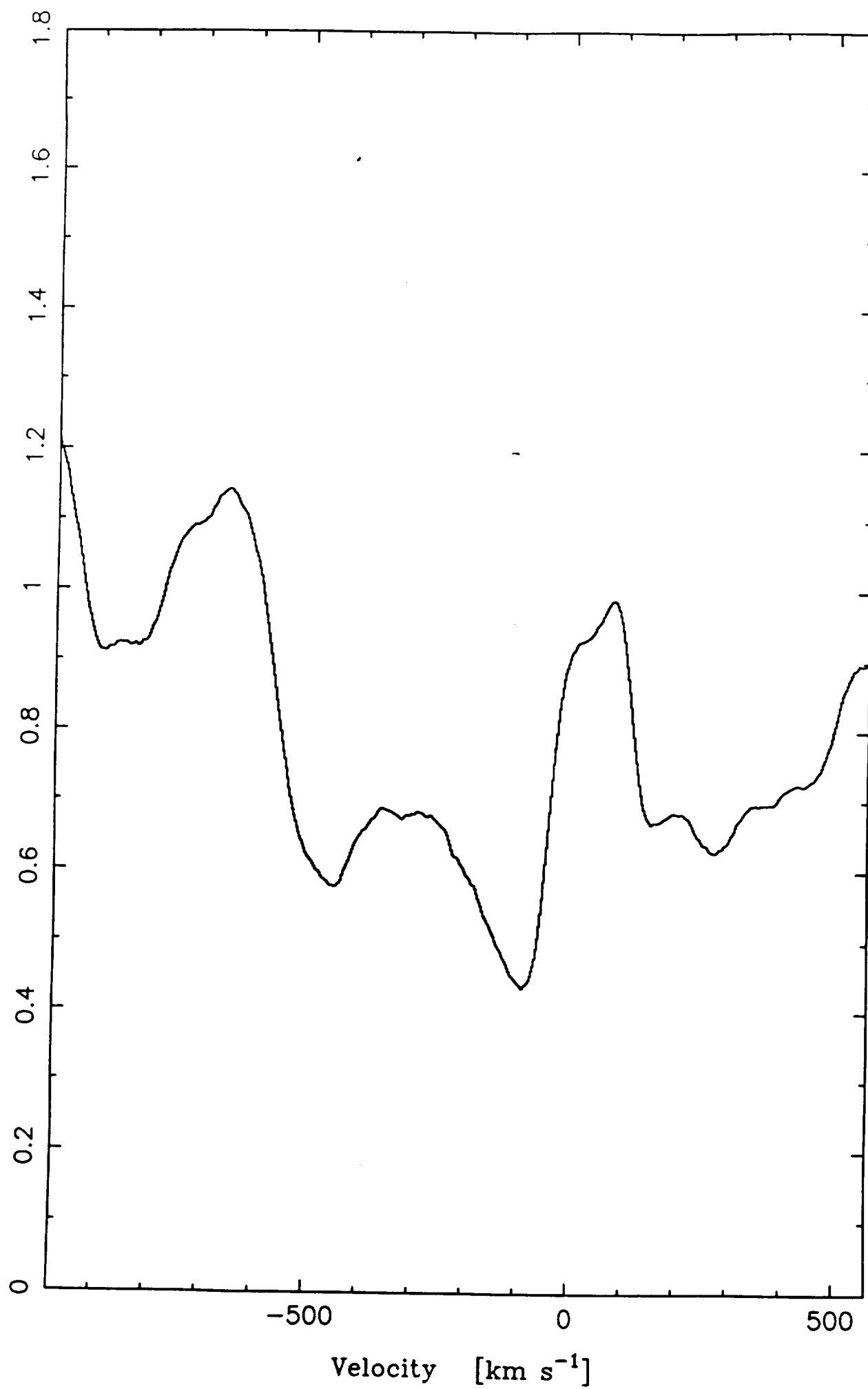
1988 Dec 21 04:24 to 05:23 H α



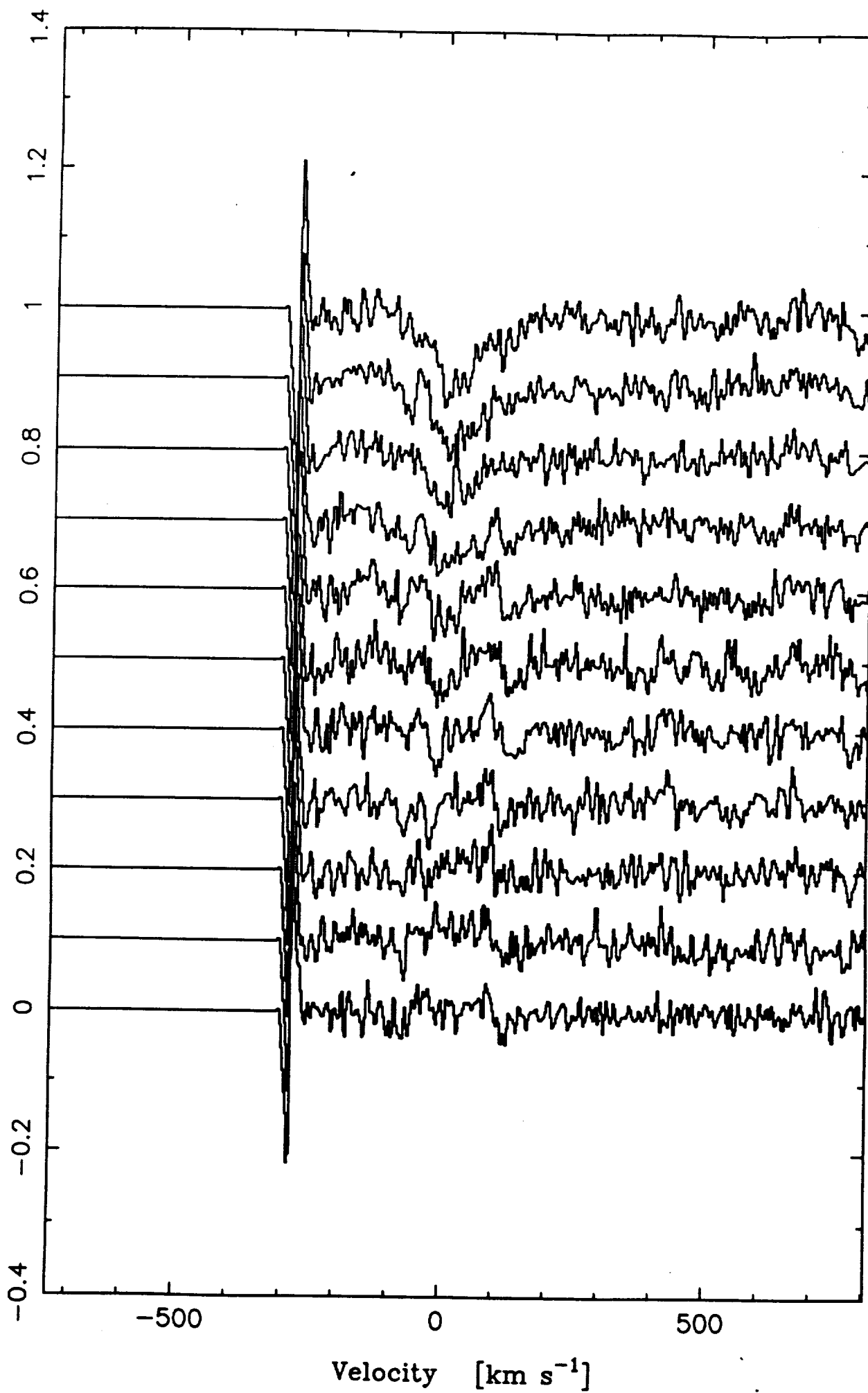
Ca II K reference spectrum



Ca II H + He reference spectrum



1988 Dec 22 05:05 to 06:04 Ca II K



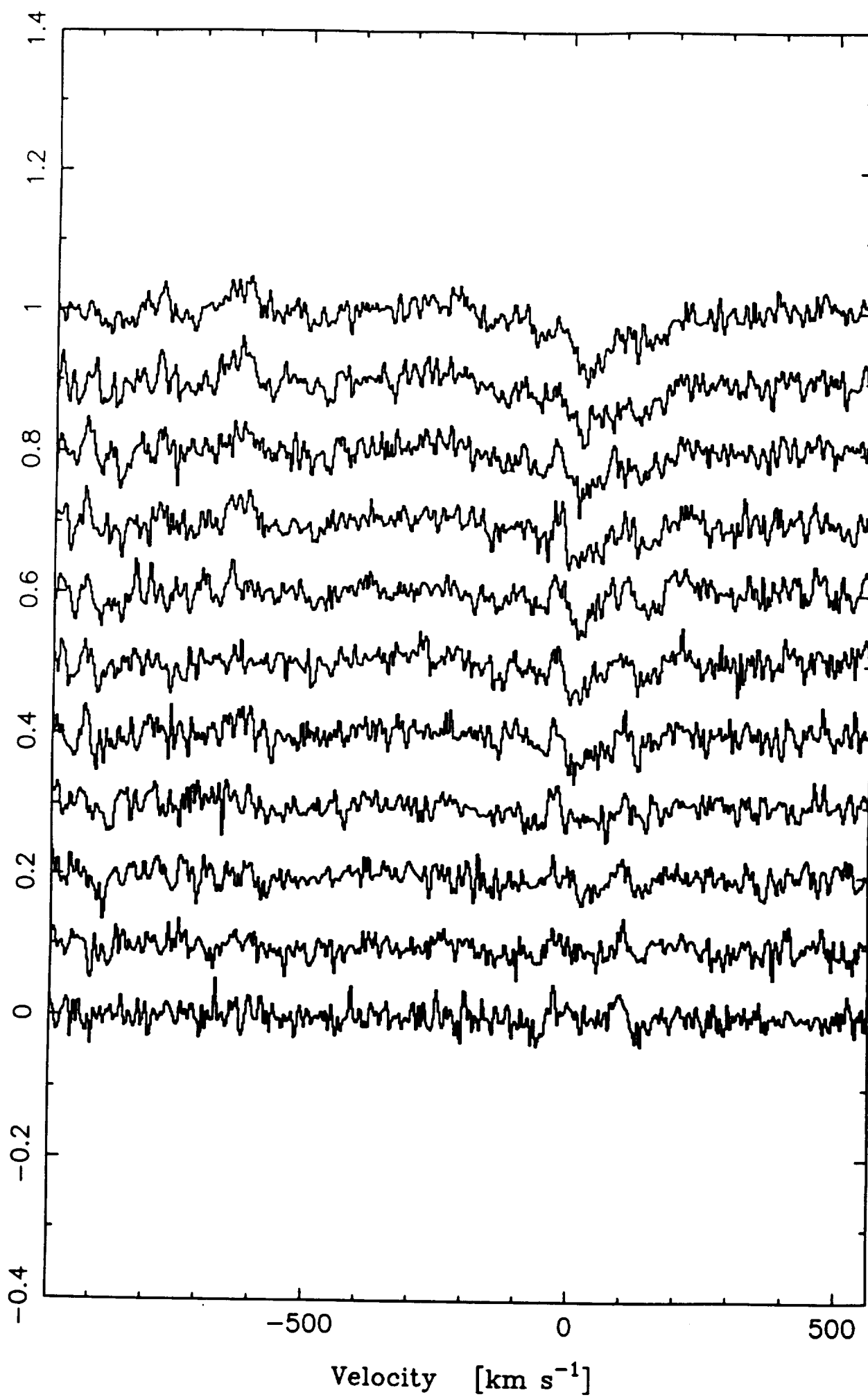


Fig. 2(a)

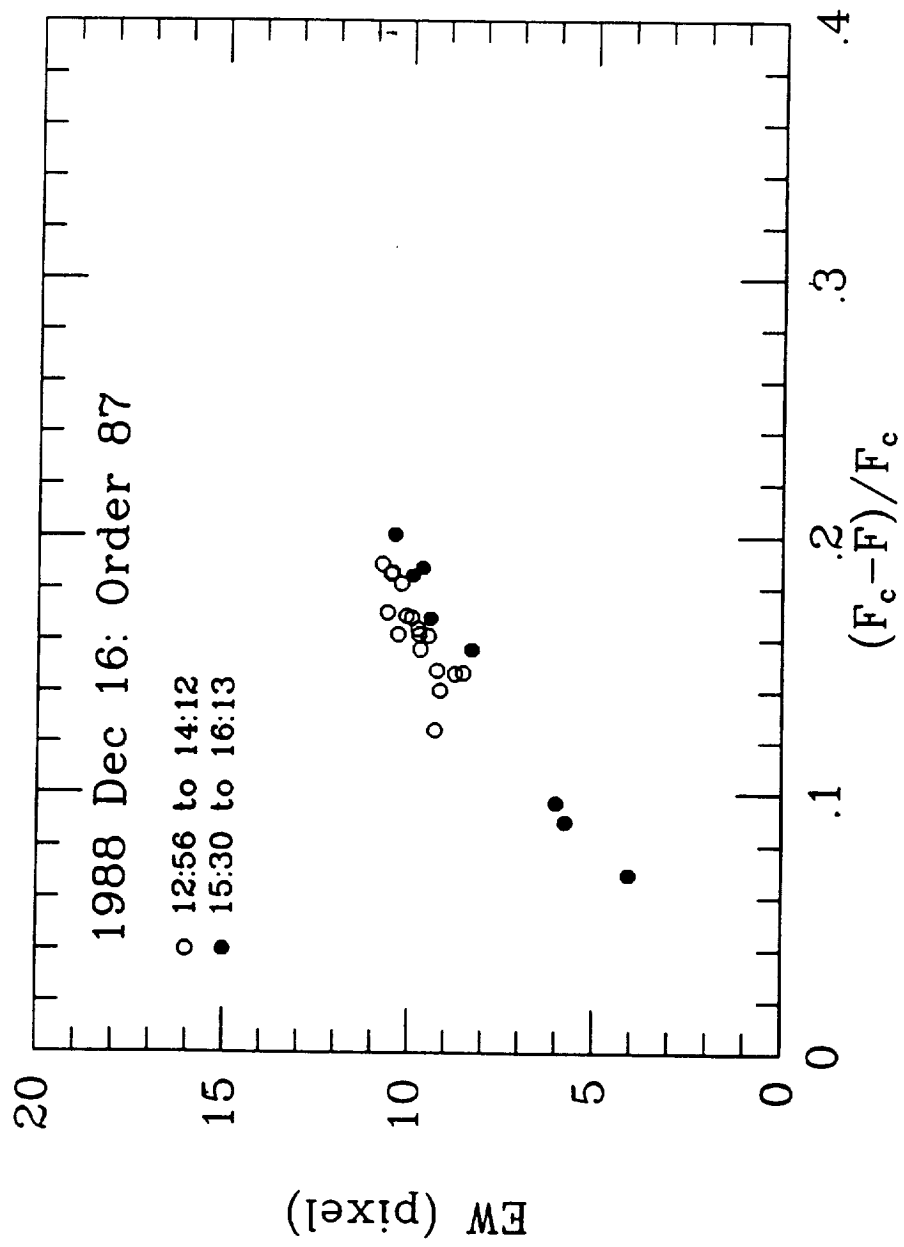


Fig. 2(b)

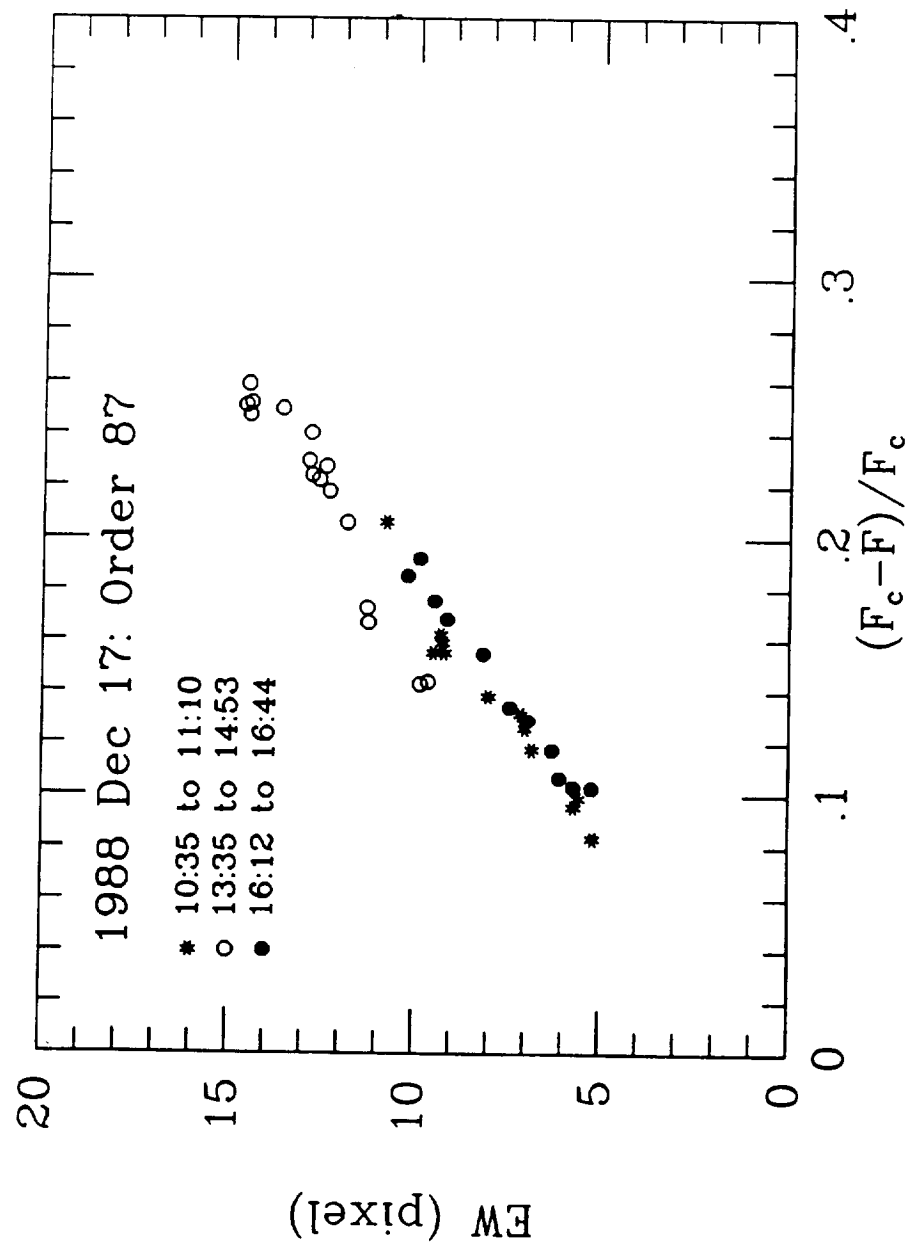


Fig. 2(c)

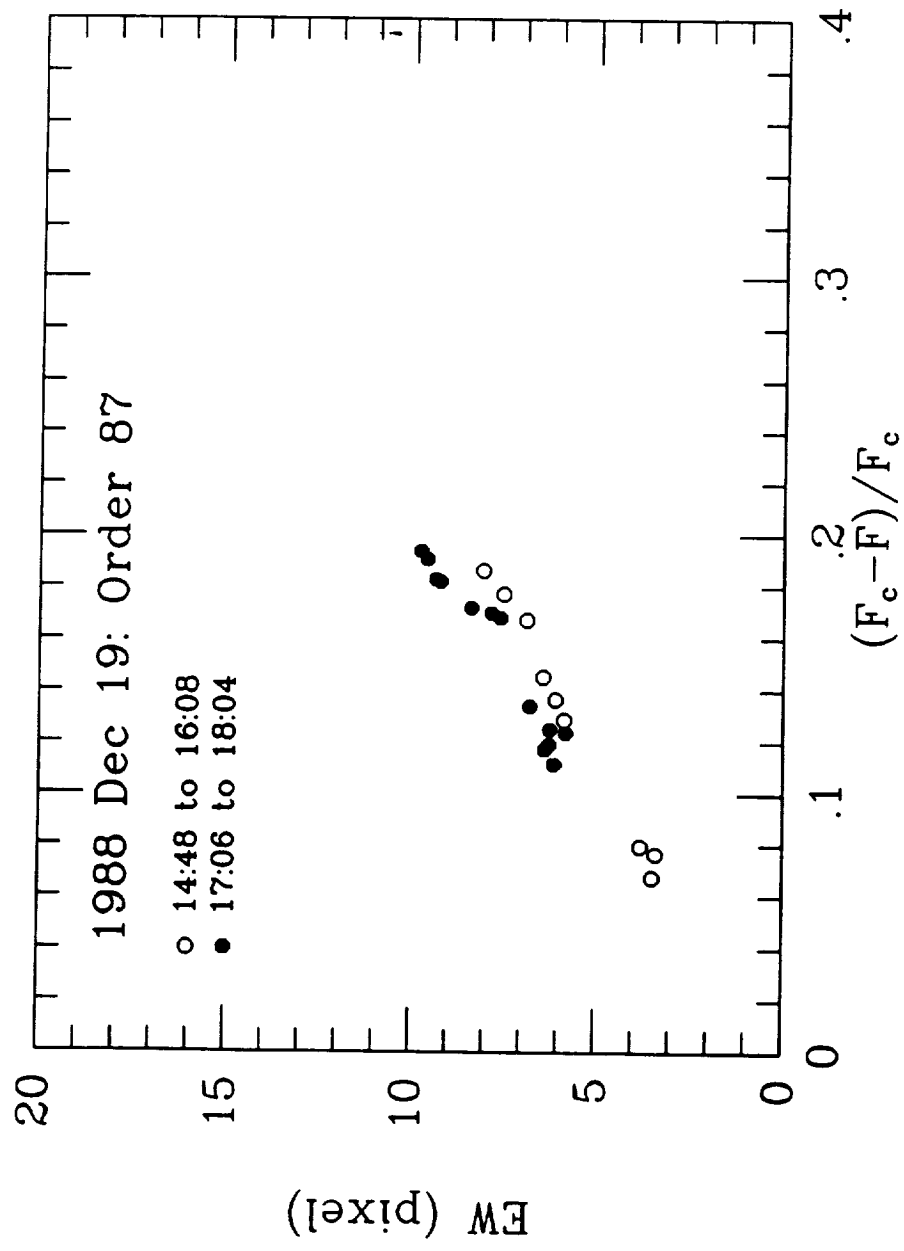


Fig 2 (d)

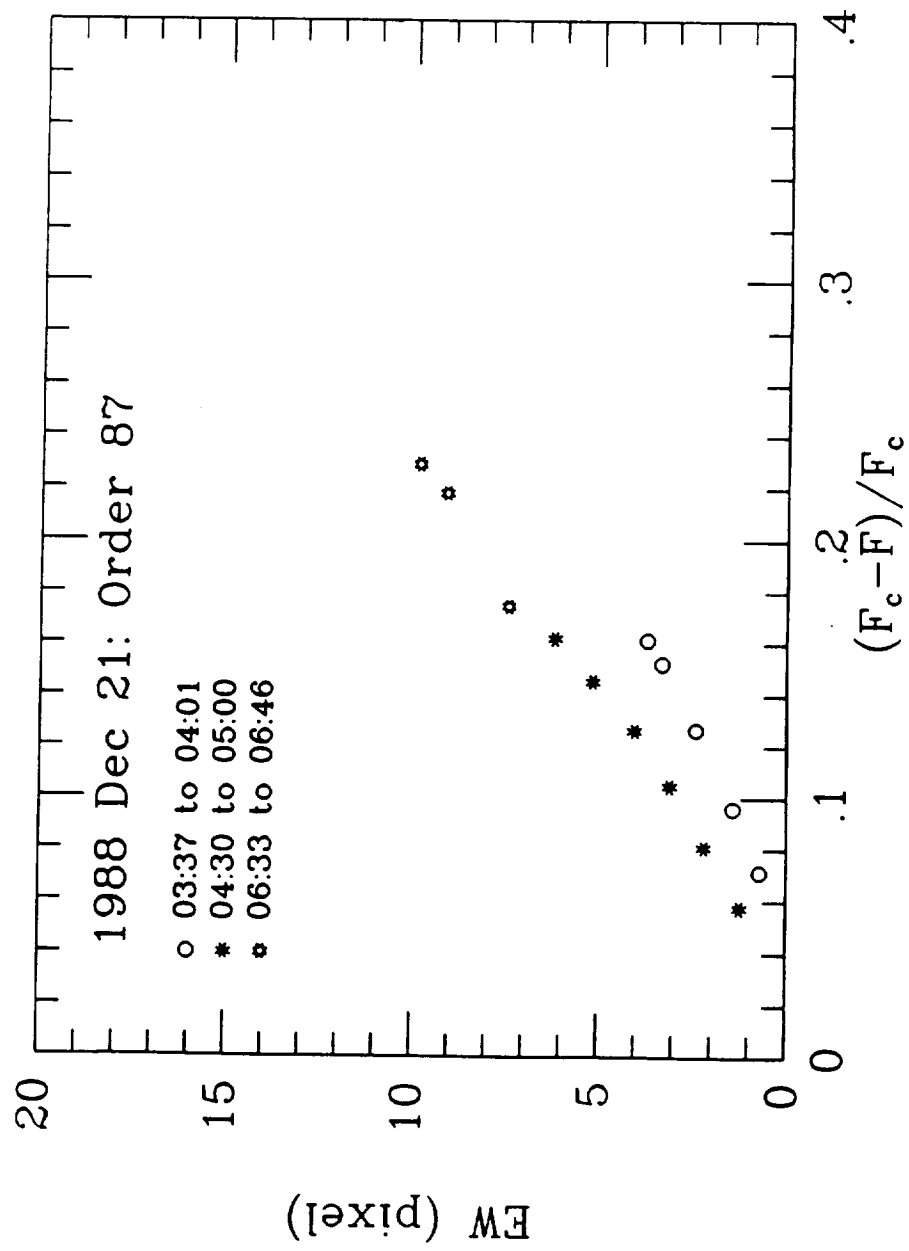


Fig 2 (e)

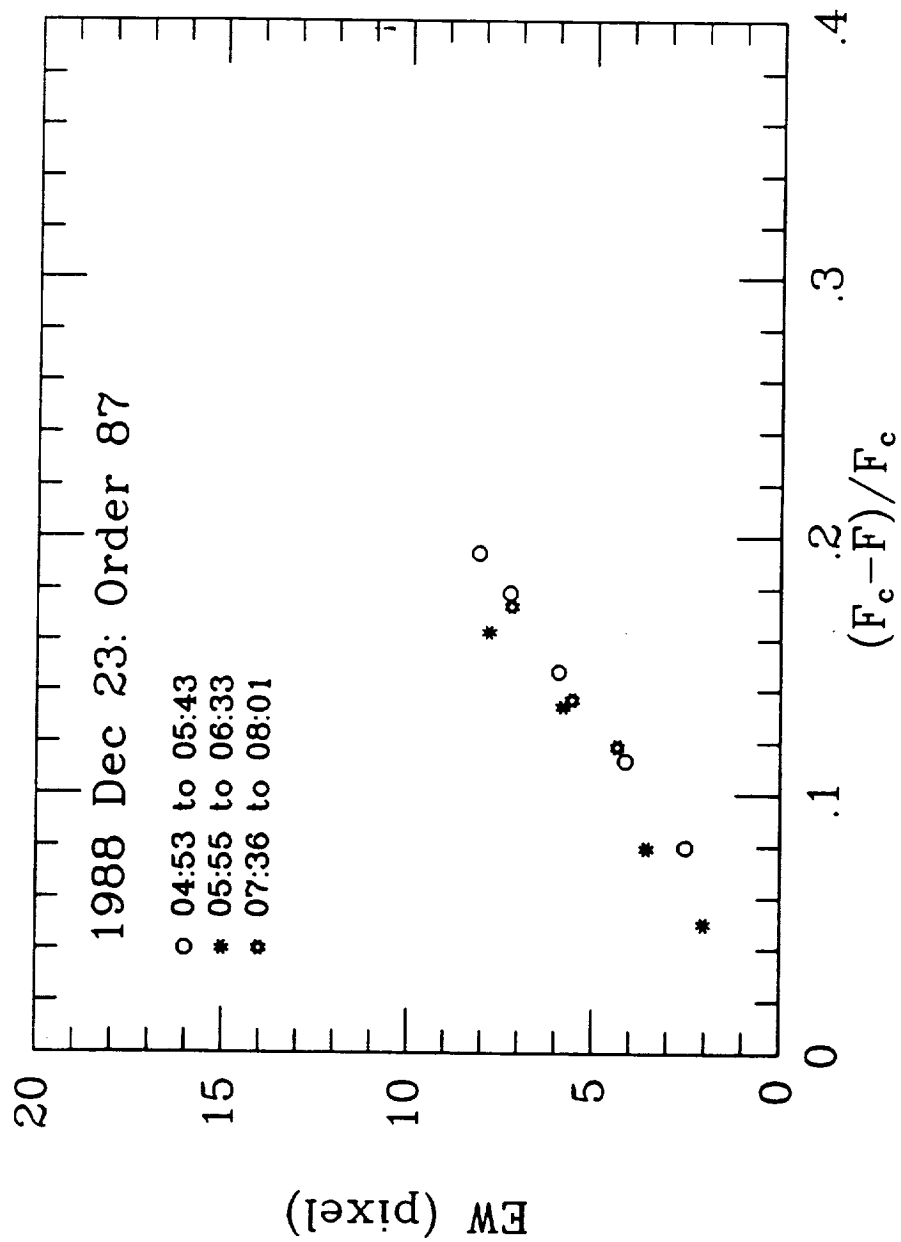


Fig. 3

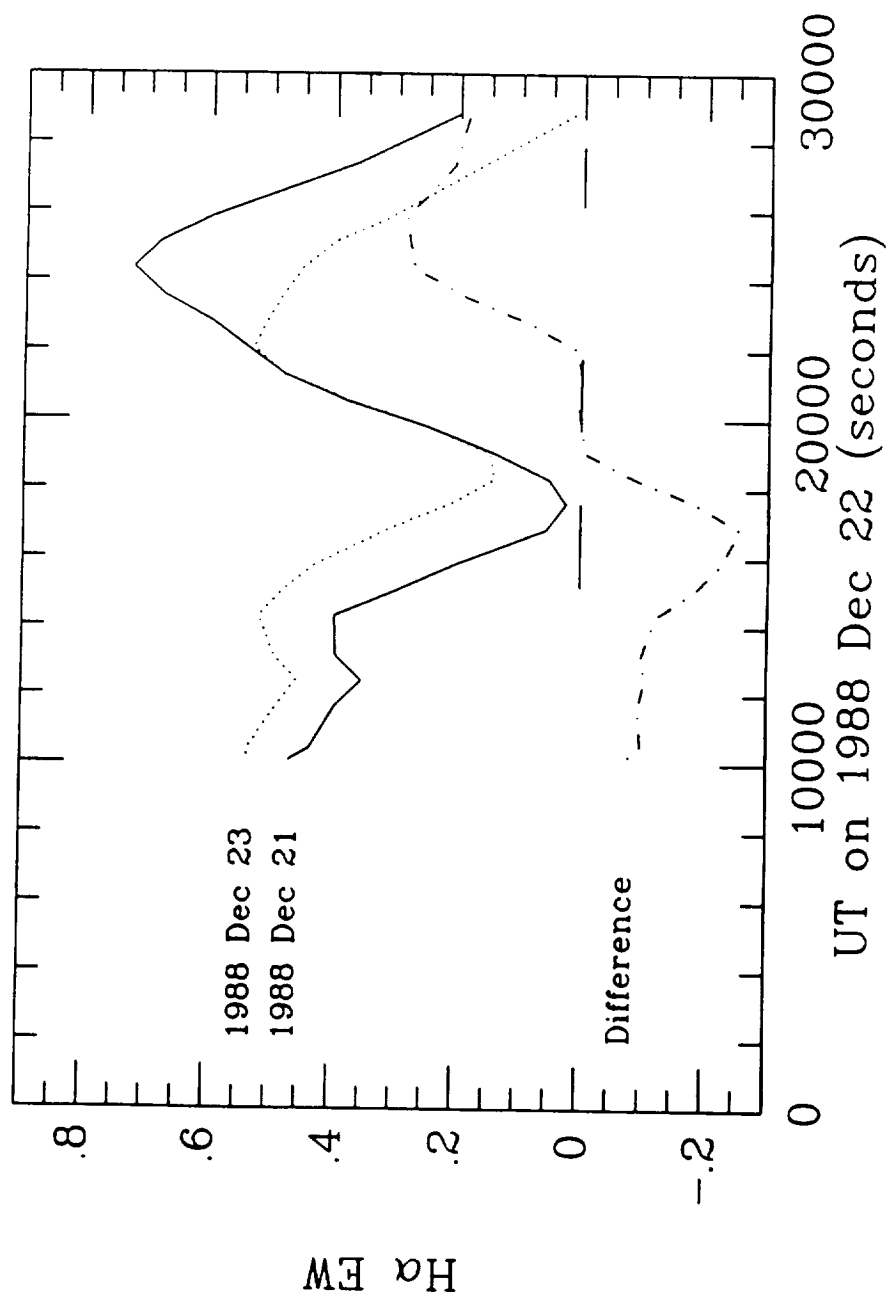


Fig. 4(a) - PANEL 1 OF 2

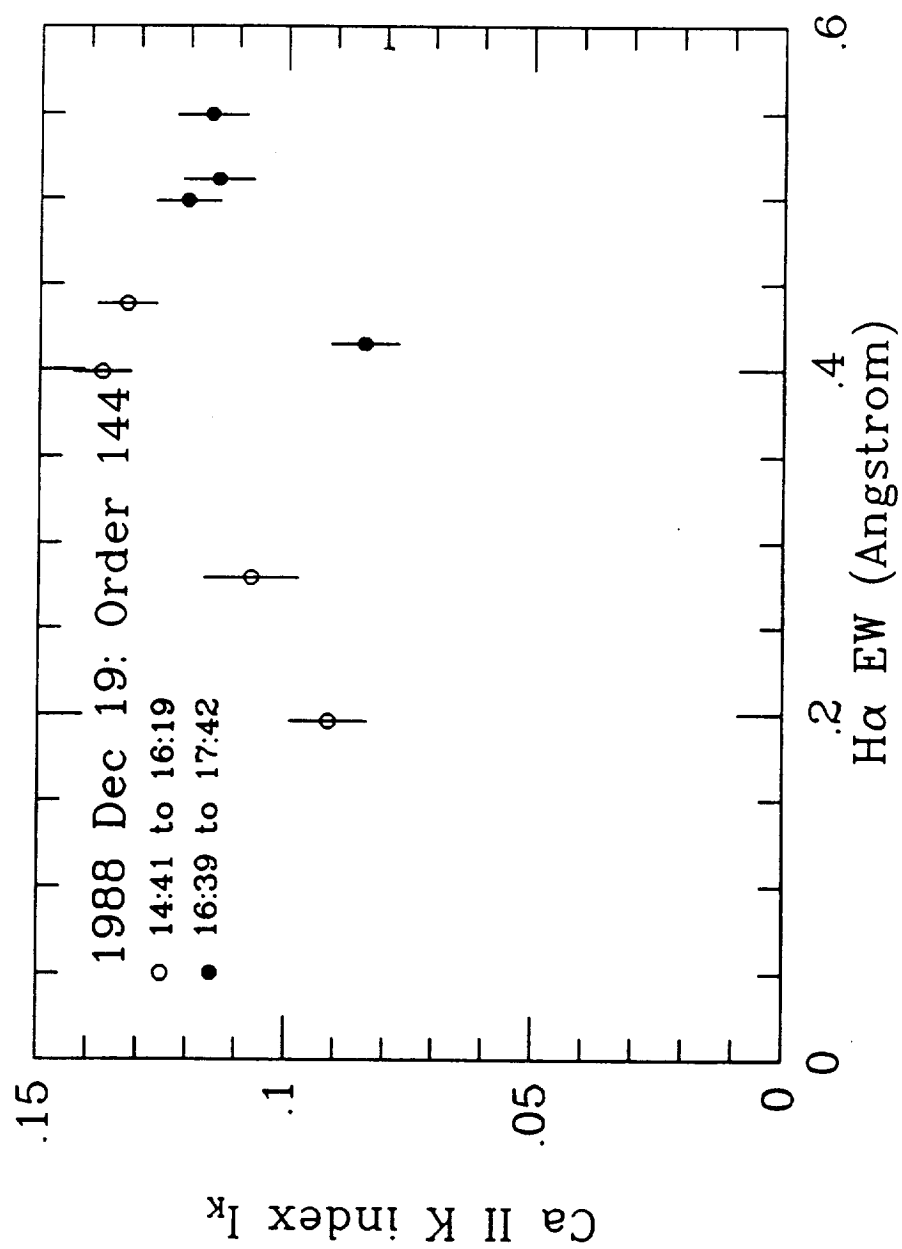


FIG. 4 (a) - PANEL 2 OF 2

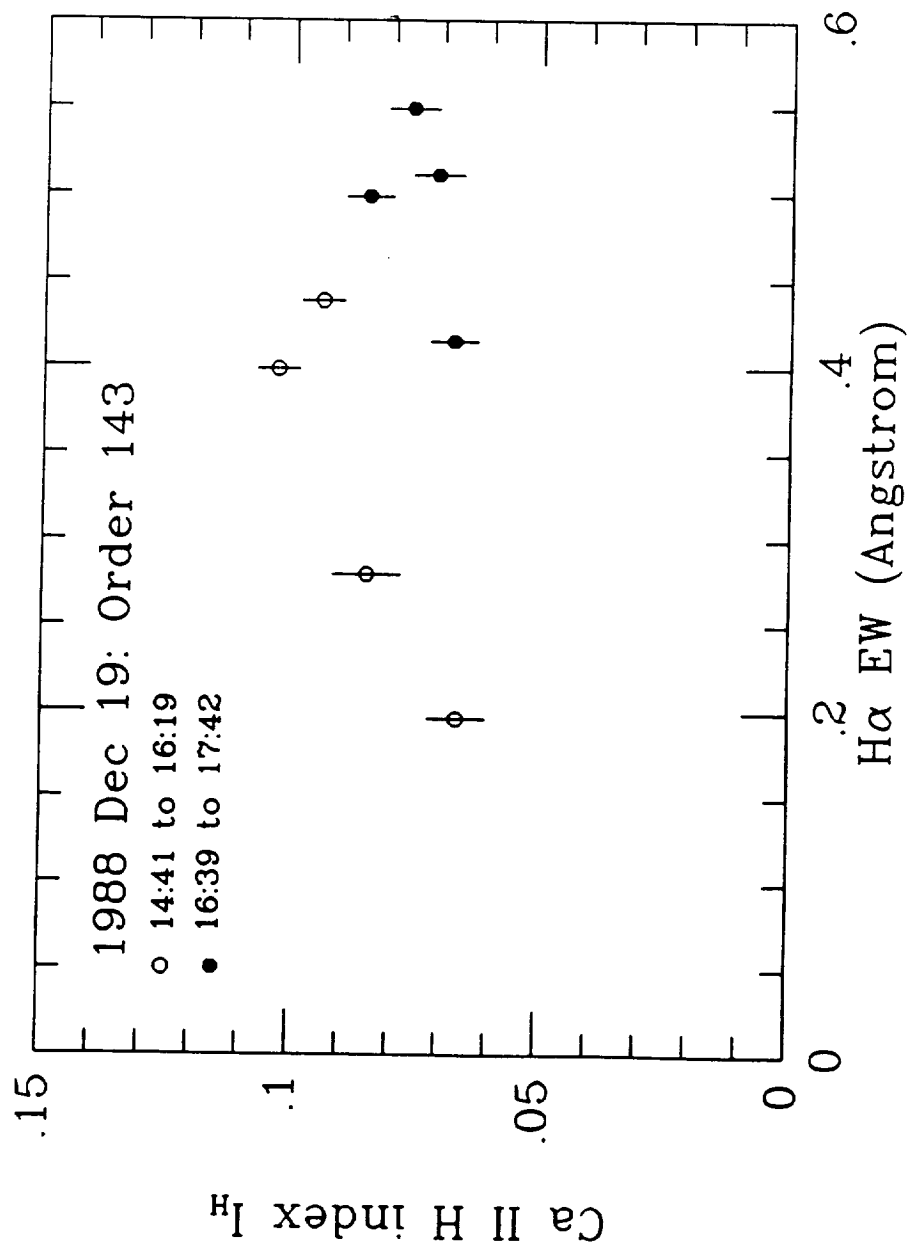


Fig 4(b) - PANEL 1 OF 3

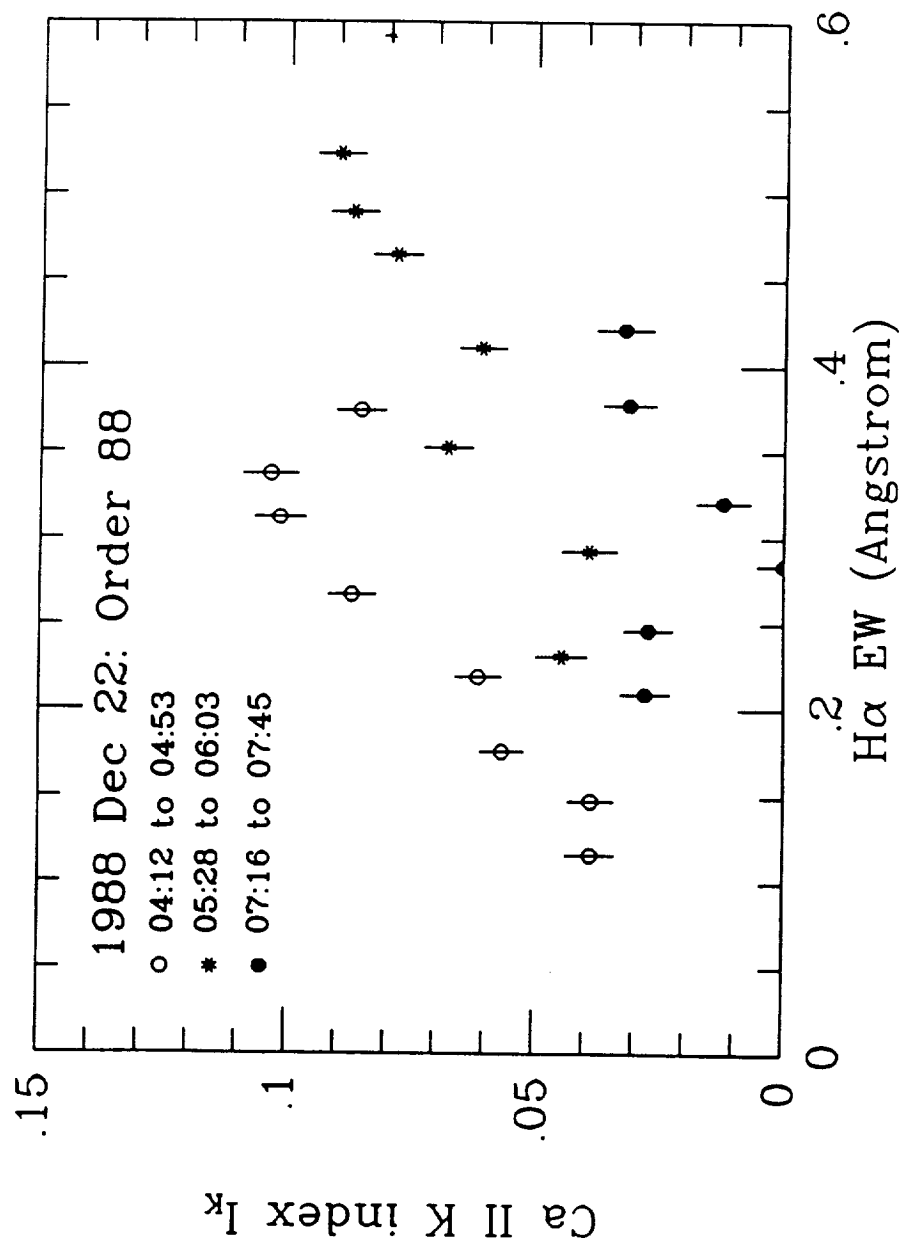


FIG. 4 (b) - PANEL 2 OF 3

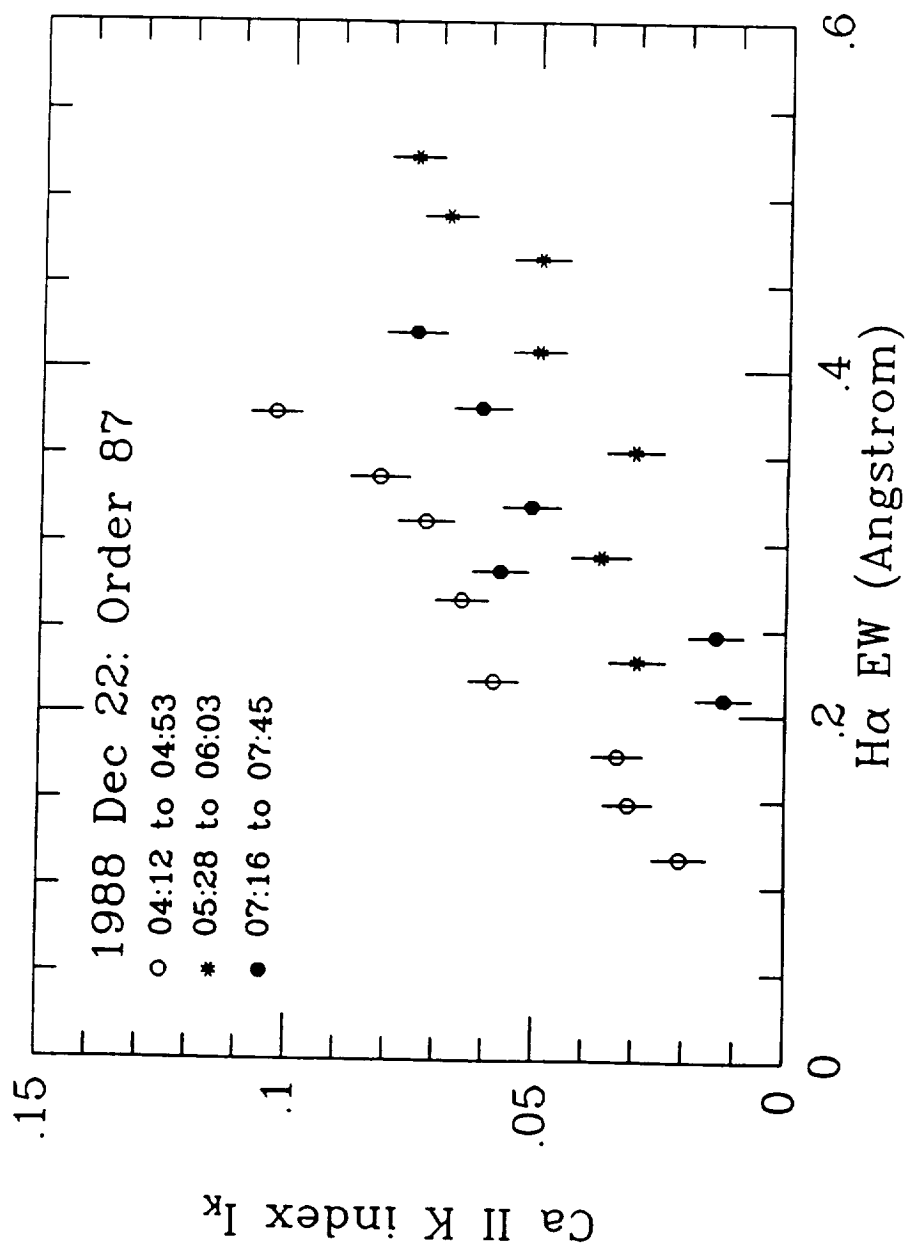


Fig. 4 (b) - PANEL 3 OF 3

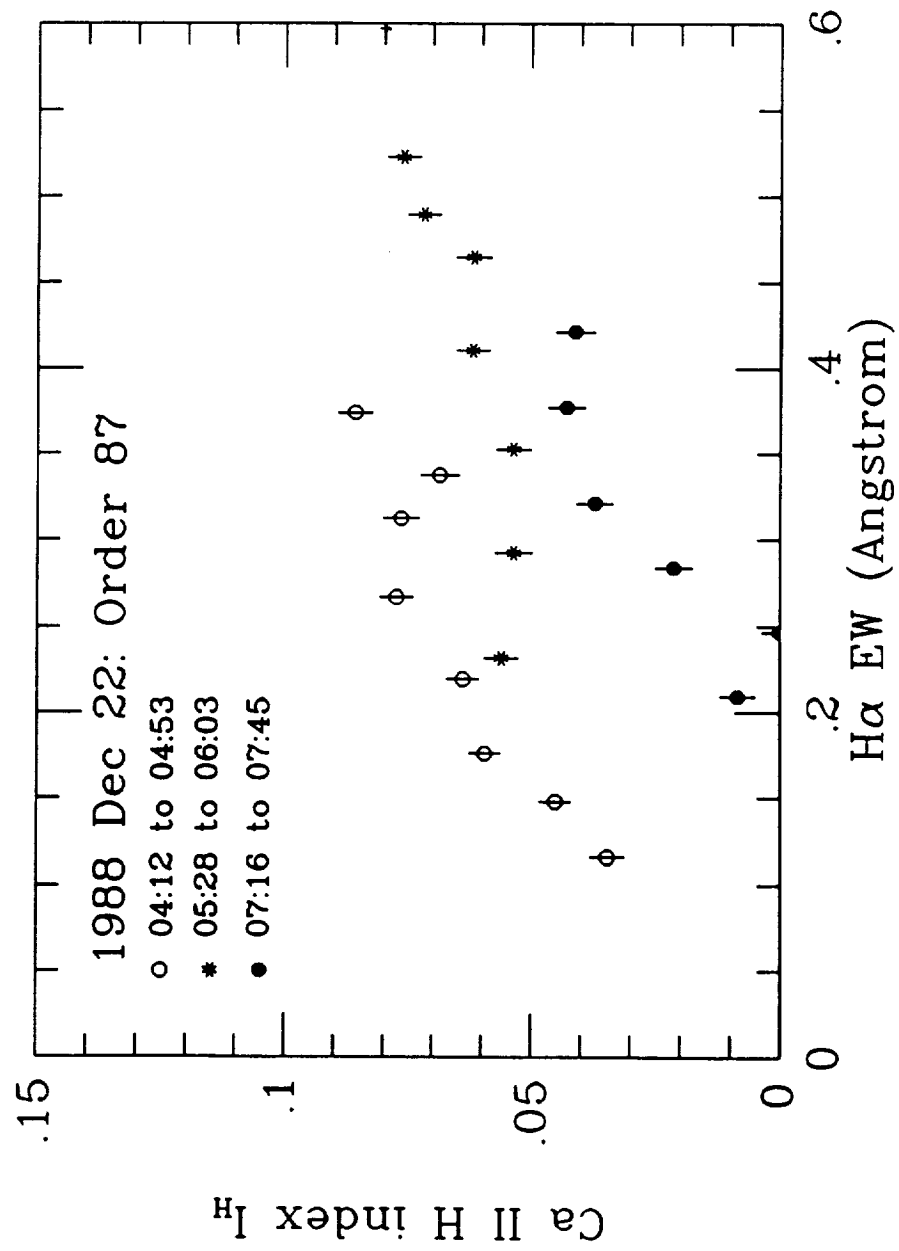


FIG. 4 (c) - PANEL 1 OF 3

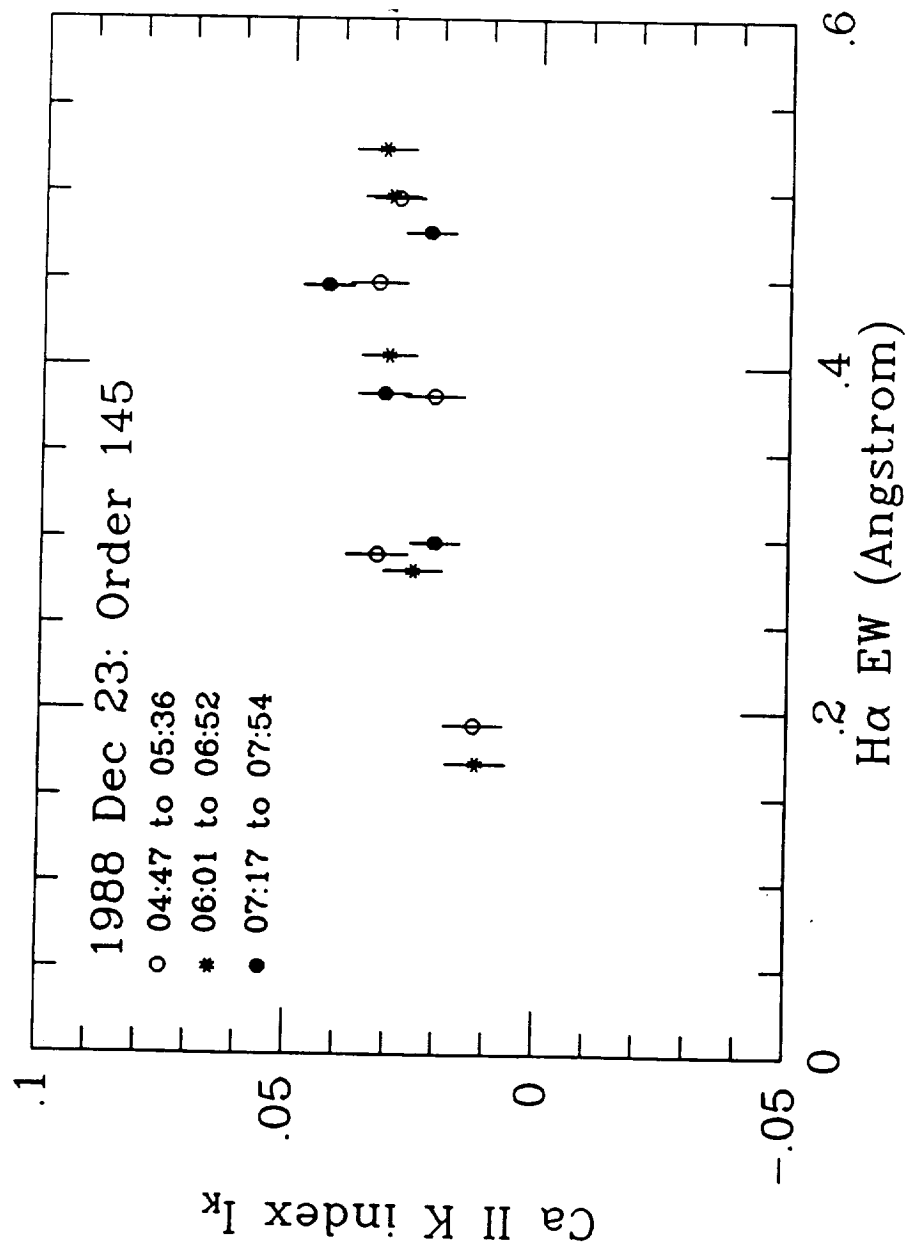


FIG 4 (c) - PANEL 2 OF 3

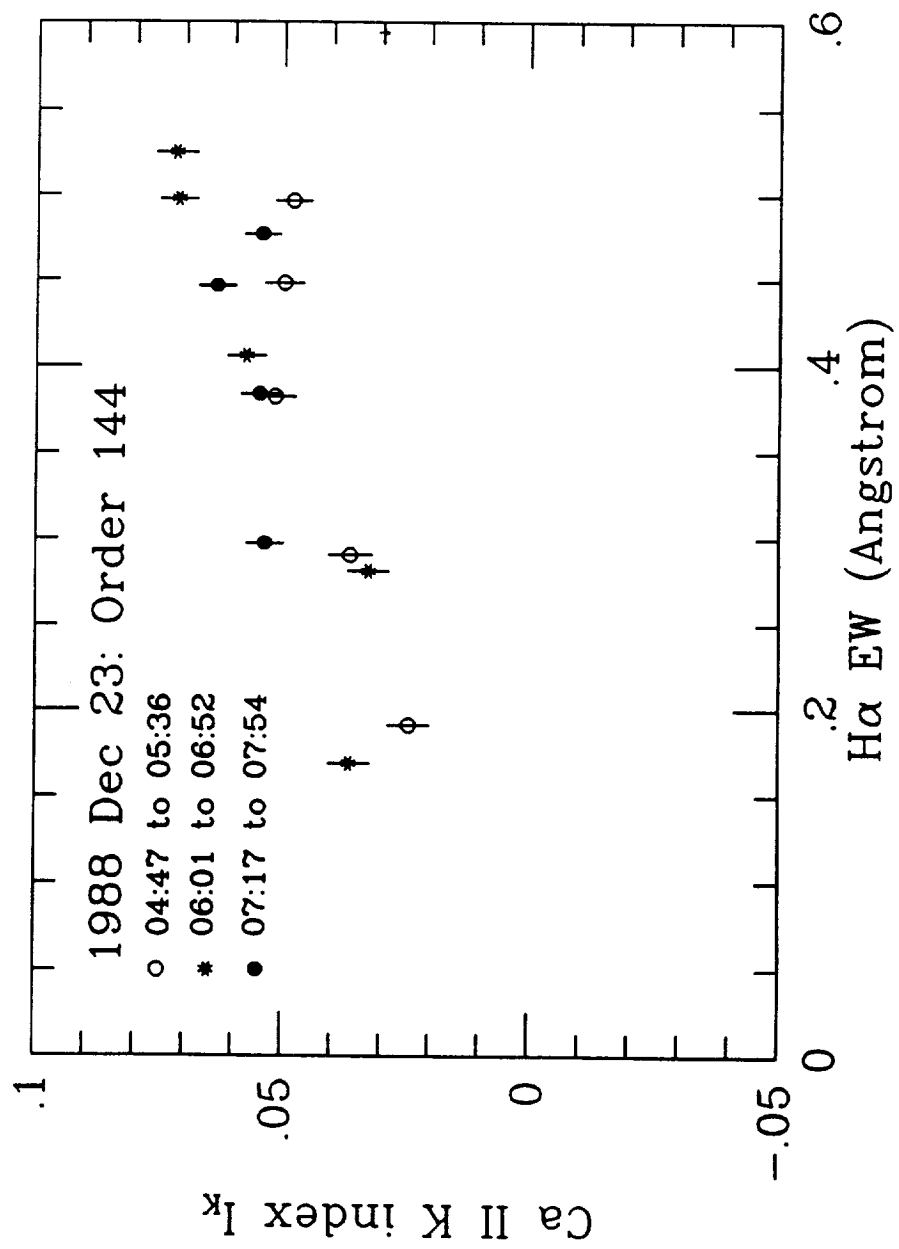


FIG. 4(d) — PANEL 3 OF 3

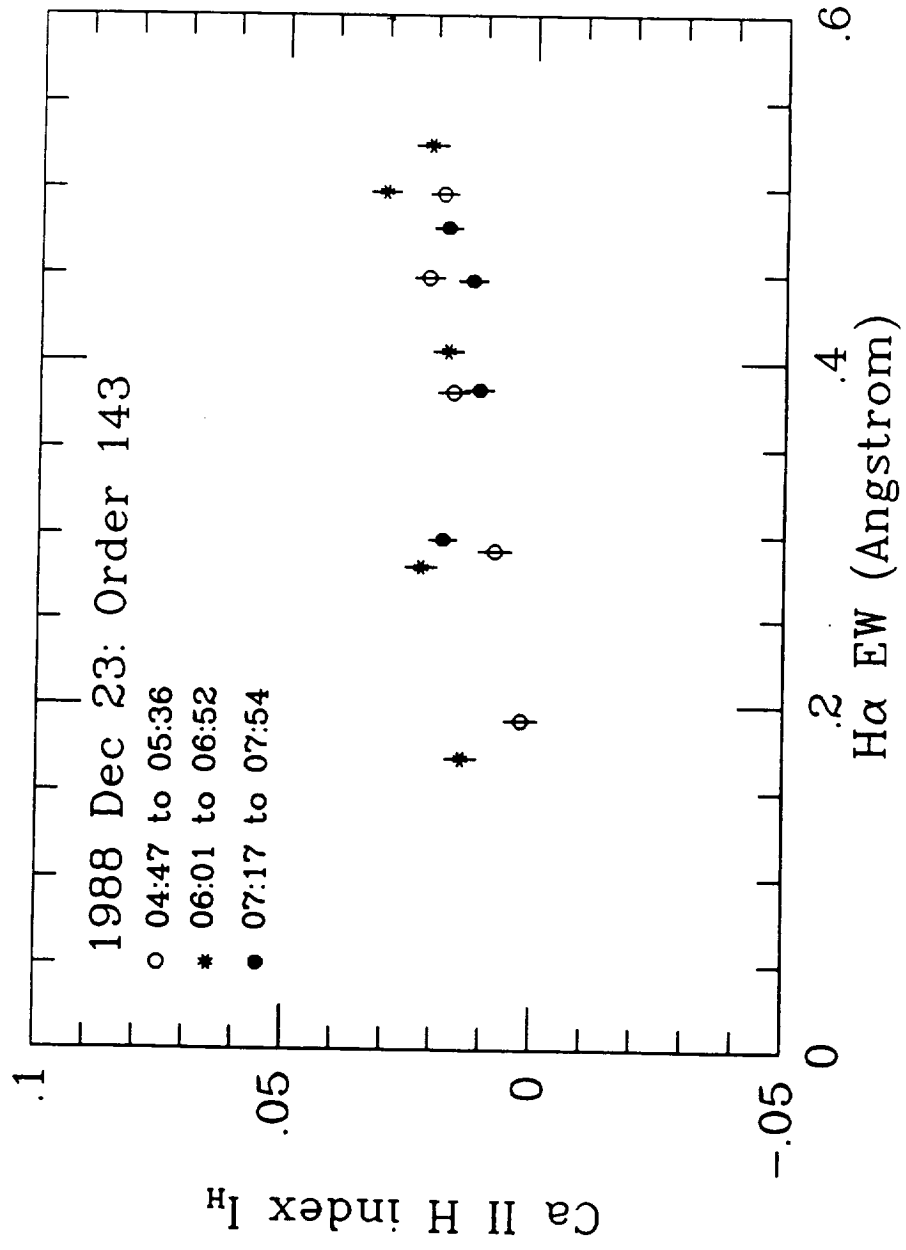


FIG. 5 — PANEL 1 OF 2

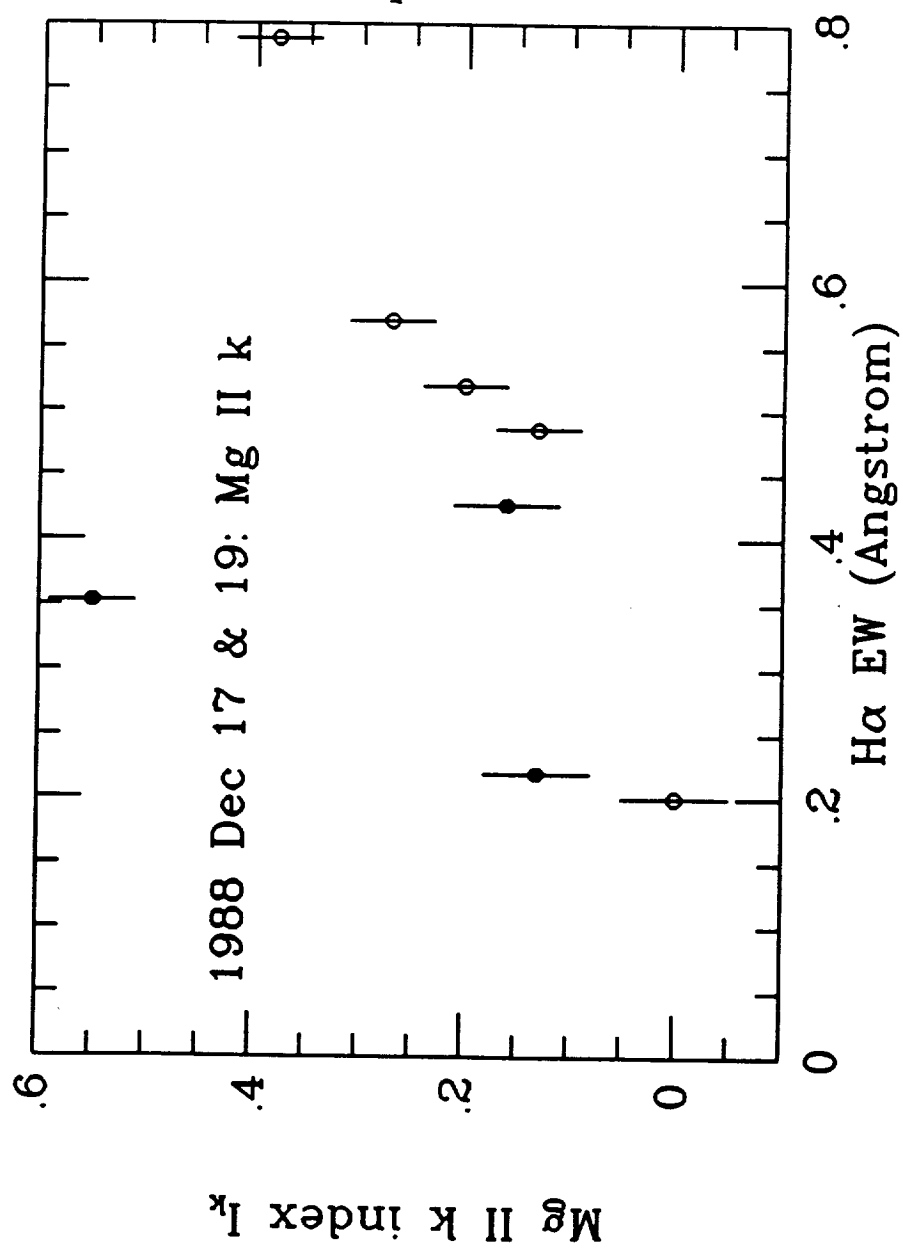
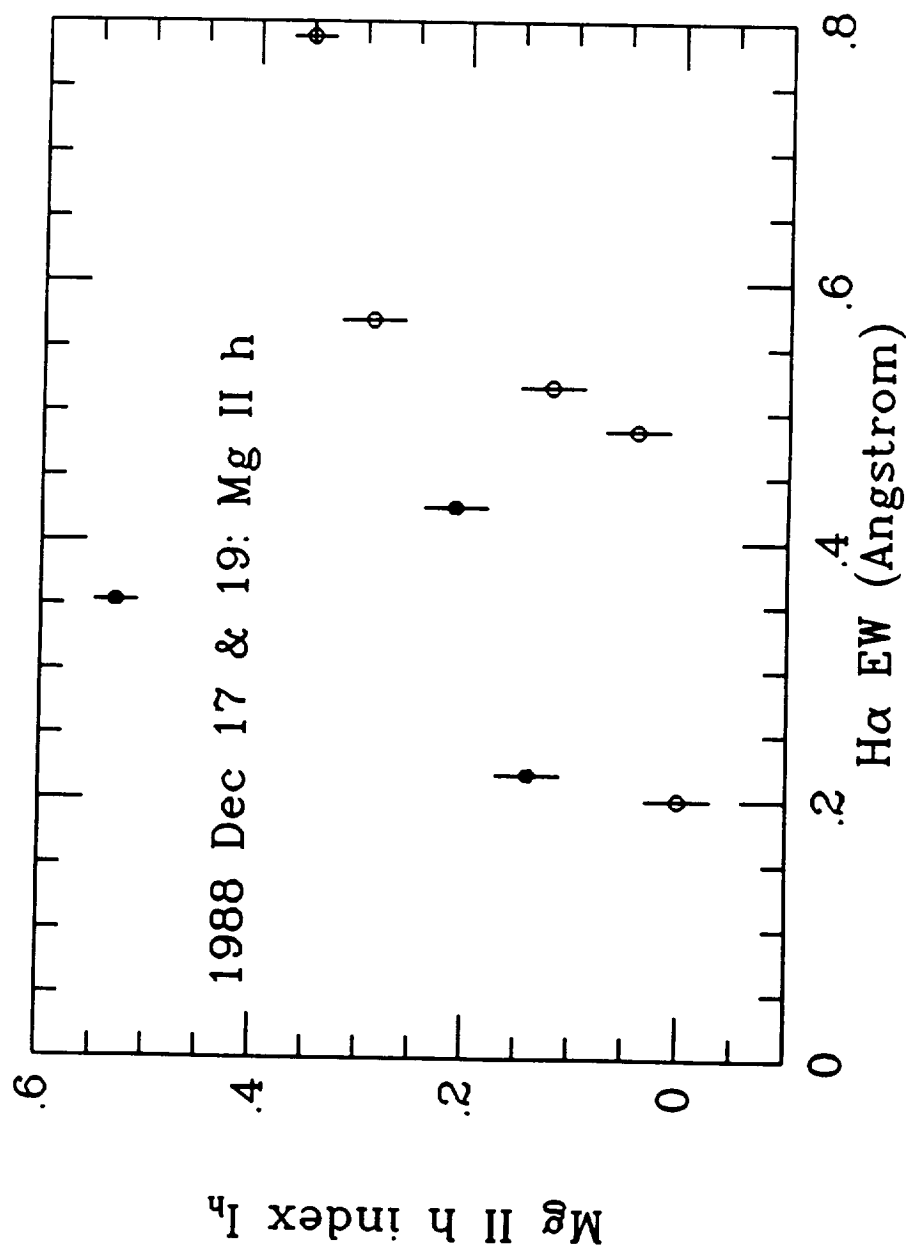
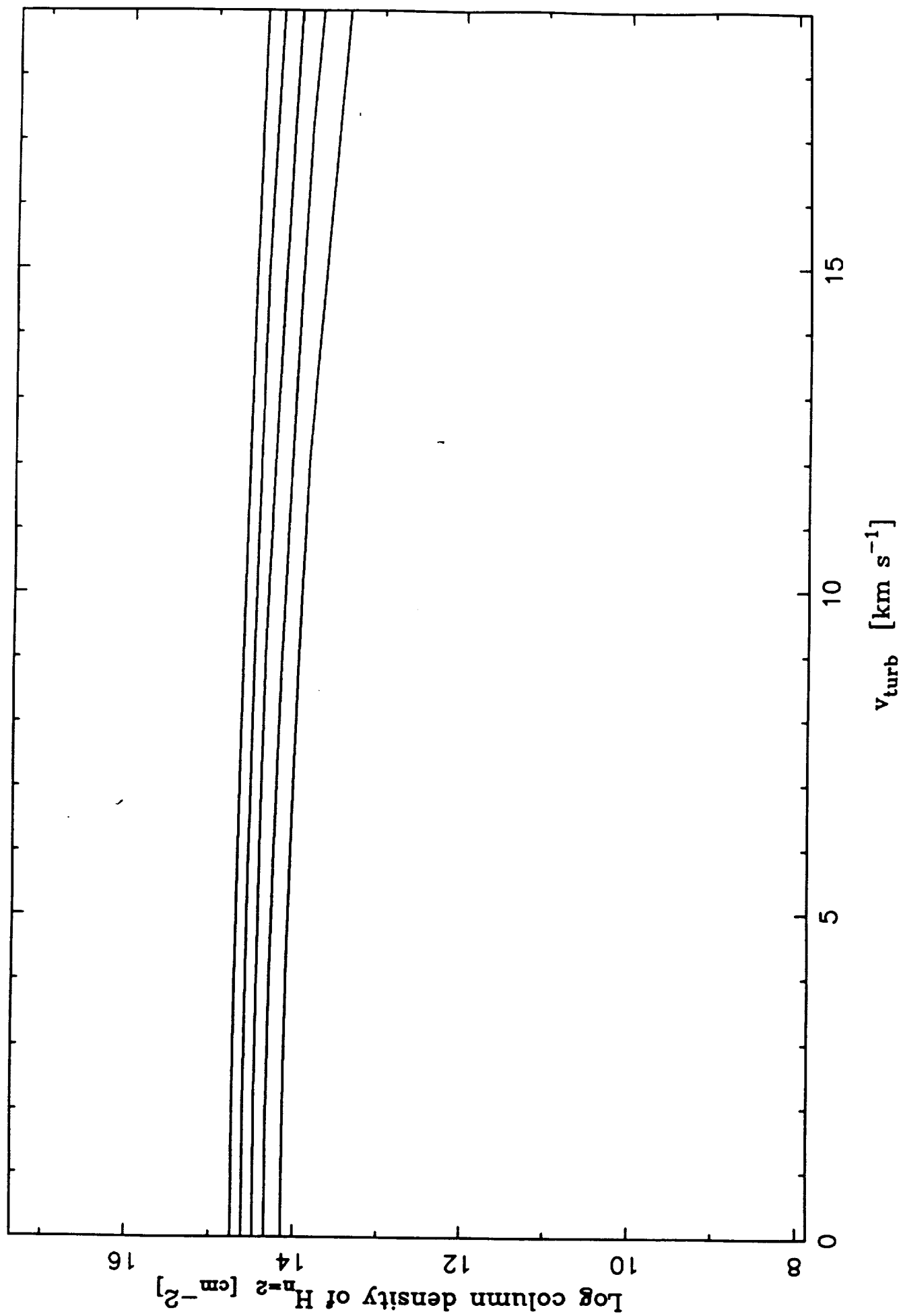
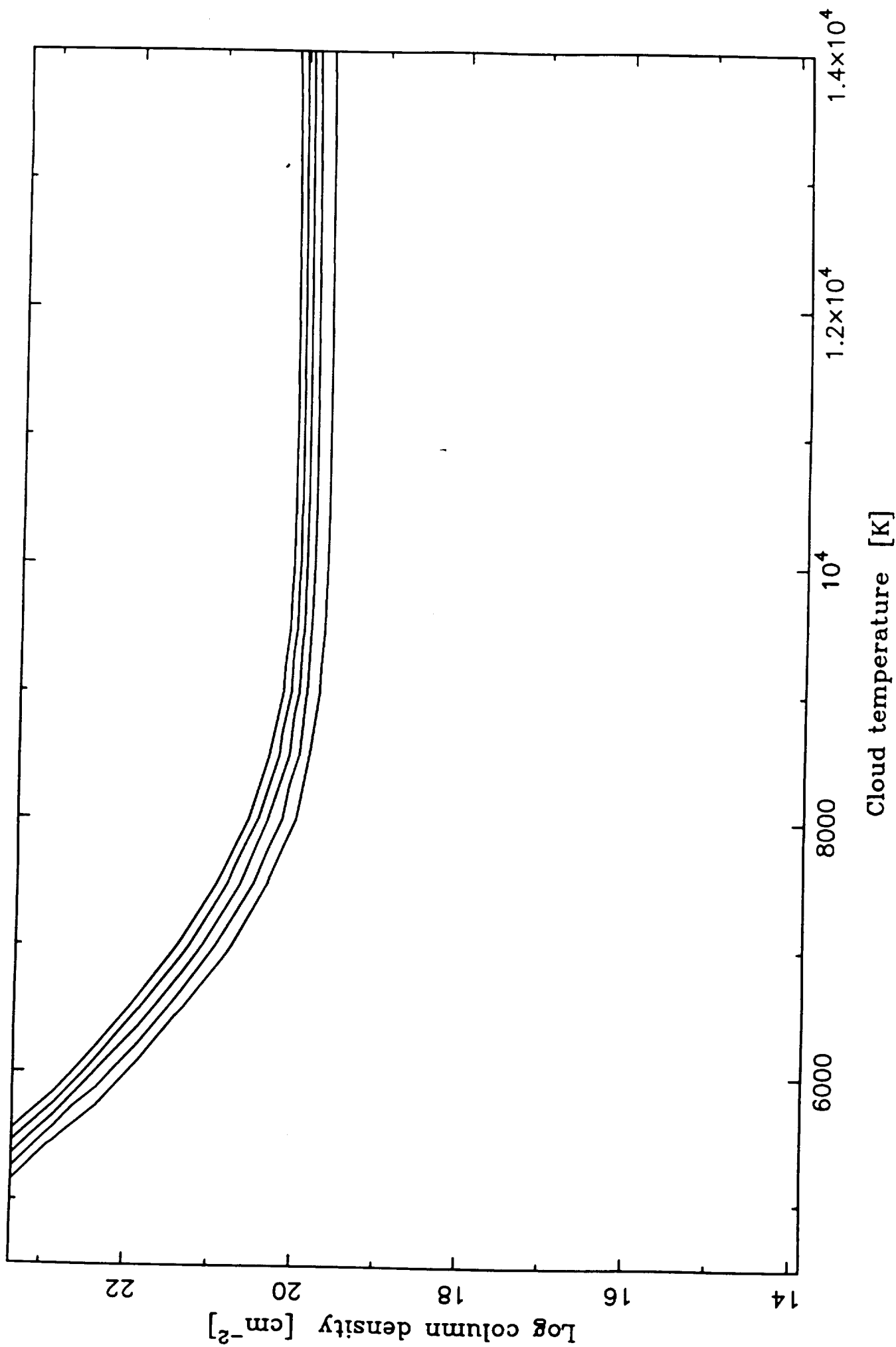


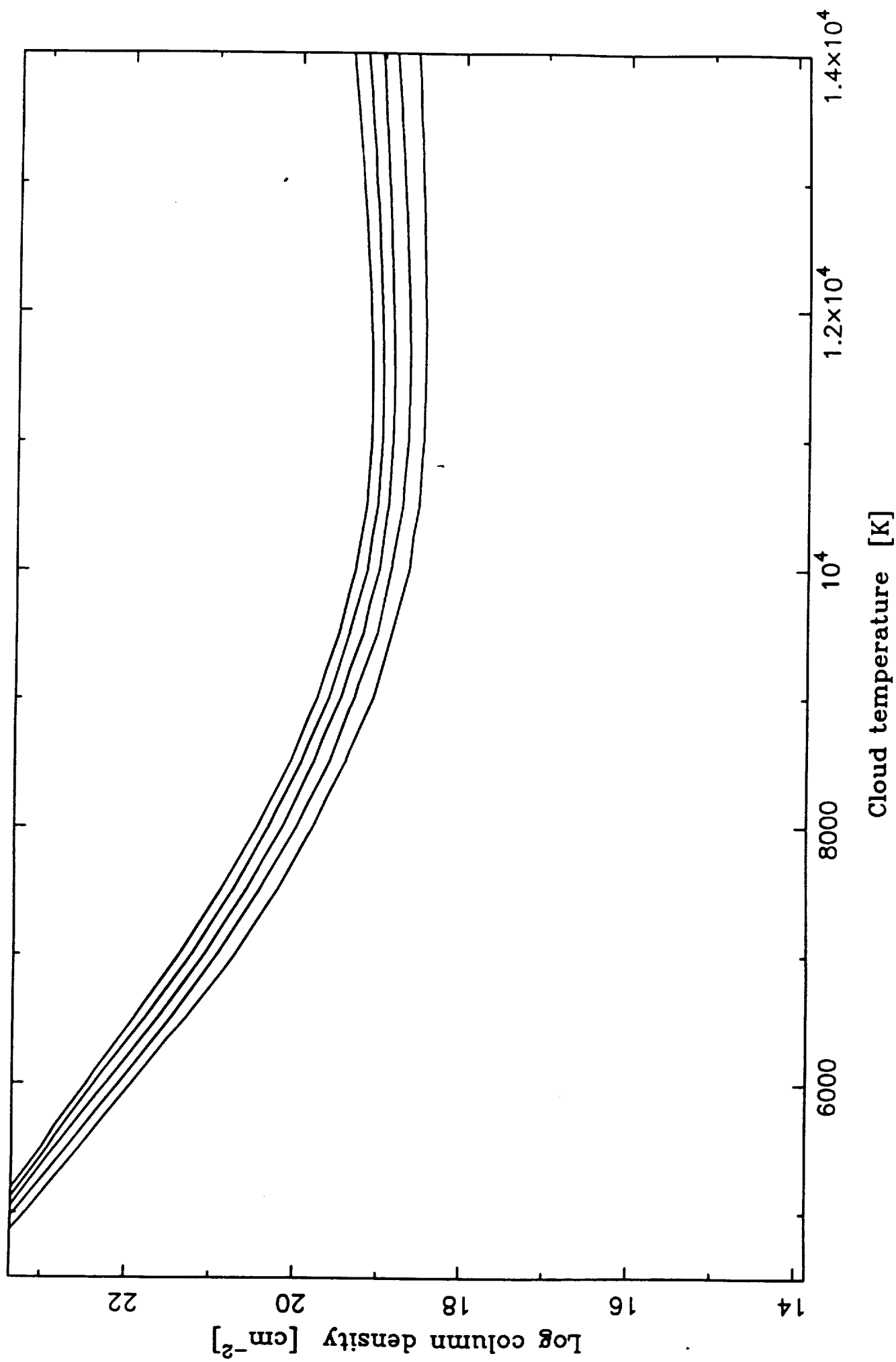
Fig. 5 — Panel 2 of 2



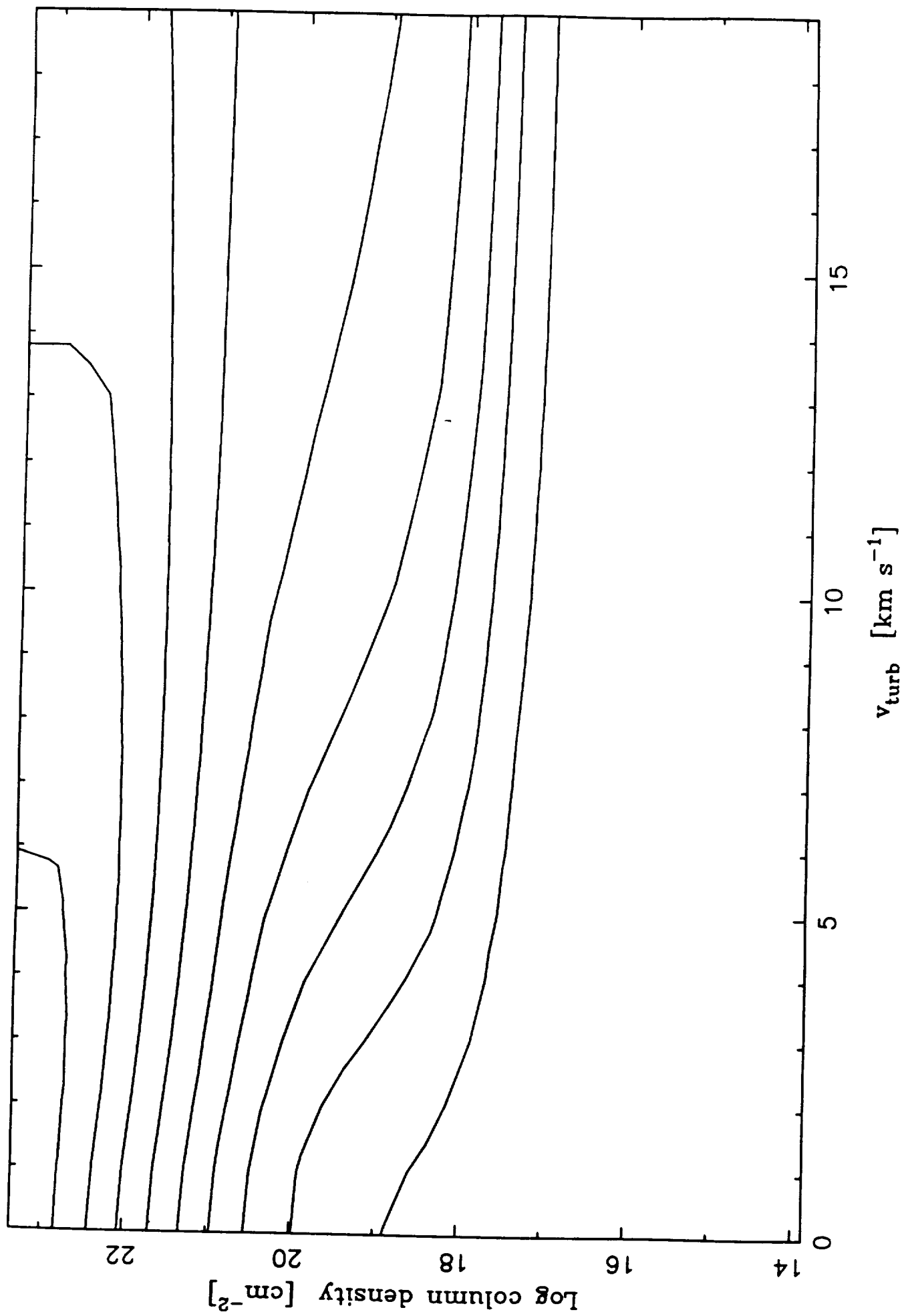
Contours of constant H α EW: uniform model

Contours of constant H α EW: uniform structure



Contours of constant $H\alpha$ EW: fragmented structure

Contours of constant Ca II K index i_K



Contours of constant Ca II H index i_H

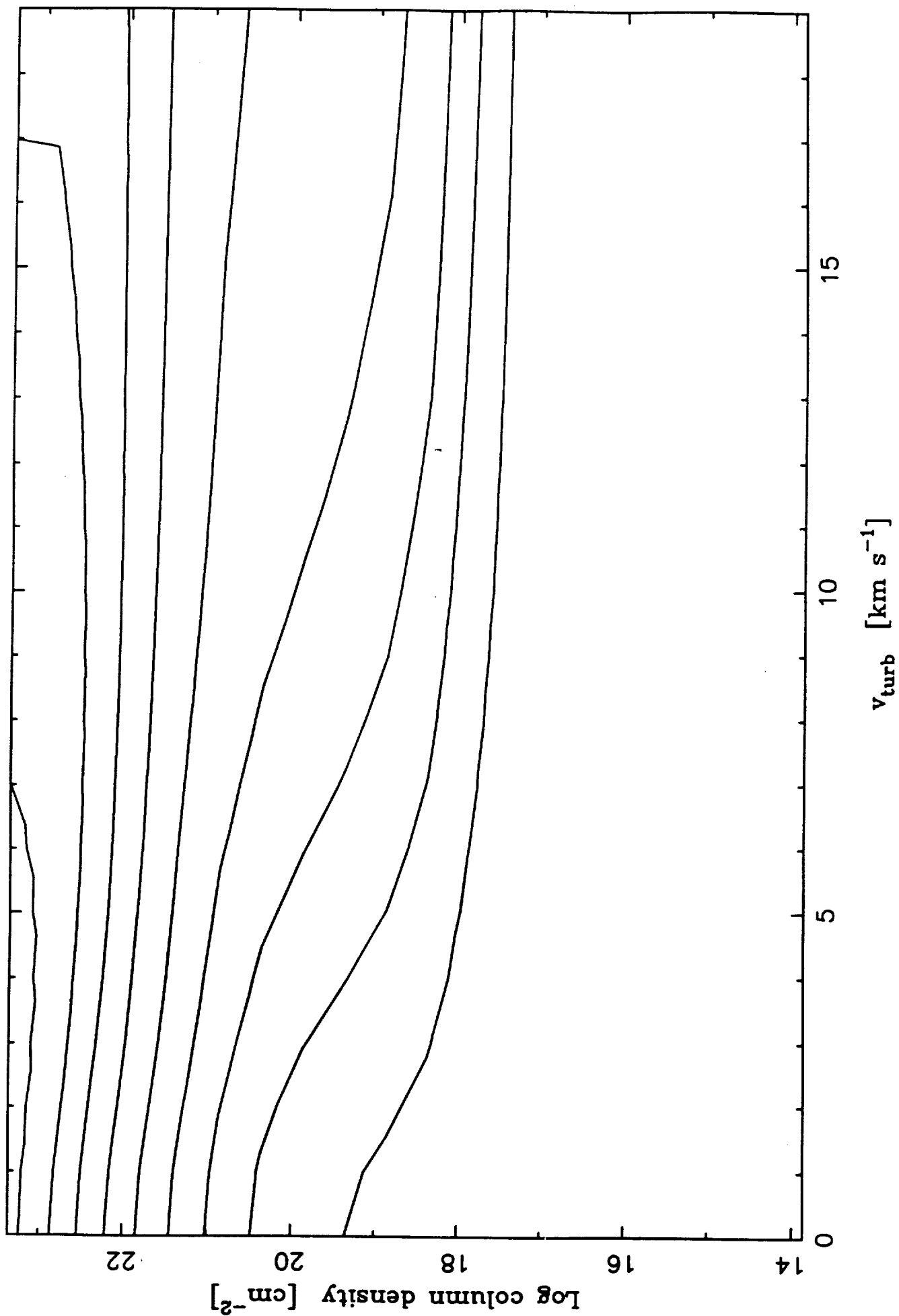


Fig. 10 (a)

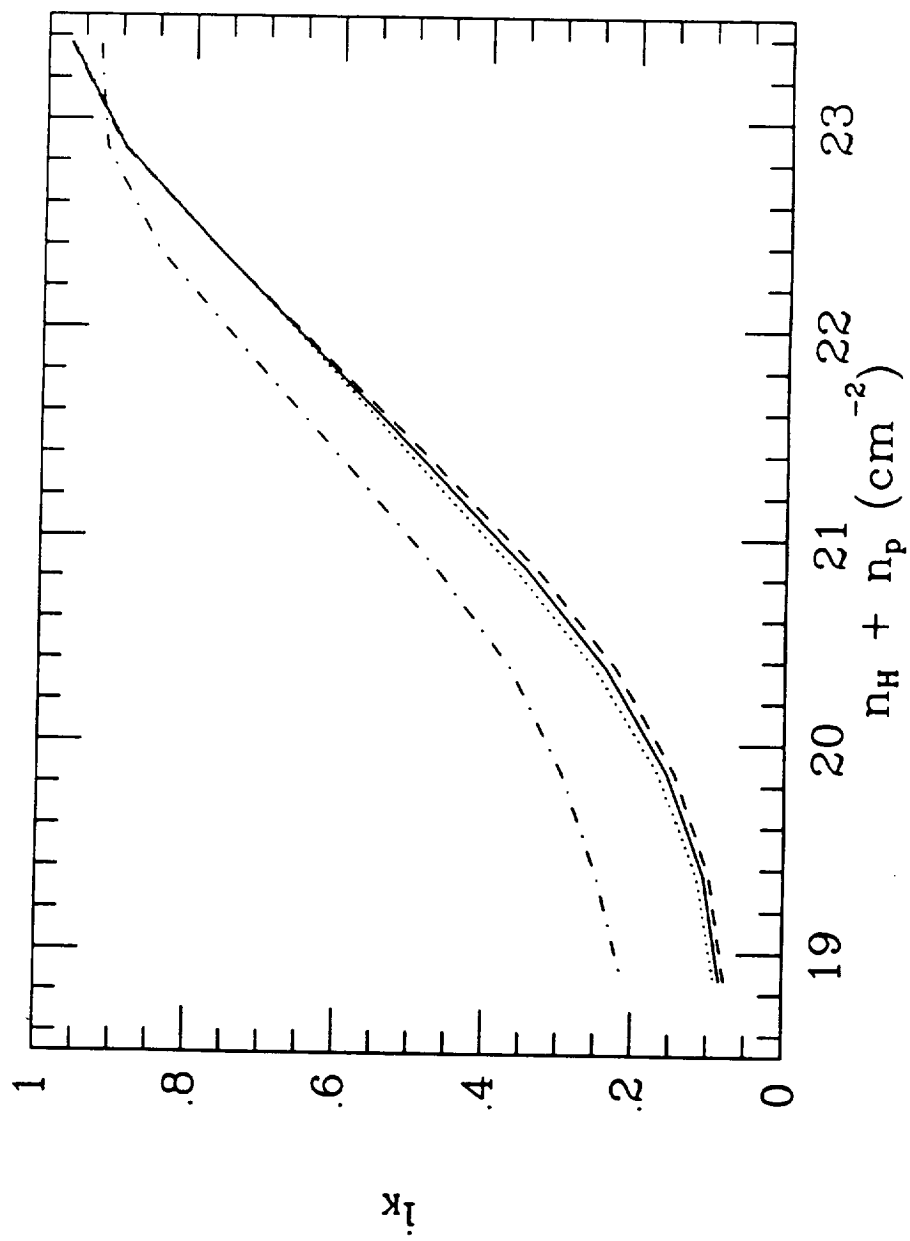
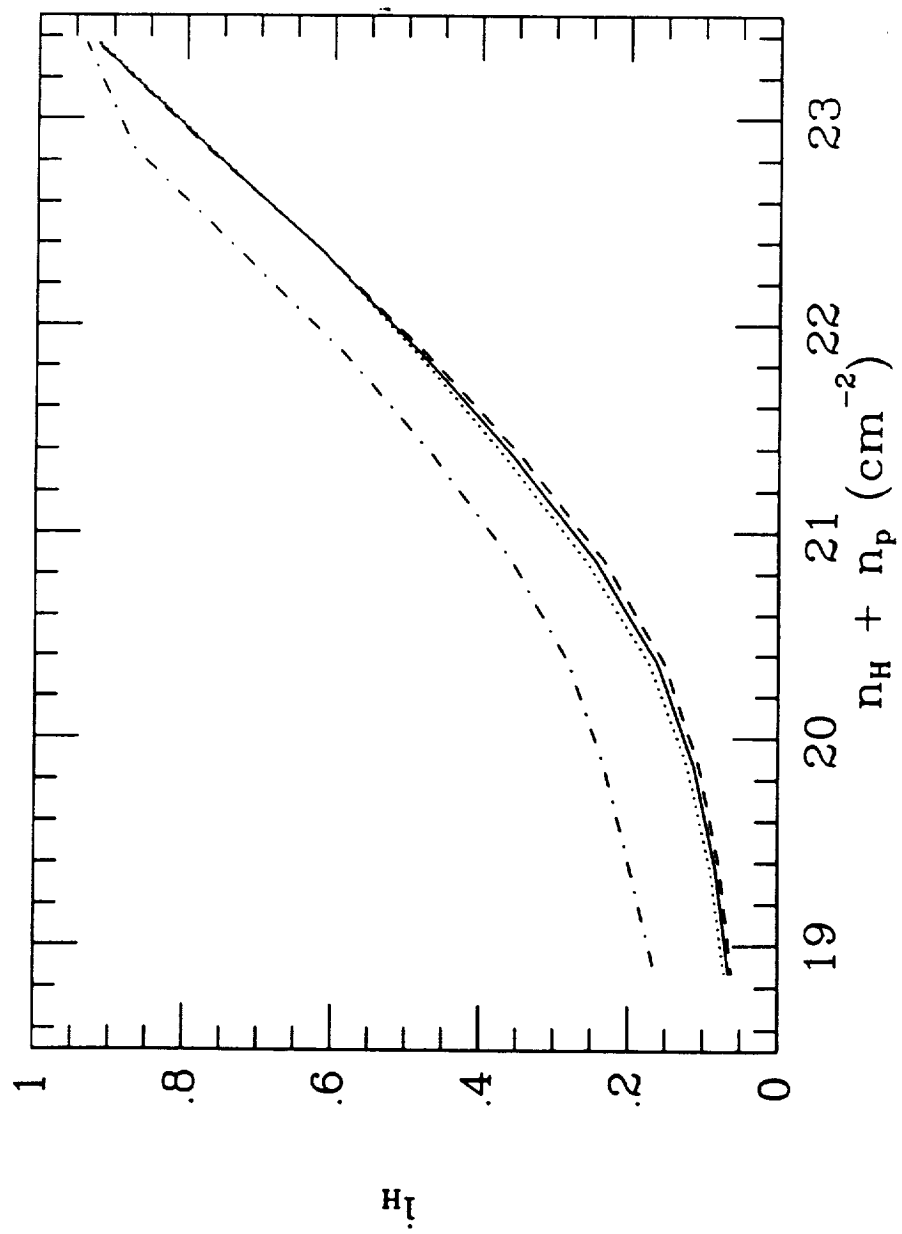
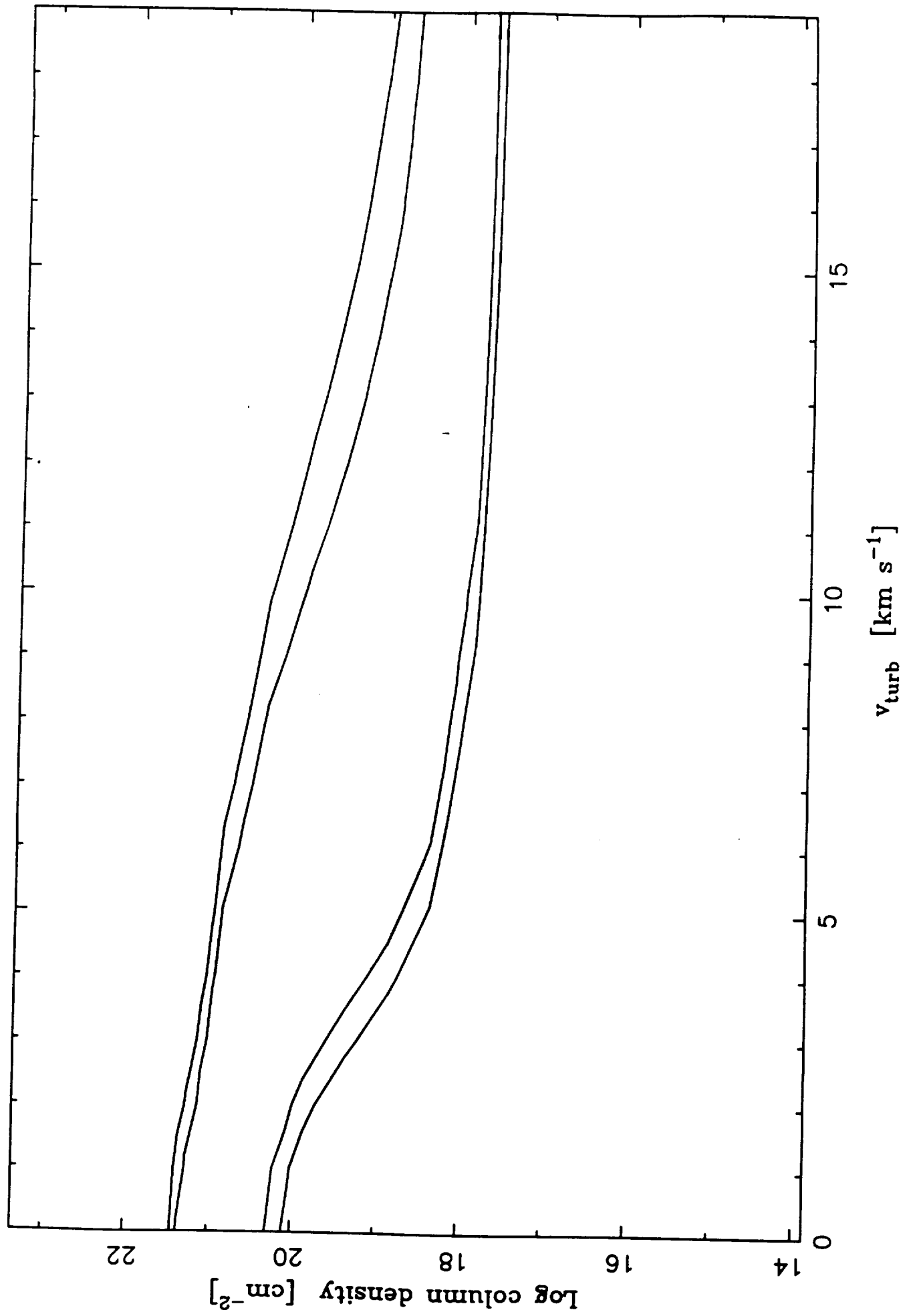


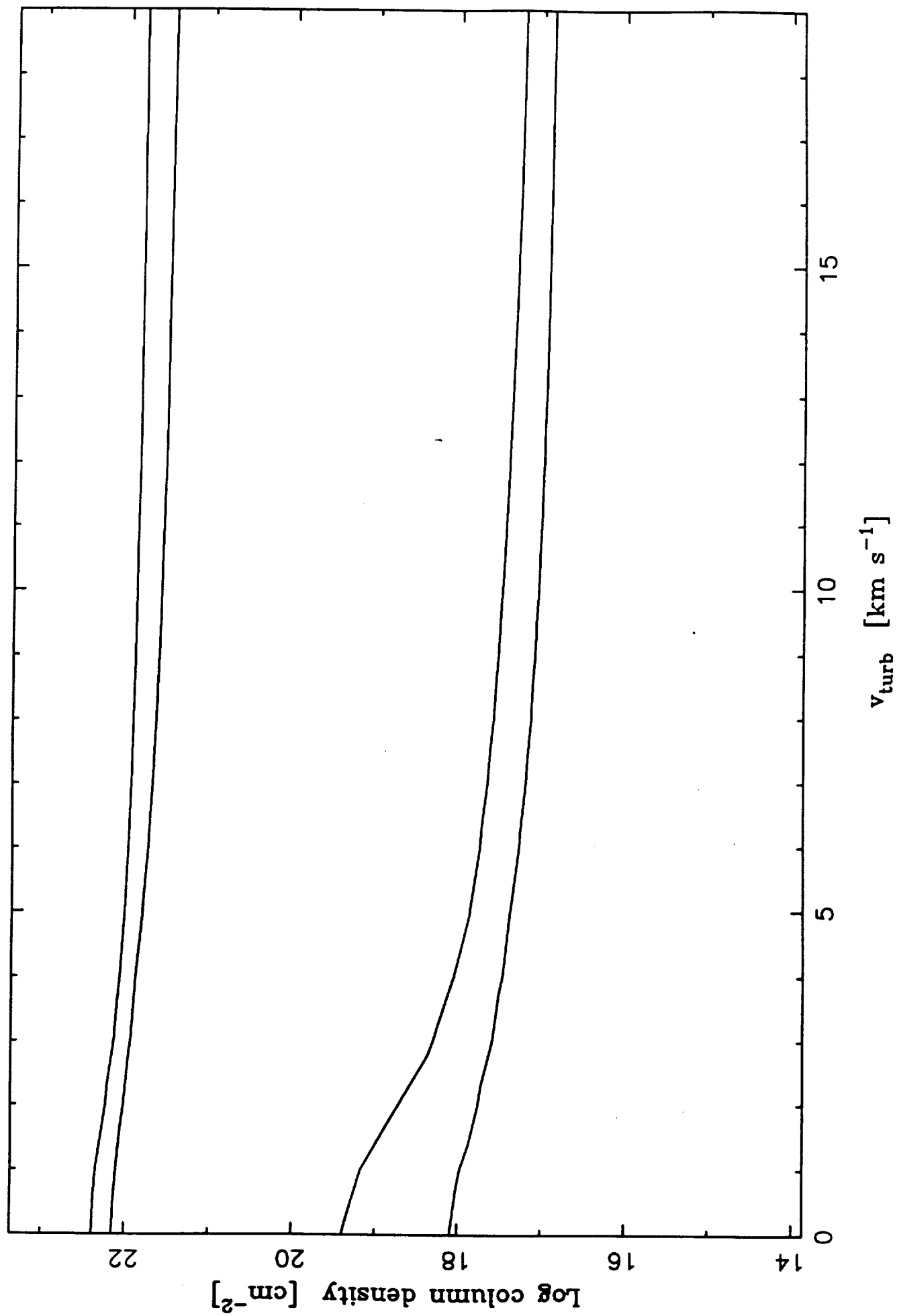
Fig 10 (b)



Confidence limits for 1988 Dec 19 14:41 to 16:19



Confidence limits for 1988 Dec 19 16:39 to 17:42



Confidence limits for 1988 Dec 22 04:12 to 04:53

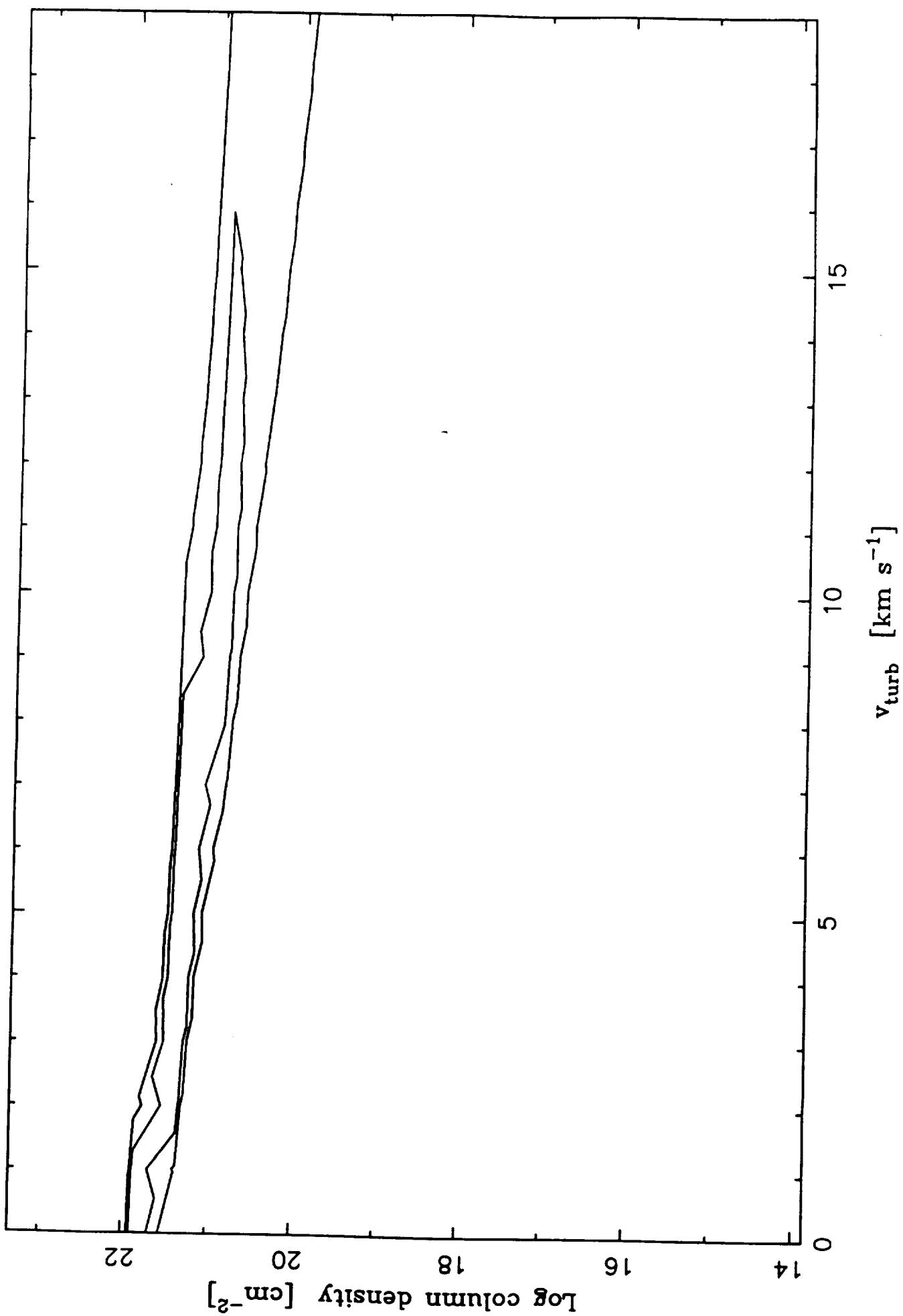
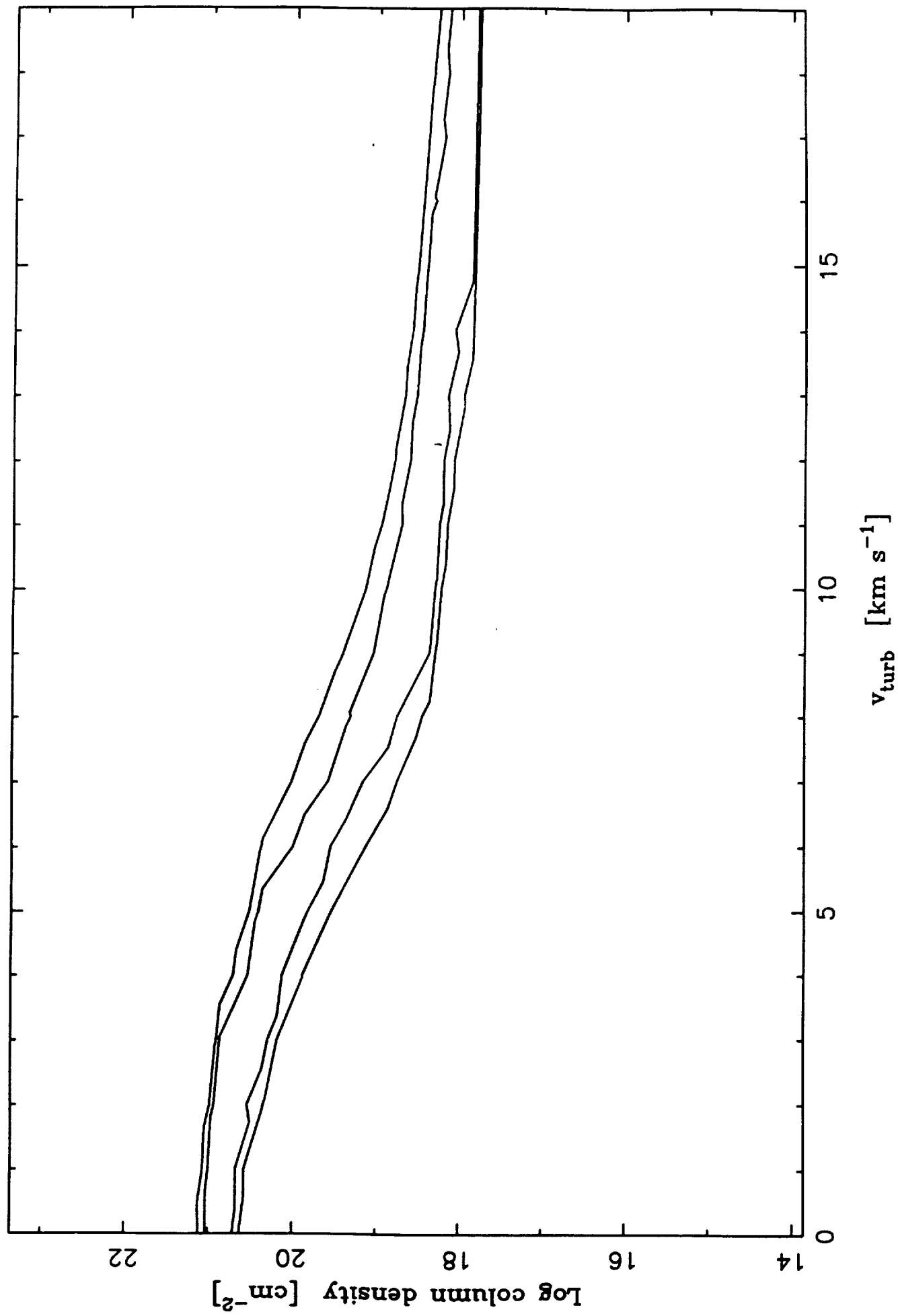
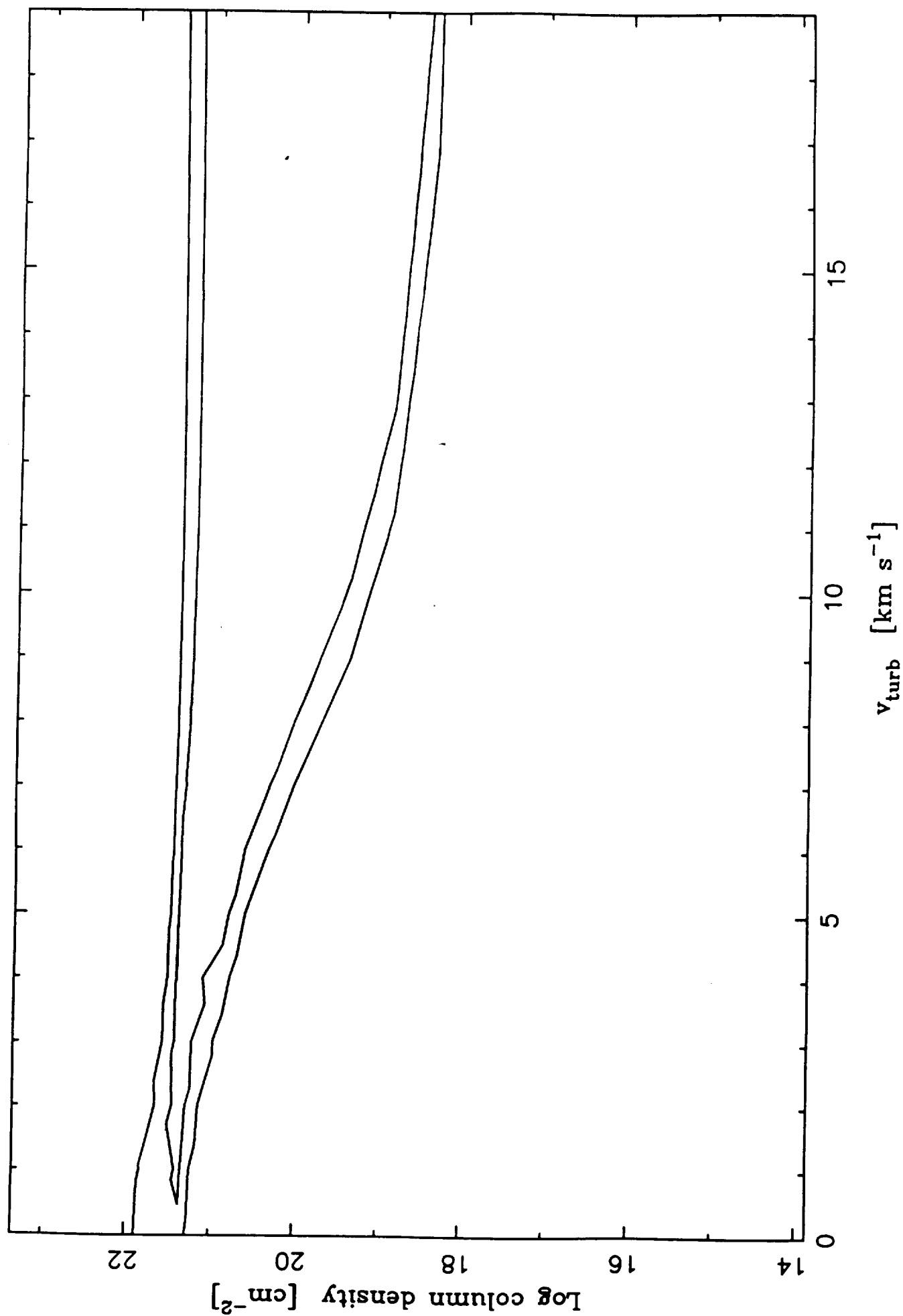


Fig. 11 (d)

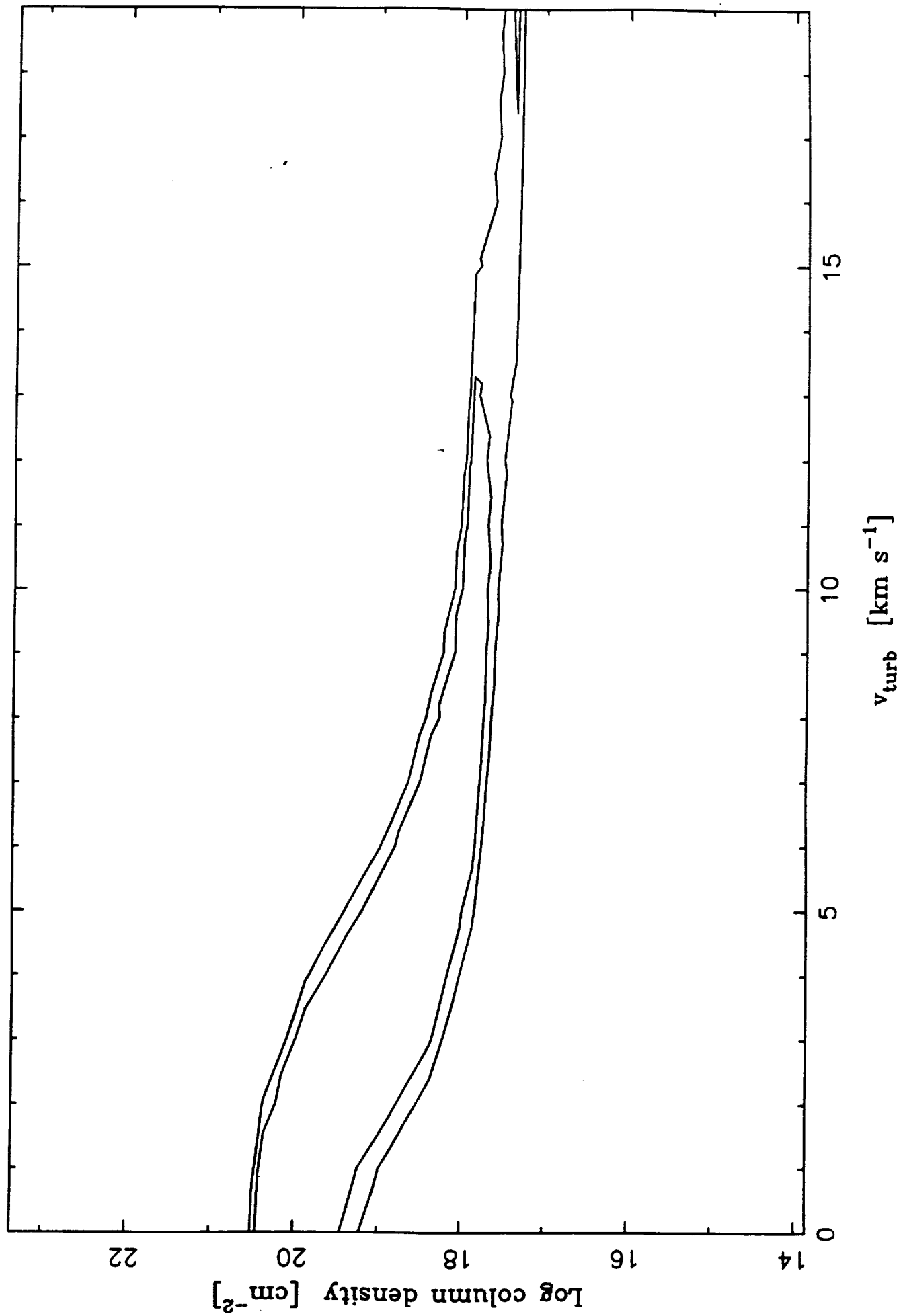
Confidence limits for 1988 Dec 22 05:28 to 06:03



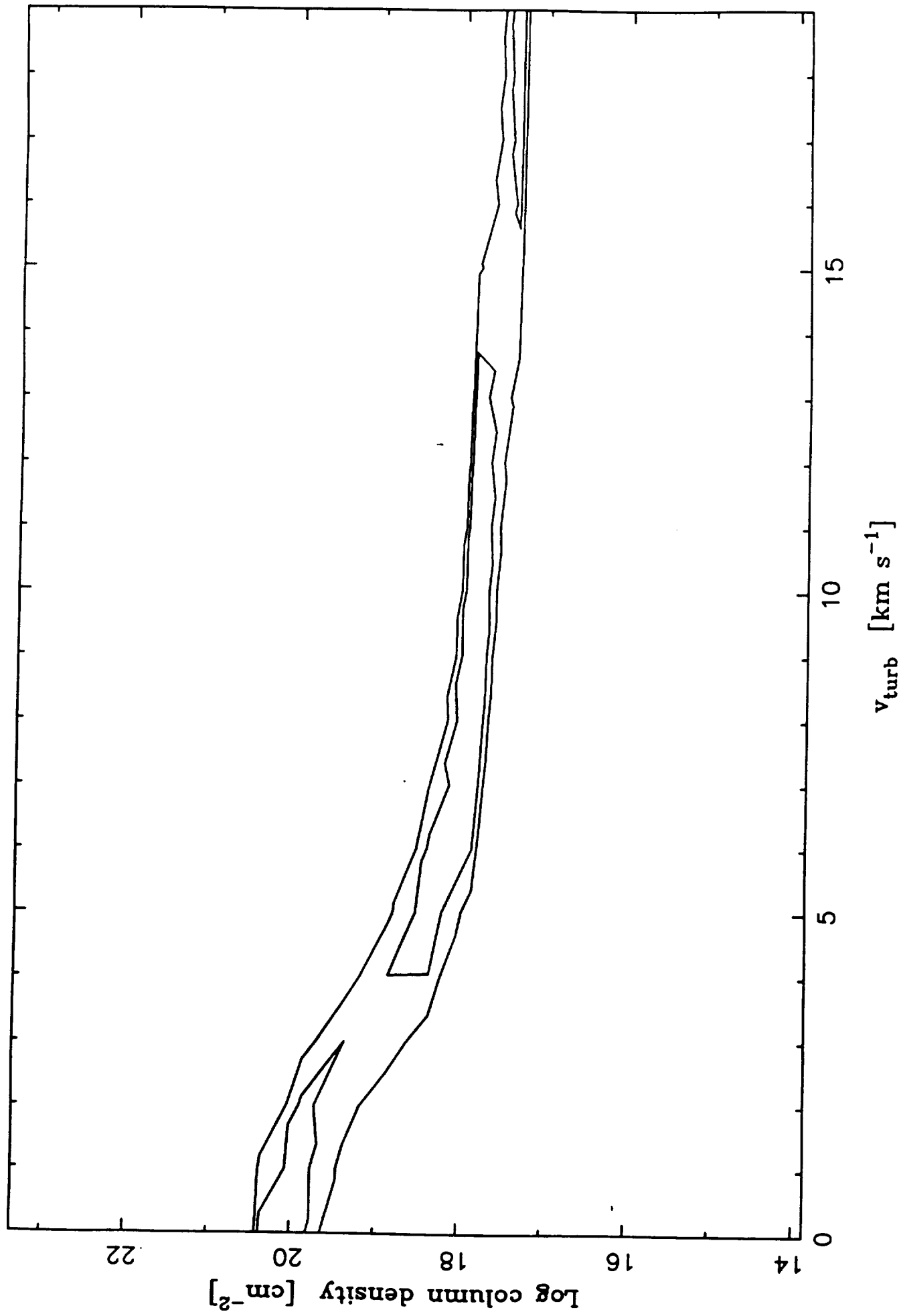
Confidence limits for 1988 Dec 22 07:16 to 07:45



Confidence limits for 1988 Dec 23 04:47 to 05:36

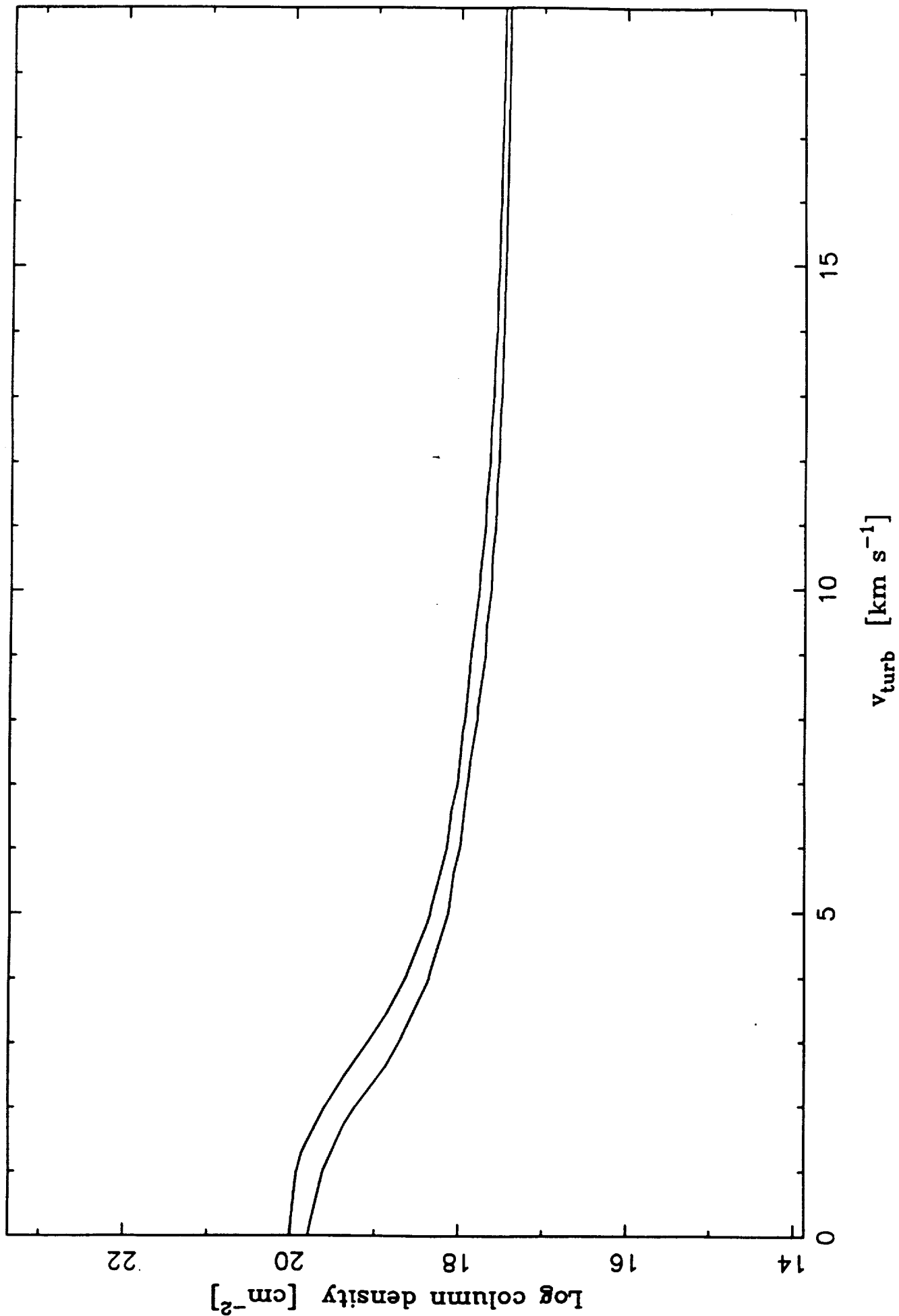


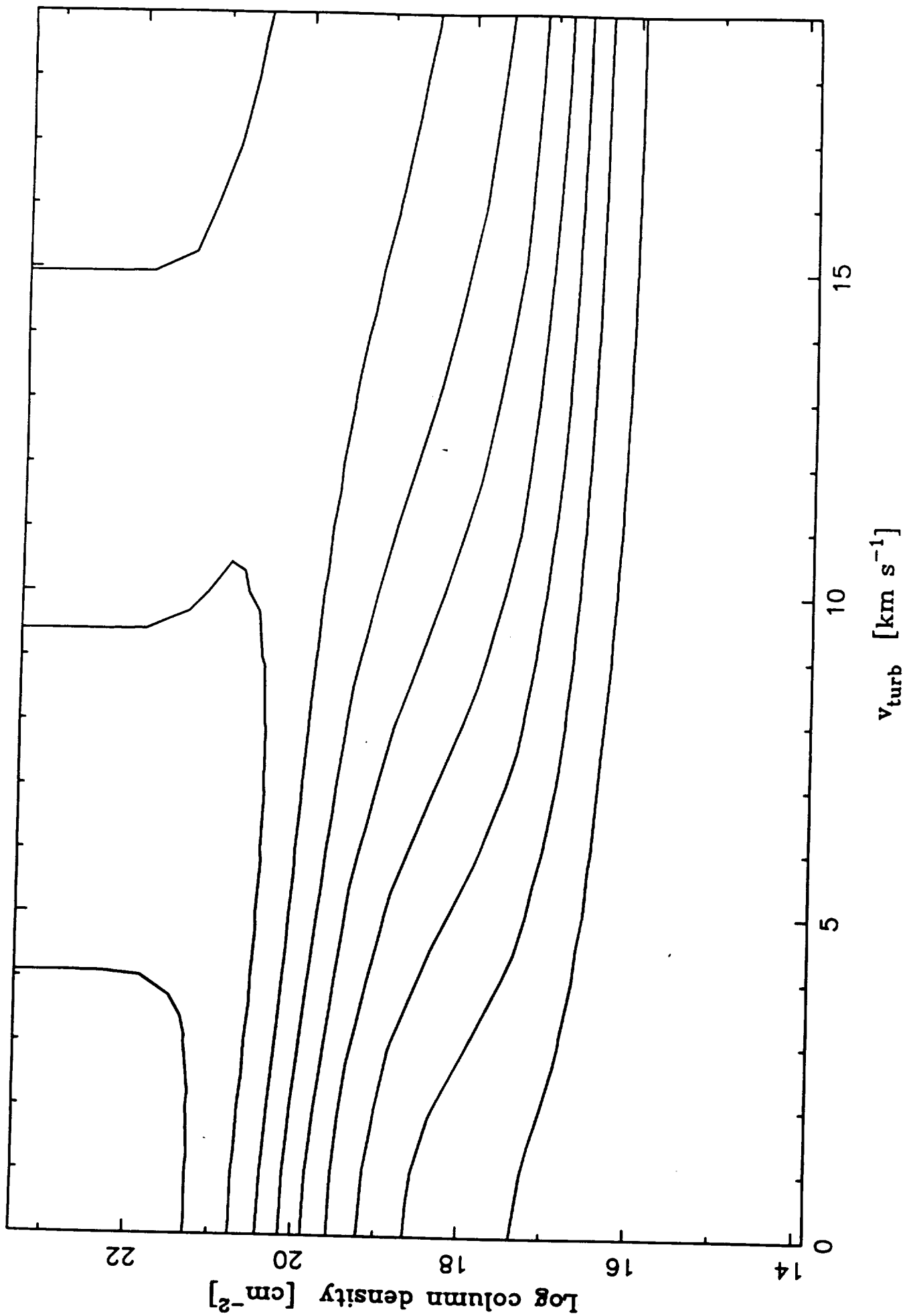
Confidence limits for 1988 Dec 23 06:01 to 06:52



$\hat{f}(v_{\text{turb}}, v)$

Confidence limits for 1988 Dec 23 07:17 to 07:54





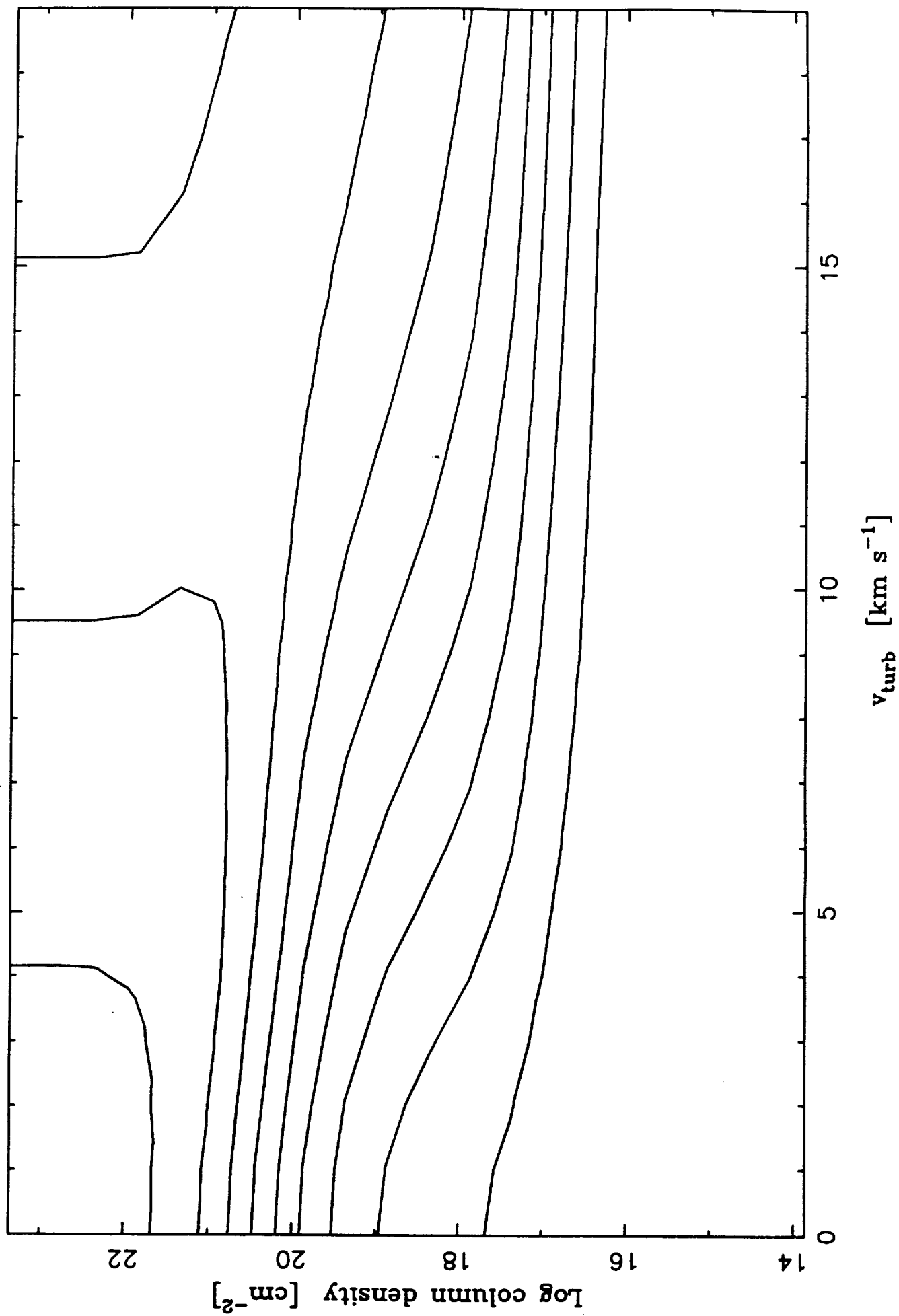
Contours of constant Mg II h index i_h 

Fig. 13 (a)

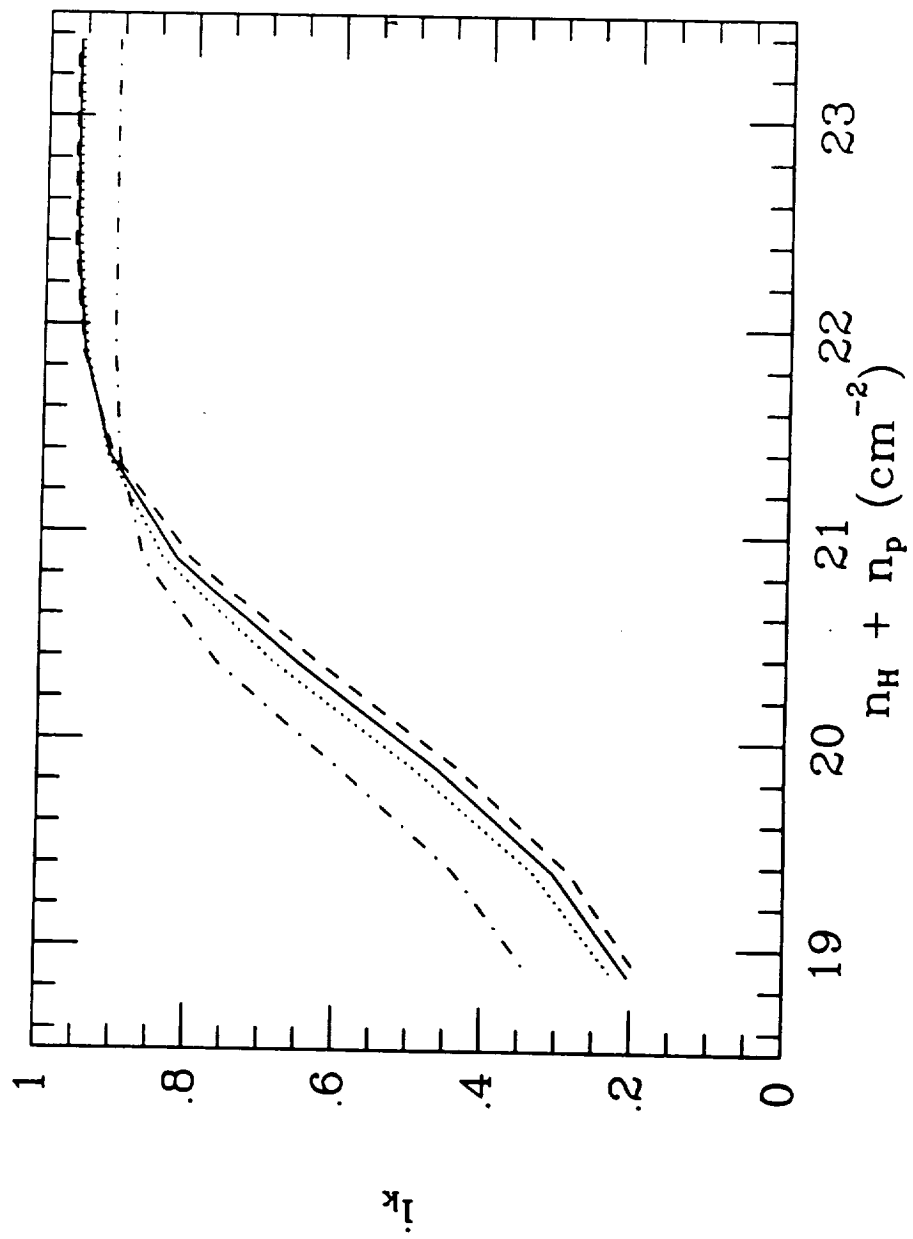
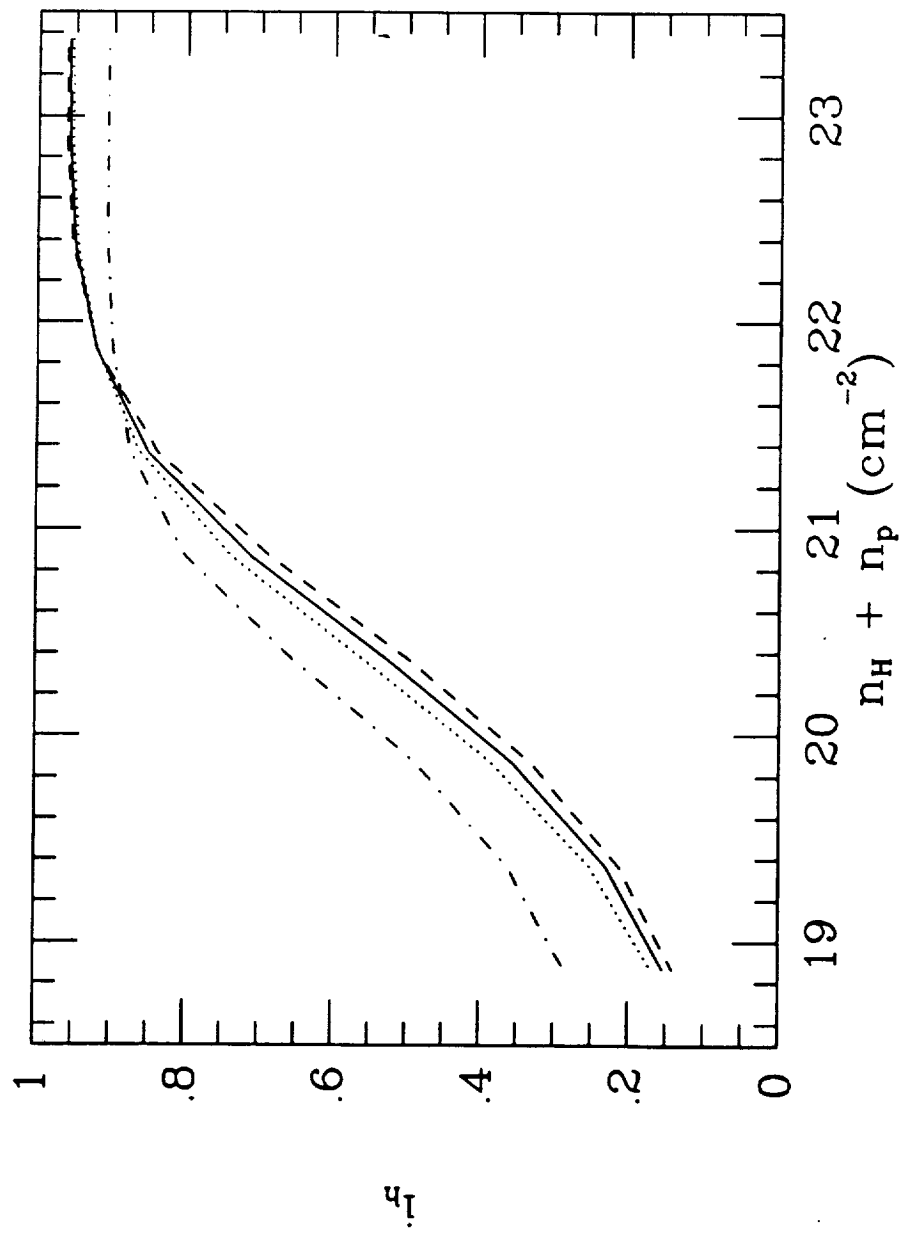


Fig. 13 (6)



Confidence limits for 1988 Dec 17 & 19 Mg II data

